PAPER

Check for updates

B@LGTs of Nd, Eu, Er, and Yb lanthanides with physicochemical interfacing for enhanced photocatalytic reduction of fluorescent dyes, transition metal ions, and quinonoid phenolphthalein†

Krishan Kumar [ID] and Man Singh [ID] *

In this work, lanthanide sulphide nanorods (LSNRs) of neodymium (Nd_2S_3), europium (Eu_2S_3), erbium (Er_2S_3), and ytterbium (Yb_2S_3) were prepared with a $LnCl_3 \cdot 6H_2O$ salt, sodium metal, and H_2S gas through a crash reaction methodology (CRM) at NTP. The LSNRs were doped with gadolinium ions (Gd^{3+}) and coated with graphene oxide (GO) to prepare bimetallic LSNRs (B@LSNRs) and GO templates (B@LGTs), respectively. LSNRs, B@LSNRs, and B@LGTs were characterised using XRD, FT-IR spectroscopy, BET analysis, UV/vis spectroscopy, HR-TEM, SEM, TGA/DTG, XPS, Raman spectroscopy, and elemental analysis. The B@LGTs as interstitial photocatalysts photocatalytically reduced the Coomassie brilliant blue red (BBR) dye, transition metal ions (TMIs), and quinonoid phenolphthalein (QHIn) in aqueous solutions under visible light. Experimental parameters including pollutant concentrations, B@LGT dosages, physicochemical properties (PCPs), and pH were optimized for achieving monodispersion and maximum PCR. The PCPs like density, viscosity, sound velocity, surface tension, friccohesity, and isentropic compressibility have predicted the spontaneity and sustainability at 288.15, 298.15, and 310.15 K with photocatalysing medium. $B@Nd_2S_3{:}GO$, $B@Eu_2S_3{:}GO$, $B@Er_2S_3{:}GO$, and $B@Yb_2S_3{:}GO$ with 2.23, 2.28, 2.38, and 1.88 eV bandgaps (E_g) and −670.14, −829.18, −767.39, and −925.57 J mol^{-1} activation energies (E_a) having −0.9869, 0.8843, −1.4011, and −1.2102 J mol^{-1} entropies (ΔS) photocatalytically reduced a dye with 96.35, 96.67, 97.60, and 99.17% quantum yields (Φ), respectively. The above-mentioned data indicated that the B@LGTs are robust photocatalysts that photocatalytically reduce BBR in 48 and 30 times shorter duration than LSNRs and B@LSNRs, respectively. It was found that 0.01 g% B@LGTs photocatalytically reduced 40 ppm BBR and 20 ppm $CrCl_3$, $NiCl_2$, $CuCl_2$, and QHIn in 30, 20, 40, 35, and 15 min, respectively. Kinetic rate constants of 3.25×10^{-2}, 3.21×10^{-2}, 3.18×10^{-2} and 3.15×10^{-2} min^{-1} for BBR were in the order of $B@Nd_2S_3{:}GO > B@Er_2S_3{:}GO > B@Eu_2S_3{:}GO > B@Yb_2S_3{:}GO$ with $4f^{3e}$, $4f^{11e}$, $4f^{6e}$, and $4f^{13e}$ electrons, respectively. This indicated first-order reaction similar to QHIn and TMIs. Furthermore, the B@LGTs exhibited favourable stabilities, with 58.1–68.05% PCR efficiencies after 10 cycles of reduction experiments.

1. Introduction

Designing quantum materials for emitting phonons of longer wavelengths to harness solar energy[1] has been a thrust area in nanoscience and technology for reducing wastewater effluents[2] without any sophisticated infrastructure.[3] Generally, the effluents discharged from various industries are intrinsically soluble in water and are difficult to separate through mechanical ways due to strong coulombic interactions.[4] The phonons noted as negative (e$^-$) and positive (h$^+$) holes of longer wavelengths reach charged centres to counterbalance the chemical linkages[5] naturally, enabling separation without the adoption of expensive methodology.[6] The over-harnessing of the natural resources poses a serious challenge[7] to a sustainable ecosystem.[8] Resources such as electricity, fuel,[9] and infrastructure are usually used to convert these wastes into second-generation pollutants.[10] The wastewater treatment plants, incinerators, resinous filtration, thin films, and landfill technologies have been used for recycling these wastes.[7] The discharge of waste dyes and heavy metals from the textile and metallic industrial establishments[11] causes nuisance in the environment.[12] However, conventional approaches have been on the corrective modes through research activities that are initiated to weaken the interactions of modern-day effluents. Hence, the need for

School of Chemical Sciences, Central University of Gujarat, Gandhinagar, Sector-30 (382030), India. E-mail: Krishan8053649040@gmail.com; Mansingh50@hotmail.com

smart photocatalysts has arisen, and their physicochemical properties are applied for wide-ranging applications like adsorption. The wastewater treatment technologies have been indispensable for recycling the wastewater effluents.[13] Among several nanomaterials,[14] the lanthanide-driven quantum materials have been found to trap the photons ($h\nu$) from solar radiation that have generated the negative and positive holes noted as intensive redox cycles (ROCs) to photocatalyze the effluents.[15] LSNRs have been effective core nanomaterials to be doped and coated with various functional and photosensitive thermodynamically stable molecules such as GO. However, the synthesis of Ln_2S_3 at temperatures >800 °C has restricted scalability, limiting their wide applications in photocatalysis[16] (Table 1). Their poorly shielded 4f electrons ($4f^{@e}$) restricted the synthesis at NTP.[29] Ln^{3+} aligns the residual positive charges holding crystalline water strongly as follows:

$$Ln^{3+} = 4d^{10}5s^25p^6 \text{ (core) } 4f^{@e}5d^06s^0 \text{ (free electron)} \quad (1.0)$$

The residual positive charge with a stronger $Ln^{3+}\cdot6H_2O$ ion-dipole has formed a thick hydration sheath.[30] The Ln_2S_3 synthesis at a high temperature disrupts the crystal growth, agglomeration,[31] phase inhomogeneity, impurity, and the particle size and shape.[32] This study reports the reduction of $LnCl_3\cdot6H_2O$ with Na metal for LSNR synthesis at NTP.[28,33] The synthesis of LSNRs or their doping with Ln^{3+} at NTP has not yet been reported (Table 1). At NTP, the reaction kinetics precisely tailors the particle size, shape, and phase composition by minimizing the thermal agitation of atoms for an ordered lattice.[34] The Ln_2S_3 synthesis at NTP is aimed to enhance the optical conductivity, electrical conductivity, and magnetic coercivity untapped by a high temperature.[26,30] The B@LGTs with minimum QEB and E_g have avoided electron–electron collisions and electron–hole recombination.[35] The B@LGTs with the GO lattice with oxygenated functional groups (FGs) have enhanced the surface continuity that receives the $h\nu$ to a larger extent and transforms to holes for expeditious photocatalysis without rebouncing.[36] The B@LGTs have three interstitial tiers to promulgate the quantum tunnelling effect (QTE) and the least quantum energy barrier (QEB) via friccohesity resonating energy transfer (FRET). The tiers have enabled the B@LGTs for an expeditious PCR of the effluents. A lot of electricity, infrastructure,[37] manpower, and water are used in recycling the wastes[38] through the conventional methods.[39] Thus, the B@LGT photocatalysts, on equipartitioning the potential energy (PE) to kinetic energy (KE), have enhanced the surface area,

allowing for the excitation of electrons from the valence band (VB) to the conduction band (CB) upon exposure to solar energy.[33] Since 2016 to date, only a few research works have been reported, as given in Table S28.† This is the first reported study, wherein lanthanides are used as dopants. The sulfides of lanthanum or cerium have produced H_2 and O_2 by splitting wastewater using sunlight or electricity.[40] The B@LGTs could intensify the cyclic voltammetry to transform the $h\nu$ to holes, which seems incomparable to the f-GO reported previously.[41] The B@LGTs have split the BBR, TMIs, and QHIn wastewater pollutants discharged from the textile,[23] food, paper, printing,[42] leather, and cosmetic industries.[43] The conjugated water-soluble textile and non-biodegradable Coomassie BBR dyes,[12,44] TMIs, and QHIn lower the biological and chemical oxygen demands upon light exposure.[33,45] It splits O_2 into free radicals[30] as BBR + $h\nu$ → BBR* + O_2 → BBR + 2O·, causing a reactive oxygen stress. The B@LGT with 1.88–2.38 eV E_g could act as a cracking catalyst in the petroleum industry replacing the transition metals.[46,47] The B@LGTs with the interstitial tiers of different electronic energies seem to align as a monolayer with adherence for enhancing the frictional force with least surface tension (γ). Therefore, the energy of B@LGTs is integrated with $\int_{4f^{@e}}^{FGs} \psi_{4f} \times \psi_{FGs} = 1$ through the dopant and the GO upon exciting $4f^{@e}$ (ψ_{4f}) and FGs (ψ_{FGs}) seems to transform the
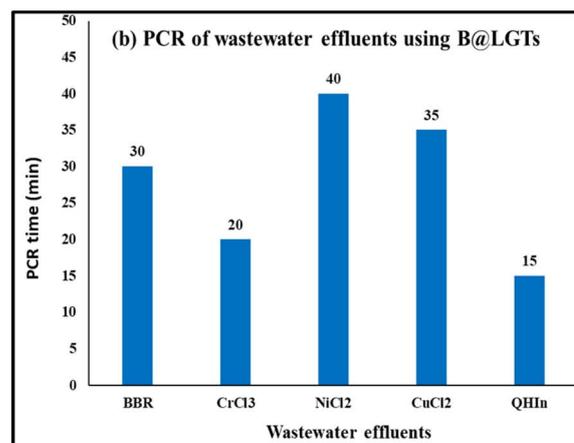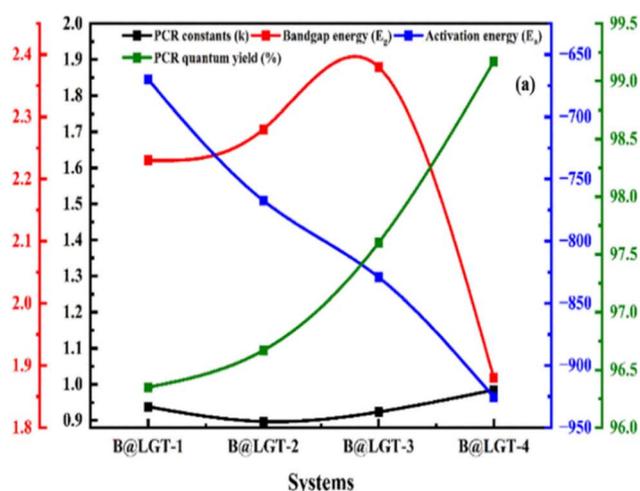

Table 1 Comparative study about lanthanide sulfide synthesis at higher T/K

Synthesis methods	Temp. (°C)	References
Hydrothermal	750	17
Hydrothermal	400–1150	18 and 19
Hydrothermal	800–1300	20 and 21
Solvothermal	750–800	22–25
Hydrothermal	600–1000	16, 21 and 26–28
Crash reaction methodology	NTP	This work

Fig. 1 (a) Photocatalysis interfacing with PCPs. (b) PCR of effluents with time.

$h\nu$ into the redox energy[9] for PCR. The B@LGT s exhibit enhanced surface resonance owing to oxidation (Ln^{3+} or $\psi_{Ln^{3+}}$) and reduction (S^{2-} or $\psi_{S^{2-}}$) potentials aimed at boosting the surface plasmonic resonance (SPR).[48] The B@LGTs could advance the thin-film technology, digital ink, quantum dot MRI and tomography[22,49] with a contrasting activity caused by Gd^{3+}. The B@LGTs could be used as complementary nanomaterials for spintronics,[50,51] electrical and thermal conductivies,[33] piezoelectric devices, thermoelectric devices, and biocompatibility.[52,53] The B@LGTs for solid oxide fuel cells could serve as the redox catalysts and electrode nanomaterials for enhanced lifespan to split water.[54] The anodic B@LGT aligns to a cathodic dye with a higher viscosity and a lower surface tension, favouring the energy storage and supercapacitors.[55,56] The higher viscosity with stronger frictional forces and lower surface tension comfortably aligns the B@LGT to develop a stable double layer of the negative and positive charges (Fig. 16). The study of PCPs have acted as the prerequisite database to interface the photocatalysis. The monodispersions of aq-B@LGTs predicted with the PCPs have improved the PCR of the BBR, TMIs, and QHIn on subsequent adsorption.
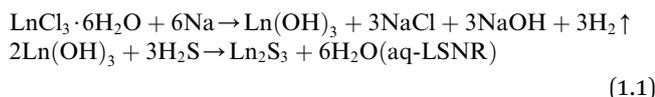
2. Materials and methods

2.1. Materials

Graphite flake (Gt < 20 mm), H_2SO_4 (99.9%), $KMnO_4$ (>99.9%), H_2O_2 (30%), HCl, NaOH, hexahydrate chloride salts of neodymium, europium, erbium, and ytterbium, gadolinium nitrate hexahydrate (>98%), sodium metals (>99%), FeS (98%), BBR, phenolphthalein, $CrCl_3$, $NiCl_2$, and $CuCl_2$ were procured from Sigma-Aldrich. Petroleum ether (40–60) was obtained from Sisco research laboratory and absolute alcohol from SCVUS Mandli India. The solutions were prepared with Milli-Q water.
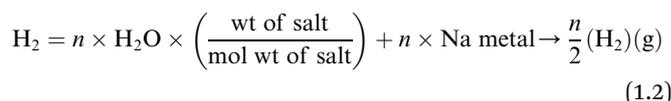
2.2. Crash reaction methodology (CRM) for LSNR synthesis

LSNRs were synthesised by our previously reported method.[33] The hexahydrate of $NdCl_3$, $EuCl_3$, $ErCl_3$, and $YbCl_3$ (0.001 M) was crashed with Na metal (0.006 M) individually by CRM. $Nd(OH)_2$, $Eu(OH)_2$, $Er(OH)_2$, and $Yb(OH)_2$ were produced, along with NaCl, NaOH, and H_2 gas as side products. The side products were confirmed with $AgNO_3$, phenolphthalein, and gas chromatography.[30] $Ln(OH)_2$ was rinsed with water, centrifuged and dried at 60 °C. $Nd(OH)_2$, $Eu(OH)_2$, $Er(OH)_2$, and $Yb(OH)_2$ were individually mixed with H_2O and sonicated for 2 h to monodisperse on testing. The H_2S gas was passed (10 min) to monodisperse the lanthanide hydroxides (Fig. 2(I)). The LSNRs were obtained and dried at 50 °C for 12 h in an oven, and the reaction is described as follows:

$$LnCl_3 \cdot 6H_2O + 6Na \rightarrow Ln(OH)_3 + 3NaCl + 3NaOH + 3H_2 \uparrow$$
$$2Ln(OH)_3 + 3H_2S \rightarrow Ln_2S_3 + 6H_2O(aq\text{-}LSNR)$$

$$(1.1)$$

2.3. H_2 gas generation

First, 73.17 mL H_2 gas was generated from 0.001 M $LnCl_3 \cdot 6H_2O$ with 0.006 M Na during CRM. Na has dissociated the crystalline H_2O into H_2 flame as follows:

$$H_2 = n \times H_2O \times \left(\frac{\text{wt of salt}}{\text{mol wt of salt}} \right) + n \times \text{Na metal} \rightarrow \frac{n}{2}(H_2)(g)$$

$$(1.2)$$

The $n = 6$ infers the H_2O crystalline molecules of $LnCl_3$ that split to H_2 gas that had intensified a flame. Thus, the $2H_2 + O_2 = 2H_2O$, $\Delta H = -572$ kJ mol^{-1} combustion is noted as clean energy process achieved at ~500 °C through 350 °C + ~150 °C. The yellow flame was sharpened from $NdCl_3$ to $YbCl_3$ on increasing their 4f electron from 4 to 13 respectively. Na reduced H_2O to H_2 gas in a shorter duration with $YbCl_3$ of $4f^{13e}$ than $ErCl_3$. Then $3s^1$ Na by competing with $4f^{6e}$ spins detached $6H_2O$ from $LnCl_3$. $ErCl_3$ with $4f^{11e}$ has turmoiled a flame with H_2 clouds (Fig. 2(II)). The sustainable H_2 fuel could be used to generate electricity,[57] ammonia for fertilizer, and methanol[58] and remove sulfur from fuels. H_2 with CO_2 could be used to synthesise several hydrocarbons for combustion engines.[59]

2.4. Synthesis of B@LSNRs

B@LSNRs were synthesised by refluxing aq-$Gd(NO_3)_3$ with aq-LSNR in 1/4 ratio at 650 rpm and 90 °C for 12 h. The product was settled and washed with water to remove the undoped Gd^{3+} followed by centrifugation. The initial filtrate had a decolourised pink colour of QHIn (indicator) owing to formation of HNO_3 during B@LSNRs synthesis; however, it was removed after washing 3 times. Excess HNO_3 has indicated Gd^{3+} doping in larger amounts, as revealed by XPS and elemental analysis[60] (Fig. 3, 13 and Table 5). The Gd^{3+} had entered the lattice of the LSNRs and developed its own hydration spheres with those of the LSNRs. That has facilitated a doping due to *in situ* HNO_3 formation with chemical potential (μ_i) demonstrated as.
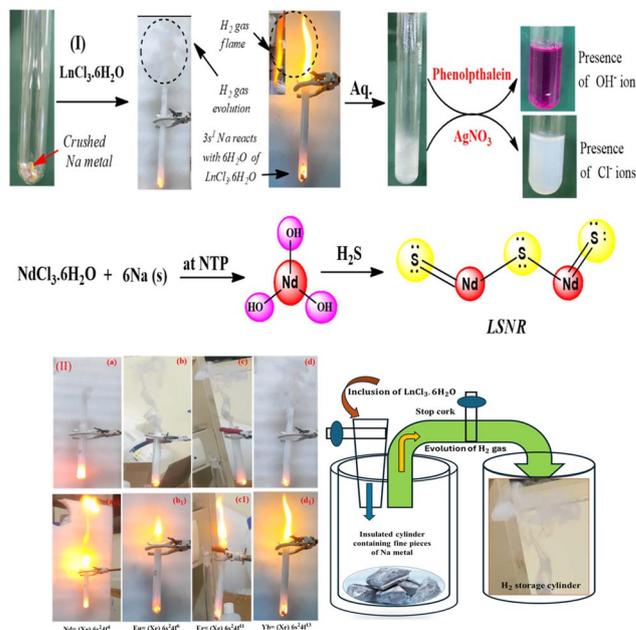

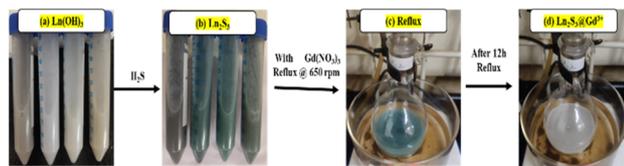Fig. 2 (I) CRM for LSNR *via* CRM at NTP. (II) Energy storage model and H_2 Flames.

Fig. 3 LSNR doping with Gd^{3+} for B@LSNR synthesis.

$$Ln_2S_3 + Gd(NO_3)_3 \rightarrow Ln_2S_3 \approx Gd^{3+} \text{ (aq-B@LSNR)} \quad (1.3)$$

$$nH_2O \rightarrow (H_2O)_n \leftrightarrow NHS, \ \mu_{H_2O} = \left(\frac{\partial G}{\partial n}\right)_{T,pH} \neq \mu_{LSNR} = \left(\frac{\partial G}{\partial n}\right)_{T,pH} \quad (1.4)$$

The wavefunction of H_2O monomer (ψ_{H_2O}) with rotational, vibrational, and translational (rovitronic) motions of $Gd(NO_3)_3$ has encapsulated Gd^{3+} with LSNR, and the activities (a_i) are as follows:

$$a_{Gd^{3+}} = e^{\frac{\Delta\mu_{Gd^{3+}}}{RT_1}}, \ a_{LSNR} = e^{\frac{\Delta\mu_{LSNR}}{RT_2}}, \ a_{Gd^{3+}} \neq a_{LSNR} \text{ but } a_{Gd^{3+}} > 0 \quad (1.5)$$

Gd^{3+} has entered the S^{2-} and Ln^{3+} cavities of LSNRs with $\Delta G_{LSNR} \neq \Delta G_{NHS \ zone}$ spontaneities due to different redox potentials of S^{2-} and Ln^{3+}. The S^{2-} of LSNR has enabled a doping with the Gd^{3+} on broadening a size of NRs by developing the moderate interstitial van der Waals forces (VWFs) (Fig. 9).

2.5. Synthesis of graphene oxide (GO) and B@LGTs

GO was synthesized according to a previous report with slight modifications.[61] The Gt flakes and $KMnO_4$ were taken in an RB flask in 1/6 ratio and H_2SO_4 (100 mL) was poured dropwise keeping on an ice bath with continuous stirring. It was refluxed at 650 rpm at 55 °C in an oil bath for 12 h. Later, cold water and 3 mL H_2O_2 (30%) were added under stirring for 10 min to obtain a GtO (eqn (1.5)). The resulting product was centrifuged at 8000 rpm for 10 min and washed with normal water, HCl, and absolute alcohol until the pH reaches 7. NaCl and Na_2SO_4 were removed in 5 sequential washings, which was confirmed by testing with $AgNO_3$ and $BaCl_2$. The GtO mixture on sonication at 28 kHz for 3 h has formed a brownish GtO dispersion on exfoliating to GO sheets[62] after the addition of petroleum ether for separation and drying at 60 °C. Brownish GO sheets were reproduced[61] (Fig. S1†), and after sonication for 3 h, they were mixed with B@LSNR in 1/6 ratio and refluxed at 650 rpm at 90 °C for 12 h. After 12 h, the resulting dark product was settled and washed with H_2O, followed by centrifugation at 8000 rpm for 8 min. The GO sheets could have competitively interlinked with Gd^{3+} and Ln^{3+} *via* S^{2-} or $\psi_{S^{2-}}$ of tentropic cavities aligning the B@LGT as astral geometry, as elucidated by HR-TEM (Fig. 9).

3. Results and discussion

B@LGTs have transformed the $h\nu$ into holes of longer wavelengths to photocatalytically reduce the pollutants. The tiers have oscillated in the same phase aligned with the specific NHS of water dipoles shortening the PCR time. The tiers have synchronized the oscillations of each constituent to a single-valued wavefunction by avoiding electron bouncing to expeditiously cross the Fermi energy barrier or QEB. The equi-partitioning of the surface charges stabilized to the electrostatic dipoles has been predicted with the Raman spectra with a sharper intensity of D and G bands (Fig. 11). The tier with a least interfacial energy barrier and E_a has enabled the B@LGTs to photocatalytically reduce the effluents. The tier structures have enhanced reusability as the reduced effluents did not coagulate rather adhered to the interstities with moderate VWFs as per Schrödinger and Le Chatelier spontaneities. The B@LGTs favour adherence and coherence by minimizing the collisions for ROCs (Fig. 17). Fig. 4 elucidates the morphology of B@LGTs with the 1st tier for LSNR, 2nd tier for Gd^{3+}, and 3rd tier for GO that have photocatalytically reduced BBR, $CrCl_3$, $NiCl_2$, $CuCl_2$, and QHIn in 30, 20, 40, 35, and 15 min, respectively. The PCPs and thermodynamic parameters have predicted a role of each tier enhancing the sustainable photocatalytic activities. The B@LGTs as super-photocatalysts or photomultipliers on monolayer adhesion with LSNR–Gd^{3+}–GO interfacial templates photocatalytically reduced the effluents in 15–40 min with 90–99.8% Φ (Fig. 19 and 22). The Φ value from $4f^{3e}$ to $4f^{13e}$ (x-axis) is polynomially increased with a linear decrease in E_a, while E_g initially increased from $4f^{3e}$ to $4f^{11e}$, but from $4f^{11e}$ to $4f^{13e}$, it is decreased (Fig. 1a). The increasing Φ inferred an access of phonons to BBR on decreasing E_a. The B@LGTs have acted as anodic site to receive the $h\nu$ for exciting the VB electrons to CB on storing the solar energy. The e^- and h^+ holes have access to cathodic BBR and others with a longer λ. Fig. 1a predicts the robust anodic and cathodic interfacing for harnessing solar energy *via* $4f^{3e}$ to $4f^{13e}$ for photocatalytic reduction.

3.1. Temperature-dependent PCPs as PCR sensors

The temperature-dependent surface properties of 0.01 g% B@LGTs at 288.15, 298.15, and 310.15 K have predicted the monodispersion, while the regression coefficients of PCP data from 288.15 to 310.15 K were used to calculate the respective PCPs at 283.15 and 313.15 K. The temperature variation has inferred a thermal stability of aq-B@LGTs on absorbing a maximum $h\nu$ at 298.15 K than others. At 298.15 K, an infinitesimal decrease in surface tension indicates monodisperse B@LGTs for $h\nu$ capturing (Fig. 19). No coagulation, no dimerization, and no clustering with least QEB have optimized the PCR at 298.15 K. The T/K below and above 298.15 K is being
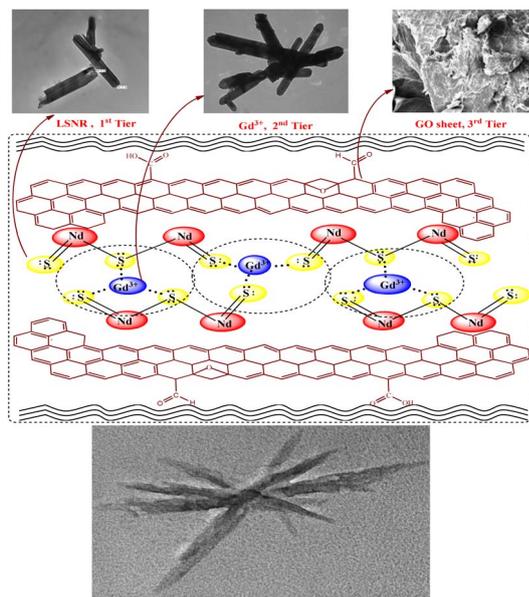
$$2KMnO_4 + 3H_2SO_4 \rightarrow K_2SO_4 + 2MnSO_4 + 3H_2O + 5[O]$$
$$GO + \cong \rightarrow GO^*, \ GO^* + B@LSNR \approx Gd^{3+} \rightarrow B@LSNR \approx Gd^{3+}@GO(aq\text{-}B@LGT) \quad (1.6)$$

Paper

Fig. 4 B@LGT with three-tier interstities in a same phase for higher functionality.

pursued for determining the temperature dependence of PCR and physisorption activities of B@LGT for reusability. The surface tension (γ), viscosity (η), friccohesity (σ), density (ρ), and isentropic compressibility have predicted the monodispersion for ordering the e^- and h^+ holes w.r.t. the anodic B@LGT and cathodic effluents. The tier-like structure of the B@LGT with a higher surface area and a moderate surface tension acted as a superphotocatalyst because a longer λ opted to the quantum tunnelling effect. The lower E_a, ΔH, ΔG, and ΔS values have predicted the spontaneous reorienting activities of the B@LGT to receive the $h\nu$. Lower γ with higher η values for aq-B@LGT than aq-LSNR and B@LSNR at 298.15 K have inferred on aligning the $h\nu$ receiving dipoles. The BBR, TMIs, and QHIn were photocatalytically reduced for the first time to recycle wastewater. The PCPs and thermodynamic parameters of B@LGTs have acted as a prerequisite database for receiving the $h\nu$ consistently without coagulation. The $h\nu$ receiving sites get reoriented to bulk with a higher γ value, while the lower γ with higher η values align at surfaces (Fig. 18 and 19). γ and η both interfaced *via* σ have depicted the spatial orientation of B@LGTs aligning along the effluents *in situ*. The B@LGTs have absorbed the maximum $h\nu$, intensifying the ROCs at 298.15 K with surface continuity due to a lower surface tension with a higher viscosity for higher Φ. The fraction of occupied Fermi surface (θ) with a vacant surface ($1 - \theta$) have facilitated to receive the $h\nu$ and also a transfer of holes to the effluents as $k_1(1 - \theta)h\nu = k_2\theta$ steady state.[63] The k_1 and k_2 values infer the $h\nu$ receptance and transfer of holes in the first order with energy distribution for generating the holes as follows:

$$\text{Energy distribution} = \frac{n_i}{N} = \frac{e^{-E_i/k_B T}}{\sum\limits_{j=1}^{j=n} \left(e^{-E_j/k_B T} \right)} \quad (1.7)$$

'n' refers to the number of energy ensembles, total energy N_E and n_e could have been $N_E \approx \sum n_e$, equipartitioned (eqn (1.7)). The receptance of the least numbers of $h\nu$ excited the functional sites of B@LGT for a higher surface energy (KE $\approx$ PE) for PCR as follows:

$$E_\psi = \frac{\partial p^2}{2m}\psi \leftrightarrow V(x, t) \quad (1.8)$$

The B@LGT due to aligned[64] interstities generated holes with ψ interfacing $4f^{@e}$ along Ln^{3+} and S^{2-} oscillating with the wavefunctions ($\psi_{Ln^{3+}}$) and ($\psi_{S^{2-}}$) as $\psi_{Ln^{3+}} \neq \psi_{S^{2-}}$ (eqn (1.8)). $|\psi_{Ln^{3+}}| \times |\psi_{S^{2-}}| \neq 0$ of LGT reduced the dyes in 60 min, as reported previously.[33] The oscillating charges ($\psi_{Ln^{3+}} \neq \psi_{S^{2-}}$) of B@LGT have received $h\nu$ with a higher relaxation time (eqn (1.9)). The minimum internal entropy (ds/dt) and topographical entropy (tentropy, ΔS_T) seem to equally spin the electrons of B@LGT at position 'x' nm at time 't' with $V(x, t)$ PE. The GO $\approx$ NHS and GO $\approx$ LSNR linkages of aq-B@LGTs spin in the same phase with entropy as follows:

$$\Delta S_{B@LGT} \pm \Delta S_{NHS} \approx \Delta S_{B@LGT-NHS},$$
$$\Delta S_{B@LGT} \pm \Delta S_{NHS} \leq 0 \text{ and } \Delta S_{B@LGT-NHS} \quad (1.9)$$

The $\Delta S_{B@LGT} \pm \Delta S_{NHS} > 0 > \Delta S_{B@LGT} \pm \Delta S_{NHS}$ trends have weakened and strengthened the B@LGT $\approx$ NHS out of B@LGT $\approx$ B@LGT and NHS $\approx$ NHS linkages. Higher friccohesity infers the $\psi_{B@LGT-NHS}(x, t)$ at 'x' $\neq 0$ position between B@LGT and NHS at 't' relaxation time in the same phase (φ). Thermograms have also predicted a streamlining of thin-layer 2D whitish laces with energy as follows:

$$E_{B@LGT-NHS} = E_{Corner} + E_{FGs \text{ at opposite plane}} + E_{FGs \text{ at width}} \quad (2.0)$$
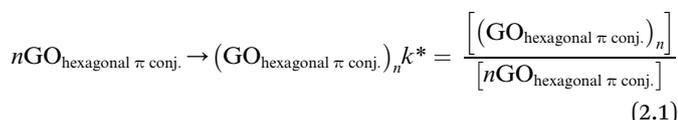
Eqn (2.0) infers a plane area being occupied from the corner and width of aq-B@LGT upon increasing the γ values and decreasing the η values (Fig. 18 and 19). Aq-B@LGTs with monolayer NHS adhesion moderately align. The water dipoles aligned with core LSNRs, dopant, and GO of B@LGTs to communicate mutually with comparatively high γ values (Fig. 9). The B@LGTs with lower E_g could upgrade nano-thin films,[65] fibres, optics, catheters, optoelectronics,[66] digital inks, and nanomaterials.[67] The B@LGT could be doped with I_2 of induced dipoles with the lowest reduction potential widening energy domains[68] similar to our earlier study[33] on LSNR doped with GO and without doping (1 : 4). This deals with the coating of B@LSNR with GO unlike LGT for B@LGTs. The $O^{\delta-}$ and $2H^{\delta+}$ of H_2O with metallic (TMI, Ln^{3+}) dopants lowered the E_g solar energy.[61,69] The B@LGTs had aligned the tentropic cavities upon the scintillation of electrons from the VB to the CB as $|\psi_{Dipole-DOS}|^2 > \psi_{Dipole} \approx \psi_{DOS}$ hybridizing $|\psi_{Dipole-DOS}|^2 \approx 80\%$. BET has predicted the stabilized dipoles with lower E_g and higher surface area (Fig. 6). Terminals of S=Ln–S–Ln=S aligned *via* $\psi_{S^{2-}}$ and $\psi_{Ln^{3+}}$ eigenenergy with the NHS zone (Fig. 4). The $\psi_{Gd^{3+}}$, $\psi_{S^{2-}}$, and $\psi_{Ln^{3+}}$ of B@LGT in continuity had a higher viscous flow time (vft) and surface energies as the tiers

also adhere the water dipoles with a higher shear stress to stabilising the holes (Tables 11–13).

3.2. Water binding and heat holding abilities of B@LGTs for PCR

The 0.002 g% aq-Gd@Nd$_2$S$_3$-GO was boiled in 45 min at 103 °C@5 °C than the same amount of water in 25 min at 100 °C@5 °C due to stronger interaction of Gd@Nd$_2$S$_3$-GO. It was found that aq-Gd@Nd$_2$S$_3$-GO has acquired an extra heat at 682.543 kJ °C min^{-1} at a sharper boiling point than that of water alone. The water dipoles adhered to interstities on aligning more strongly than the hydrogen bonding of water (Fig. 5). Their constituents with water dipoles develop oscillating interfaces that detain higher heat than water alone and predict the energy storing ability of the B@LGTs. The heat holding ability of aq-Gd@Nd$_2$S$_3$-GO is useful for various thermal applications in biophysical, biochemical, and biothermodynamic fields. The stronger heat holding capacity is also attained on stronger GO binding depicted with TGA and BET (Fig. 6 and 15). It has intensified photoluminescence (PL) due to ψ in single phase by darkening a colour on stacking by producing nanoclusters of similar sizes with sharper emittance after 2 h at *RT* (Fig. 5c). On heating, the water molecules got escaped from interstities to phase out nanoclustered sheets. The monodispersion with $\eta_{\text{aq-B@LGT}} < \eta_{\text{H}_2\text{O}}$ and $\gamma_{\text{aq-B@LGT}} < \gamma_{\text{H}_2\text{O}}$ has caused PL without rebouncing the $h\nu$(Fig. 5c, 18, and 19). The aq-B@LGTs were realigned to a hydrophilic head and a hydrophobic tail with brighter PL[70,71] on forming the symmetric bipolar electrostatic stabilisation due to needful η and comparatively lower γ values. With the needful Nernst potential, 4f$^{@e}$ and π-conjugation enhanced the photocatalytic activity[61] (Fig. 5d). The thermal energy generated PL, as [O] was unable to functionalize all the π-conjugated GO and responded differently upon heating as follows:

$$n\text{GO}_{\text{hexagonal }\pi\text{ conj.}} \rightarrow \left(\text{GO}_{\text{hexagonal }\pi\text{ conj.}}\right)_n k^* = \frac{\left[\left(\text{GO}_{\text{hexagonal }\pi\text{ conj.}}\right)_n\right]}{\left[n\text{GO}_{\text{hexagonal }\pi\text{ conj.}}\right]} \tag{2.1}$$

H$_2$O dipoles with the wavevector of Gd^{3+} 4f^{7e} within S=Ln–S–Ln=S have aligned to intrinsic tentropic cavities (ΔS_{T}) correlated with the moment of inertia (I) as follows:

$$E_\text{v} = h\nu\left(v + \frac{1}{2}\right) \text{and } I = 1/12\left(m_{\text{Ln}}l_{\text{Ln}}{}^2 + m_{\text{S}}l_{\text{S}}{}^2 + m_{\text{Gd}}l_{\text{GD}}{}^2\right) \tag{2.2}$$
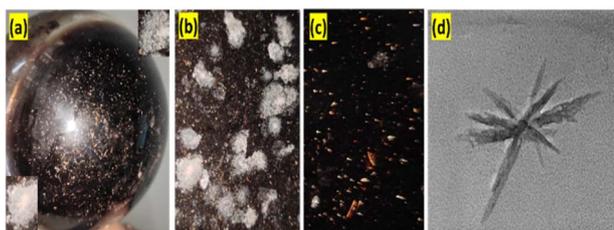

Fig. 5 (a–c) Thermally nucleated photoluminescence analysis on heating the 0.002 g% of aq-Gd@Nd$_2$S$_3$-GO for elucidating thermal stability. (d) HR-TEM image of B:Nd$_2$S$_3$-GO.

ν is the vibrational frequency of the bond based on atomic mass, v the vibrational quantum number of electrons, m the atomic mass and l the length of NRs. The rotational activities with the $h\nu$ could shorten PCR time on $m_{\text{Ln}}l_{\text{Ln}}{}^2 \neq m_{\text{S}}l_{\text{S}}{}^2 \neq m_{\text{Gd}}l_{\text{Gd}}{}^2$. The alignment of solvated B@LGT stabilised the chemical bond vibrational frequency vis-a-vis the vibrational quantum number of 4f electrons. The aq-Gd@Nd$_2$S$_3$-GO had generated a whitish PL on storing energy with similar wavevector (K-space) without causing electronic collisions. This was attained on distributing the $h\nu$ energy within the interstitial constituents of Gd@Nd$_2$S$_3$-GO through the energy distributing factor $\frac{1}{\sqrt{\pi a^3}}e^{-r/r^\circ}$, the r°, Bohr and r, radii for lattice 'a'. The B@LGT combined with aq-BBR, TMIs, and QHIn to boost the PL (Fig. 16). B@LGT at $r > r^\circ$ receives $h\nu$ with least permittivity (ε) and mutually shares it with effluents, as predicted *via* PCPs. The $r = r^\circ$ infers no reduction and no PCPs without $\psi_1 \neq \psi_2 \neq \psi_3 \ldots \neq \psi_n$ conjugation.[72] Fig. 5 depicts the single lattice elongating a wavelength[73] on thinner 2D GO sheets similar to those reported previously.[61] XRD, HR-TEM, and BET predicted that the synchronized electronic clouds of dopants, and coating agents of B@LGT have intimately hybridized without twisting on aligning interstities similar to their individual angular momentums. The La$_2$S$_3$, Ce$_2$S$_3$, Tb$_2$S$_3$, and Ho$_2$S$_3$ as core LGTs as the two tiers have slightly modulated the electrostatic interacting activities of aq-BSA protein with mild unfolding dynamics reported in an earlier study.[33] Noticeably, polyvinylpyrrolidone (PVP)-capped rod-shaped europium (Eu^{3+})-doped gadolinium oxide (Gd$_2$O$_3$) nanoparticles (PVP@Gd$_2$O$_3$:Eu^{3+} NPs) have been effective to tune electrostatic charges of salt bridges of proteins.[24] Thereby, the B@LGTs could further elaborate the charges to intensify the interacting activities with the peptides and intercalate the base pairs of dsDNA which are being pursued. The aligned B@LGTs have generated the e$^-$ and h$^+$ holes of a longer mean free path that photocatalytically reduced BBR, Cr^{3+}, Ni^{2+}, and Cu^{2+}, and QHIn within 15–40 min (Fig. 22).

3.3. Brunauer–Emmett–Teller (BET) analysis

With the BET technique, a solid material measured the adsorption of inert gases such as N$_2$ upon increasing the relative pressure (P/P_0) at NTP. Thus, the amounts of adsorbed gas by LSNR, B@LSNR, and B@LGT of Nd$_2$S$_3$ determined their surface area, pore volume, and pore size at 77 K (Fig. 6). B:Nd$_2$S$_3$@GO adsorbed a higher amount of N$_2$ and also desorbed at the same rate. The similar rates infer the distribution of the similar sized pores of similar dimensions with 100% physisorption. The higher surface area, larger pore size, and pore volume and physisorption enabled the use of B@LGTs for 10 fresh dye samples of 40 ppm for PCR with 10 times reusability. Each time, the B@LGTs were washed, used for adsorbing the reduced effluents and desorbed for subsequent cycles. The N$_2$ adsorptions with B:Nd$_2$S$_3$@GO are fitted with standard isotherms as per the IUPAC classification.[9] The similar rates of adsorption and desorption with B@LGTs have predicted the mesopores of sharper and broader edges.[42] Nd$_2$S$_3$ and B@Nd$_2$S$_3$ of 13.131 and 15.80 m^2 g^{-1} surface area with 0.009 and 0.019 cc g^{-1} pore
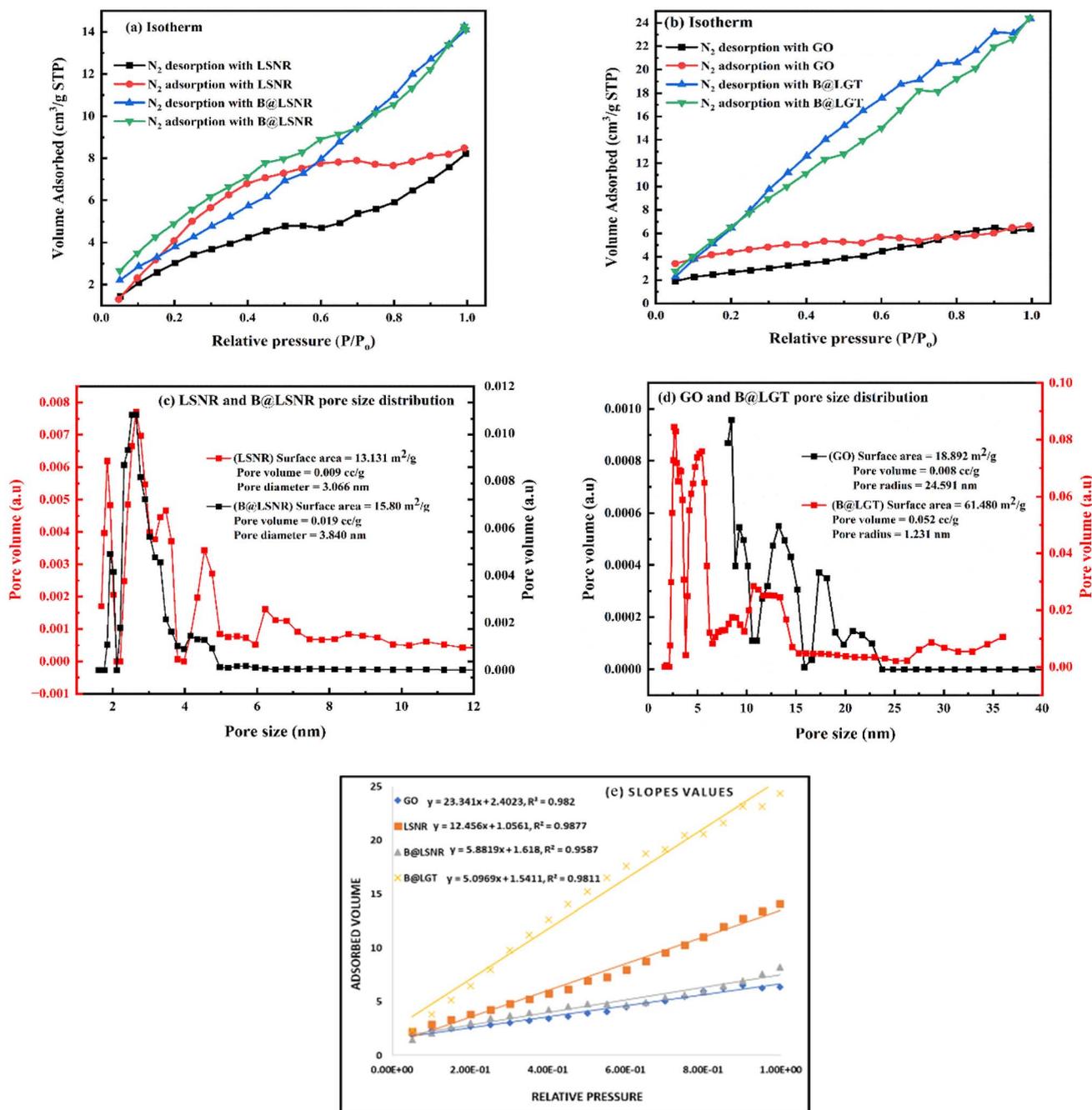
Fig. 6 (a and b) Isotherms and (c and d) pore size of Nd_2S_3, $B@Nd_2S_3$, GO, and $B:Nd_2S_3@GO$. (e) Slopes obtained during the adsorption of N_2 by $B:Nd_2S_3@GO$.

volume respectively indicate a lower N_2 adsorption than B@LGTs due to coating. The coating seems to have transformed the cohesive to adhesive forces with two different centres of electronic energy well that exchanged their energies through FRET. Thus, a surface area of $B:Nd_2S_3@GO$ has been increased with higher $h\nu$ receiving and e^- and h^+ hole generating abilities. The 2D GO sheets might have equipartitioned their energies normalizing the pore sizes than the uncoated. The 61.480 m^2 g^{-1} area of $B:Nd_2S_3@GO$ is higher than Nd_2S_3, and $B@Nd_2S_3$ by 4.60, and 3.89 times respectively supported with SEM and HR-TEM (Fig. 9 and 14). Therefore, this research opens the novel

gateways to choose several coating agents to enhance the surface area. The Barrett–Joyner–Halenda and Villarroel–Barrera–Sapag (VBS) methods have been fitted for their pore size distribution with monolayer to multilayer N_2 adsorption at a lower pressure with ~2–50 nm pore diameter (Fig. 6). The first-order adsorption to desorption with $B:Nd_2S_3@GO$ with almost the same slope values has inferred equal distribution of residual charges for equally reorienting the pore sizes uniformly without much compression at high pressures and low temperatures (Fig. 6a and b). The compressibility and pore volume as aq-$B:Nd_2S_3@GO$ > GO > $B@Nd_2S_3$ > Nd_2S_3 infer a higher surface

energy with B:Nd$_2$S$_3$@GO for expeditious access to BBR, TMIs, and QHIn (Tables S26 and S27†). Thus, the B@LGT could be extended to several other wastewater material to recycle them through the PCR and then with a subsequent adsorption. B:Nd$_2$S$_3$@GO with a longer wavelength (λ) of holes overcomes a QEB than others. B:Nd$_2$S$_3$@GO is reusable for five cycles to harness the $h\nu$ as $h\nu$ + B@LGT = B@LGT* + (e$^-$, h$^+$)* → PCR supported with PCPs (Fig. 17). The slopes as B:Nd$_2$S$_3$@GO < B@Nd$_2$S$_3$ < Nd$_2$S$_3$ < GO have inferred stronger N$_2$ absorbing ability with B:Nd$_2$S$_3$@GO than with GO (Fig. 6e). The least N$_2$ adsorption rate with GO infers stronger VWFs at constant temperatures and pressures at fixed compositions. Thus, similar to N$_2$ entry to the interstities, the water dipoles were also entered that had equipartitioned the potential to kinetic energy.

3.4. UV/vis analysis

Aq-LSNRs have consolidated the transitions at λ_{max} = 214 nm with abs = 0.4 unlike λ_{max} = 302 nm and abs = 0.6–0.9 for B@LSNR while Gd^{3+} has caused a transition on a dive in abs = 0.32–0.48 at λ_{max} = 268 nm. The dive abs infers engaging the electrostatic Ln^{3+} and S^{2-} domains by weakening the transitions of B@LSNR at λ_{max} = 268 nm, and it is elucidated by morphology and BET analysis (Fig. 6 and 9). Abs = 0.32–0.48 and 0.24–0.56 diffused transitions at 228 and 312 nm for GO and B@LGT on $\pi \to \pi*$ and n $\to \pi*$ respectively indicate a longer wavelength with B@LGT. Thus, the n $\to \pi*$ energies have been further enrooted to the dopant and LSNRs in the same phase to enhance the resulting λ. The coating has diffused the transitions within 300–475 nm λ with abs = 0.10–0.34 on uniform GO sheet distribution with B@LSNR. The B@LGTs with a similar lattice

Fig. 7 UV/vis absorption spectra of (a) LSNR, (b) B@LSNR and (c) B@LGT.

have indicated an interlink with Gd^{3+} on elongating the wavelength compared to B@LSNRs (Fig. 7c). The B@LSNR with the dopant aligned the water dipoles without leaching out the dopant and coating agents on sonication. The quantum mechanically flexible GO with the quantized energies of FE-LSNR, FG-LSNR, FE-Gd-LSNR, and FG-Gd-LSNR each might have developed uncounted ensembles. The B@LSNRs have integrated the energies to eigenenergy with a single-valued wavefunction (ψ_{sv}). The $\pi \to \pi*$ transition for C=C and n $\to \pi*$ for C–O–C of GO have intensified the distinguished activities.[74] $E_{228} = (hc/228)$ and $E_{312} = (hc/312)$ from 228 to 312 nm with B@LGT integrated the holes on VB → CB to photocatalytically reduce BBR in 30 min. The B@LGTs have aligned the H$_2$O dipoles in their interstities with a higher surface tension and longer λ than GO. Absorbance as Yb$_2$S$_3$ > Nd$_2$S$_3$ > Er$_2$S$_3$ > Eu$_2$S$_3$ with 4f^{13e}, 4f^{3e}, 4f^{11e}, and 4f^{6e} respectively was occurred at λ_{max} = 214 nm. That had predicted the similar fermi energy levels for the Yb$_2$S$_3$, Nd$_2$S$_3$, Er$_2$S$_3$, and Eu$_2$S$_3$ because their electrons are filled in 4f orbitals. It differs from 300–500 nm with B@LGTs as the electrons of dopant and FGs of coating agent have shared their angular momentum. That have shifted the λ_{max} = 300–500 nm to absorb energy from sunlight (Fig. 7d). The Yb$_2$S$_3$ could have detained a higher energy than Nd$_2$S$_3$. Their 4f^e could not affect the λ_{max} = 214 nm except absorption, as their energy levels remain the same except the degeneracies. The 4f^{13e} and 4f^{3e} shared by S^{2-} of LSNR matrices[75] synchronized the surface area of tentropic cavities (Fig. 7c). Thus, the abs as B@Yb$_2$S$_3$ > B@Nd$_2$S$_3$ > B@Er$_2$S$_3$ > B@Eu$_2$S$_3$ have shortened the PCR time. The B@LGTs with C=C have induced the $\pi \to \pi*$ transition at λ_{max} = 228 nm compared to LSNR at λ_{max} = 214 nm and B@LSNR at λ_{max} = 302 nm that have realigned the ψ as follows:

$$E_\psi = \frac{p^2}{2m}\left[|\psi|_{\text{B@LGT}}{}^2 \approx |\psi|^2 \approx |\psi|_{\text{dye}}{}^2\right]$$
$$+ \frac{q^+q^-}{4\pi\varepsilon r^2}\left[|\psi|_{\text{B@LGT}}{}^2 > |\psi|^2 < |\psi|_{\text{dye}}{}^2\right] \gg \text{QEB} \quad (2.3)$$
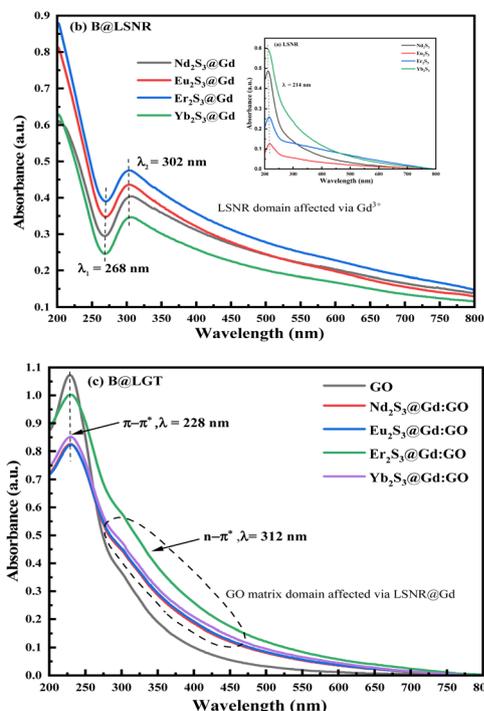
The $p^2/2m$, KE and $q^+q^-/4\pi\varepsilon r^2$ are PEs.[76] $|\psi|_{\text{B@LGT}}{}^2 > |\psi|^2 < |\psi|_{\text{dye}}{}^2 \neq |\psi|_{\text{B@LGT}}{}^2 \approx |\psi|^2 \approx |\psi|_{\text{dye}}{}^2$ did not photocatalytically reduce compared to $|\psi|_{\text{B@LGT}}{}^2 \approx |\psi|^2 \approx |\psi|_{\text{dye}}{}^2$ at 312 nm, which photocatalytically reduced in a shorter time. The B@LSNR has produced the new peaks at λ_{max} = 268 and 302 nm than 214 nm with the bare LSNR due to energy equipartitioning on doping (Fig. 7b). Thus, the doping interstities also gained a geometry with their own energies. B@LSNR$_{268\ nm}$ − LSNR$_{214\ nm}$ = 3.6×10^{-25} J is the doping energy on streamlining 4f$^{@e}$. Gd^{3+} has reduced E_g with longer λ_{max}, the Gd$^{3+}\cdots$S^{2-} attraction and Gd$^{3+}\cdots$Ln^{3+} repulsion might have synchronized the holes at λ_{max} = 302 nm with B@LSNR$_{302\ nm}$ − LSNR$_{214\ nm}$ = 2.25×10^{-25} J, for a shorter PCR time (Fig. 7b).

λ_{max} = 228 for B@LGT, 214 nm for the LSNR, while 268 and 302 nm for B@LSNR, which enhanced the PCR rate. The B@LSNR$_{302}$ − LSNR$_{214}$ = 2.25×10^{-25} J and B@LSNR$_{302}$ − LSNR$_{268}$ = 5.8×10^{-25} J energies are noted as coating energy that had decreased the E_g from 4.86 to 1.88 eV. The higher E_g with shorter λ also induces the electron–electron collisions while lower E_g with longer λ = 302 nm gains stronger quantum

tunnelling effects on doping and coating by partitioning the cohesive to adhesive forces to oscillate with longer λ. For (μ) with B@LGT, a partial Gibbs energy ($e^{-\Delta\mu/RT}$) for electronic excitation is as follows:

$$\mu = \mu^\circ + RT\ln_{GO}, \ \Delta\mu = RT\ln_{GO} \text{ and } a_{GO} = e^{\Delta\mu/RT},$$
$$a_{B@LGT+dye} = e_{B@LGT}{}^{\Delta\mu/RT} + e_{dye}{}^{\Delta\mu/RT} \qquad (2.4)$$

The GO with intensified Raman band $|\psi|_{Constructed}{}^2 = |\psi|_D{}^2 \approx |\psi|_G{}^2$ has accessed BBR, TMIs, and QHIn. TMI-GO, LGTs, and B@LGTs have distinguished a role of 3d and 4f electrons on GO coating.[61] The B@LGTs photocatalytically reduced BBR, Cr^{3+}, Ni^{2+}, and Cu^{2+}, and QHIn in 30, 20, 40, 35, and 15 min respectively but TMI-GO and LGT in 60 and 120 min on partially filled 3d and 4f electrons.[33,61] The B@LGTs have developed the interstities with the reduced transition metals encapsulated in 2D GO sheets interfaced with the dopant and core LSNR.

3.5. Bandgap energy (E_g) from the Tauc plots

E_g indicates the energy range from the top of VB to the bottom of CB, which excites an 4f electron within a Fermi energy gap. The resulting VB electrons or holes in the lattices of B@LGTs move freely to approach the effluents for PCR. The B@LGT lattices with partially unfilled 4f electrons in the VB move to the CB within lattices as charge carriers. The B@LGTs with $E_g = 1.88$ eV have acted as semiconductors on forming the continuous energy bands to intensify the PCR. The B@LGT dimension affects the Fermi energy gaps where the electrons with LSNRs of ~4.70 eV are forbidden. The electrons of B@LGTs have jumped from the VB to the CB with infinite redox cycles with intense cyclic voltammetry for PCR. For excitation, the electrons gain an energy by absorbing $h\nu$ from light or heat analysed with PCPs at variable T/K (Fig. 18–20). The E_g value of B@LGTs was tuned with compositions of the dopant and coating GO. The interstities with B@LGTs on doping and coating have caused the interfacial linkages as molecular epitaxy that could have acted as heterojunctions for receiving the $h\nu$ from light. The LSNRs with >4.70 eV have acted as the mildest semiconductor (Fig. 8a). The E_g value has decreased on increasing T/K as the amplitude of atomic vibrations was increased with a larger interatomic spacing as follows:[77]

$$E_g = E_g^0 - \frac{\alpha T^2}{T + \beta} \qquad (2.5)$$

The E_g^0 value is extrapolated to zero; α and β ($\beta = 1/k_B T, \ J^{-1}$) are constants of B@LGTs; the lattice vibrations increase on increasing T/K, so their PCPs are studied from 288.15 to 315.15 K. Their interaction with water dipoles might have interlinked their lattice phonons, free electrons, and holes that could have affected E_g to a smaller extent. Thus, the pressure generated on their dipolar interactions might have also affected the electronic structure. The B@LGTs have energy equipartitioning, so the E_g value is fixed with a quantum confinement effect. The B@LGTs have a direct E_g value due to stable lattices attained on doping and coating (Fig. 8c). The energy split occurs at the Brillouin zone edge of B@LGTs for 1D on

a weak periodic potential producing a gap between bands. The XRD analysis depicts the symmetric planes where the dopant and GO coating have further strongly aligned the VB to CB transitions with Nernst potential through stable lattice. The VB electrons are directly excited into the CB by $h\nu$ having a larger energy than the bandgap as a direct bandgap tends to have stronger light emission and absorption.[78] The electronic transitions are directly connected to E_g with maximum charge carriers as transition states detained by B@LGTs at $\lambda = 660$ nm calculated from $\lambda = hc/E_g$ (Fig. 7). The Planck constant $h = 6.623 \times 10^{-34}$ J s, light velocity $c = 3 \times 10^8$ m s^{-1}, and $E_g = 1.88$ eV $\times 1.602 \times 10^{-19} = 3 \times 10^{-19}$ J. The B@LGTS have detained 3×10^{-19} J, as $h\nu$ has excited VB electrons to reach the CB space.[79] The 3×10^{-19} J energy with longer $\lambda = 660$ nm have predicted an intimate interfacing with the BBR, TMIs, and QHIn to PCR. Their E_g value is calculated using the Tauc plot, which directly reflects the density of energy detained by them as follows:[61]

$$E_g = \frac{hc}{\lambda}, \ \alpha = \frac{\text{absorbance(UV)}}{\text{thickness}(d)}, \ \alpha h\nu = B(h\nu - E_g)^n \qquad (2.6)$$

Eqn (2.6) indicated that $E_g \propto (1/\lambda)$, where α is the absorption coefficient, E_g the optical bandgap, B the band tailing parameter, $h\nu$ the photon, and $n = 1/2$ for direct E_g. The E_g value was calculated from $(\alpha h\nu)^2$ vs. $h\nu$ (eqn (2.6)). The E_g value for Yb_2S_3, Er_2S_3, Eu_2S_3, and Nd_2S_3 is 4.67, 4.75, 4.71, and 4.86 eV, respectively. $Gd^{3+}@Yb_2S_3$, $Gd^{3+}@Er_2S_3$, $Gd^{3+}@Eu_2S_3$, and $Gd^{3+}@Nd_2S_3$ have two E_g values in the ranges of 4.64–1.90, 4.62–2.41, 4.59–2.43, and 4.50–2.50 eV respectively (Fig. 8a and b).

Two E_g values infer the VB electrons of Gd^{3+} and Ln^{3+}, individually reaching the respective CBs as $_{18}S^{2-} = 1s^22s^22p^53s^23p^6$ has fully filled orbitals. LSNRs doped with Gd^{3+} ($4f^{7e}$) have produced two E_g values caused due to two separate intrinsic VB and CB energy domains despite synchronization. This was reduced on coating with photosensitive GO sheets unlike the pristine lattice of LSNRs and GO (Fig. 8b and c). The two bandgap values of zinc-doped Co_3O_4 nanoparticles calculated by the Tauc plot method are reported.[80,81]

The 2nd E_g values of 1.88, 2.38, 2.28, and 2.23 eV for $B@Nd_2S_3$:GO, $B@Eu_2S_3$:GO, $B@Er_2S_3$:GO, and $B@Yb_2S_3$:GO have predicted the effects of covalent bond of Ln^{3+} with S^{2-}, including the secondary bond of Gd^{3+}. The electrons of 4f orbitals of Ln^{3+} and also of Gd^{3+} individually absorb the $h\nu$ from light and reach the respective CB spaces developing two E_g values. Therefore, the doping has generated a mild band with low E_g values with longer λ that contributed to the PCR in a shorter time. The Gd^{3+} split E_g from VB_{LSNR} to CB_{LSNR} and $VB_{Gd^{3+}LSNR}$ to $CB_{Gd^{3+}LSNR}$ for Ln^{3+} and Gd^{3+} respectively.

$B@Nd_2S_3$:GO, $B@Eu_2S_3$:GO, $B@Er_2S_3$:GO, and $B@Yb_2S_3$:GO have E_g values in the range of 4.05–2.23, 4.02–2.28, 4.03–2.38, and 3.97–1.88 eV respectively, which altered the intramolecular activities for PCR (Fig. 8c). Thus, the doping has favourably integrated the resulting holes to access the dye.[82]

3.6. HR-TEM analysis

The HR-TEM images elucidated the S^{2-} and Ln^{3+} sites of LSNRs on integrating the wavevector. B@LSNR with $\psi_{Gd^{3+}}$ and $\psi_{S^{2-}}$
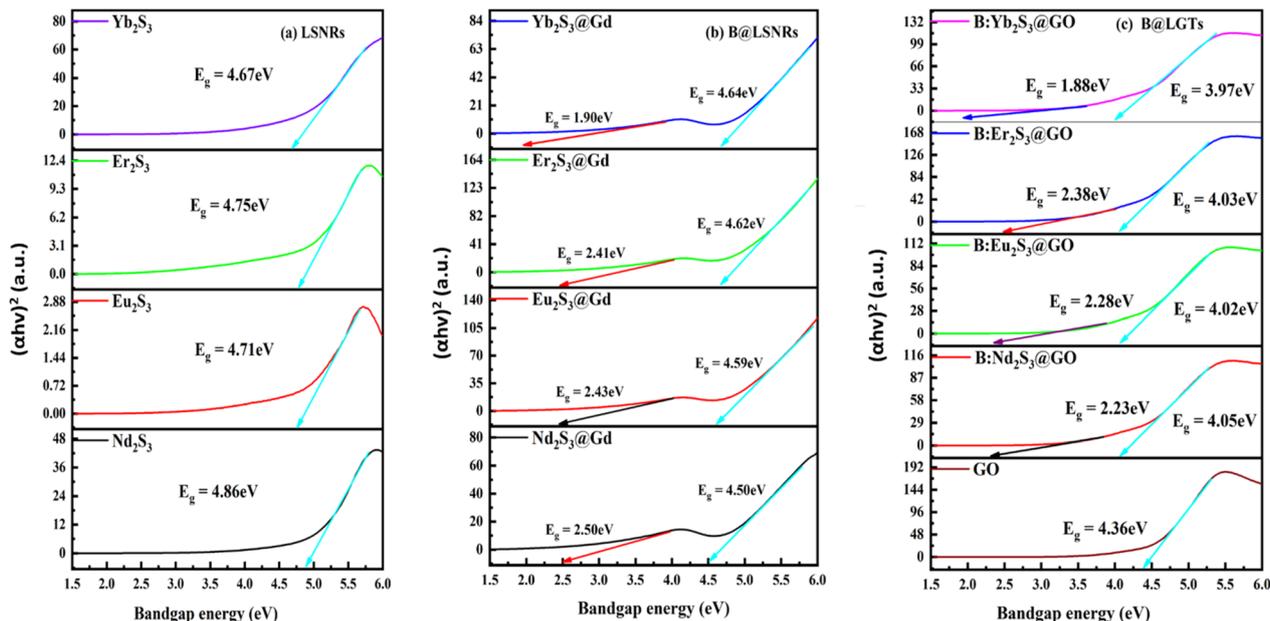
Fig. 8 E_g spectra from the Tauc plots for (a) LSNR, (b) B@LSNR and (c) GO and B@LGTs.

align in bunches of 100 nm size as the adhesive $\geq$ cohesive forces is depicted with the PCPs in Fig. 9 and 18–20. Thon ring pattern *via* Fourier transform has predicted the equalisized surface charges of terminal S^{2-} by aligning them through the consistent cohad points (CCPs) for receiving the $h\nu$. The B@LGTs have streamlined to astral morphology *via* central internodes due to enlarged surface area. This depicted that the 2D GO sheets probably align along the NR to occupy an adequate space for oscillations for getting synchronized, where each coated NR seem to synchronize the $h\nu$ receptance and aligning the resultant holes by gaining the least E_a to avoid the electron–electron collisions, avoiding the recombination. This mechanism has also generated the higher surface area depicted with the BET supporting a monolayer adherence of solvated dye and adsorption of its reduced form. Thus, the friccohesity for 0.014 to 0.012 S cm^{-1} of LSNR to B@LSNR indicated the clubbed NRs with longer λ_{max} (Fig. 20). The B@LGTs are confined to a central point from 20 to 100 nm. Selected area electron diffraction (SAED) depicts the 2D electron diffraction patterns of Nd_2S_3, B@Nd_2S_3, and B@Nd_2S_3:GO NRs with concentric rings indexed as (211), (310), (321), (001), and (420) lattices to elucidate the uniform wavevector (Fig. 9a(i), b(i), and c(i)). This observation has inferred that the dopant and coating have been conjugated as a single structure. The $\pi \rightarrow \pi^*$ of FGs and FEs seem to get fitted with the oxidation and reduction potential of Ln^{3+} and S^{2-} respectively. The Gd^{3+} dopant has induced the oscillations by attracting the S^{2-} from primary bond with the Ln^{3+}. The sharper SAED patterns of Nd_2S_3, B@Nd_2S_3, and B@Nd_2S_3:GO NRs than others have predicted the sharing of their lattices with dopants as new wavevectors. The dopant has developed new lattice planes, depicting resolved NRs with a higher surface area, and GO coating has further enhanced the surface area with highly systematized planes,

depicted with the BET sharper SAED (Fig. 6). The HR-TEM has predicted the highly resolved surface area because the E_a values of LSNR and dopant both excite their electronic transitions within 1.88 eV energy domain to attain the same phase. Spatial lattice patterns are sharpened for Nd_2S_3, B@Nd_2S_3, and B@Nd_2S_3@GO as dopants and coating have reoriented their lattices proven with their SAED. From the HR-TEM images of Nd_2S_3, doped, and coated, the coated B@Nd_2S_3@GO has developed a prominent node (Fig. 9c). Based on the HR-TEM and XRD input, the possible structural linkages are developed (Fig. 10). Gd^{3+} seems to attract the terminal S^{2-} to join with this, while the NRs seem to wrap with the GO by intensifying the concentric arrangement of electrons. The angular momentums for $4f^{3e}$ of Nd_2S_3 might have intermixed to adjoin a centre of internode. The B@LGTs with the optimized lattice in 20–100 nm have expressed the distinctive $h\nu$ transforming activities[83] to holes (Fig. 9). The sharper edges anchor a direct conduction due to a relatively high surface area, improved hole absorption, and chemical sensing abilities. B@Eu_2S_3:GO, B@Er_2S_3:GO, and B@Yb_2S_3:GO have all the constituents common except increasing 4f electrons that have aligned the overall morphology (Fig. 9f, i, and l). Such critical 4f electron-driven interstitial interfacing has never been reported yet where the spins of increasing 4f electrons with B@LGTs have been expressing the molecular activities. The B@Eu_2S_3:GO has aligned divergently on optimizing its lattices while the B@Er_2S_3:GO as tiny divergence occurred due to difference in their 4f electrons. The B@Yb_2S_3:GO has inferred the sharper and cloudy dimensional edges due to closely spaced alignment (Fig. 9l). The 4f electrons from the VB to the CB face collisions despite the same energy levels and such collisions occur with B@Yb_2S_3:GO than others. B@Eu_2S_3:GO with infinite collisions optimized the energy to synchronize to the same energy states (Fig. 9f).

Fig. 9   HR-TEM images of (a–c) Nd_2S_3, $B@Nd_2S_3$, and $B@Nd_2S_3$:GO with (a(i), b(i), c(i)) their SAED pattern; (d–f) Eu_2S_3, $B@Eu_2S_3$, and $B@Eu_2S_3$:GO; (g–i) Er_2S_3, $B@Er_2S_3$, and $B@Er_2S_3$:GO. (j–l) Yb_2S_3, $B@Yb_2S_3$, and $B@Yb_2S_3$:GO, respectively.

3.7. XRD analysis

XRD analysed the crystalline structures (Fig. 10). The d-spacings of Nd_2S_3 are 0.85, 0.61, 0.55, 0.49, 0.38, 0.32, 0.30, 0.28, 0.22, and 0.18 nm corresponding to the planes (011), (022), (012), (112), (013), (123), (004), (033), (025), and (245) at 10.47°, 14.28°, 15.94°, 18.00°, 23.5°, 27.5°, 28.78°, 32°, 40.4°, and 50.5

respectively. The d-spacings of Eu_2S_3 with 0.93, 0.55, 0.31, 0.30, 0.27, 0.22, 0.20, and 0.18 nm correspond to (011), (012), (123), (004), (033), (025), (225), and (245) at 9.44°, 16.07°, 28°, 29.3°, 32.5°, 41°, 43.44°, and 50.5° respectively. The d-spacings of Er_2S_3 with 0.93, 0.30, 0.26, 0.18, and 0.15 nm correspond to (011), (004), (124), (045), and (445) at 9.46°, 29.28°, 34°, 48.75°, and 57.9°, respectively. The d-spacings of Yb_2S_3 with 0.93, 0.46, and 0.30 nm correspond to (011), (134), and (004) at 9.50°, 18.99°, and 29.07°, respectively (Fig. 10). The d-spacing values for LSNRs have been found within a common range to critically authenticate the similar lattice framework with the similar wavevector generating a non-shifting bandgap. The peaks at 2θ values as per 4f electron consolidate the crystallographic planes with the corresponding d-spacing indexed as 1D NRs (Table S12†). The positions of XRD peaks are slightly changed with few diffraction lines and are close to the standard JCPD cards. The XRD profiles of Nd_2S_3, Eu_2S_3, Er_2S_3, and Yb_2S_3 are in agreement with the standard JCPD cards (01-081-0924),[84], (JCPDF#26-1419),[85], (00-021-0324)[86,87] and (65–2373)[88,89] respectively. The energies of $4f^{3e}$ and $4f^{6e}$ with Nd_2S_3 and Eu_2S_3 split [90] into more peaks than those of Er_2S_3 and Yb_2S_3 to distinguish a role of their more unfilled suborbital and more filled suborbital expressed as ψ_n as $n_{Nd_2S_3} > n_{Eu_2S_3}$.[21,91] The sharpened cps from VB to CB had predicted the infinite nodes of the similar frequencies used to calculate resultant energy as

$$\psi_n = \sqrt{\frac{a}{2}} \sin \sqrt{\frac{n\pi x}{a}} \qquad (2.7)$$

Nd_2S_3 and Eu_2S_3 with sharper peaks indicate almost equal eigen energies unlike the hedgy split of nearly filled $4f^{11e}$ and $4f^{13e}$ of Er_2S_3 and Yb_2S_3 respectively[92] (Fig. 10a). Enhanced peak intensities with B@LSNR lattice planes compared to the LSNRs indicated chargewise intensified and stabilized hole-generating sites (Fig. 10b). $B:Nd_2S_3@GO$, $B:Eu_2S_3@GO$, $B:Er_2S_3@GO$, and $B:Yb_2S_3@GO$ have all the constituents common with $4f^{3e}$, $4f^{6e}$, $4f^{11e}$, and $4f^{13e}$ respectively. This predicts that a variation in 4f electrons has substantially aligned the overall morphologies due to enhancing spins. $B:Yb_2S_3@GO$ is a flower petal-like structure, in which the NRs have been aligned divergently. $B:Er_2S_3@GO$ developed a tiny structure, while $B:Yb_2S_3@GO$ developed a cloudy morphology with sharper diverging NRs. The $4f^{@e}$ from the VB to the CB also faces collision despite the same $4f^{@e}$ energy levels. Such partial collisions are nil with $B:Yb_2S_3@GO$ while $B:Eu_2S_3@GO$ seems to face much collisions, optimizing the energy to synchronize the same energies. Their spin intensity predicts the nodal plan (n) and its values are used to calculate ψ_n using eqn (2.7). At a higher d spacing with Nd_2S_3, there are

Table 2 Coulombic forces on increasing the 4f electrons

Ln^{3+}	# Electrons	# Protons	Coulombic force
Nd^{3+}	57	60	48 410.51
Eu^{3+}	60	63	53 506.35
Er^{3+}	65	68	62 565.63
Yb^{3+}	67	70	66 387.51

prominent planes and Eu_2S_3 also developed the (001) plane on shifting from $4f^{3e}$ to $4f^{6e}$ (Fig. 10a and b). These predict the role of contraction effect, where increasing the electrons in the same orbital lowered their atomic radii. However, no such data have been reported yet, but their behaviour is observed similar to the transition metals (Table S28†). On increasing the $4f^{@e}$ from Nd_2S_3 to Eu_2S_3 has generated the corresponding planes at specific 2θ values. That had predicted an influence of nuclear charge being applied on the Ln^{3+} and S^{2-}. These results are also supported by the TGA and UV/vis spectroscopy (Fig. 7 and 15). Upon increasing the number of 4f electrons within the same shell, a more nuclear charge is applied on them (Table 2). Thus, for estimating the values of atomic radii of LSNRs from Nd^{3+} to Yb^{3+}, the coulombic forces are generated as follows:

$$\text{Coulombic force} = \frac{q_{Ln^{3+}}^{\text{no. of protons}} \times q_{Ln^{3+}}^{\text{no. of electrons}}}{4\pi\varepsilon r^2} \qquad (2.8)$$

r = Bohr radii = 0.0529 nm, ε = 78.4 for H_2O at 25 °C. The higher is the attractive force, the lower is the radii (1/attractive force). The Er_2S_3 and Yb_2S_3 have developed the same planes except (012) that appeared with Nd_2S_3 due to a slightly higher nuclear charge, affecting an overall lattice wavevector (Fig. 10a). The planes with Yb_2S_3 appeared at 9.50°, 18.99°, and 29.07° compared to others (Fig. 10a).

Probably, Yb_2S_3 with $4f^{13e}$ developed a stronger nuclear charge on Yb^{3+} strongly affecting the position of S^{2-} in the Yb_2S_3 lattice. Second, no peaks appeared at higher 2θ values with Yb_2S_3 as $Yb^{3+}–S^{2-}$ seems to have the strongest potential energy. Thus, no multiple rotation, vibration, and translations are possible at higher 2θ values. The $[Yb^{3+}]^2[S^{2-}]^3/4\pi r^2$ with Yb_2S_3 have observed the maximum peaks at lower 2θ values while at higher 2θ values no peaks. Thus, the no collisions have occurred due to one UPE of Yb_2S_3 than the $4f^{14e}$ fully 4f field orbital. Fundamentally, the same energy levels for the 4f orbitals with degeneracies on increasing the electrons could be compared with the XRD intensity and d spacing pattern (Fig. 10c). Thus, 0.88 nm d spacing of GO compared to 0.34 nm of Gt indicates the interfacial forces working among their primitive cells or lattices. The d spacing of Gt is almost 3 times that of GO, as Gt has the C–C framework of primitive cells with stronger PE > KE without oscillating its energy than that of GO sheets with equal FG distribution (Fig. 10c). The FGs of different electron densities are bonded, which are mutually shared with the main lattice; hence, they expand with the covalent bonds increasing the d spaces. Similarly, an increase in the 4f electrons has resulted in an increase in the nuclear charges within 4f orbitals. The functionalisation of GO has increased the d spacing with a wider distribution compared to the sharper one with Gt (Fig. 10c). Gt has a uniform lattice with 100% equipartition that responds to a laser light without collisions with ψ_{sv}. However, GO with 2θ from 11° to 21° values synchronized the oscillation of the FGs, where the O atom dominates (Fig. 10c). Such lattice elements have synchronised the d spacing to 0.88 nm with 10 900 cps against 85 000 with Gt. Gd^{3+} with Er_2S_3 and Yb_2S_3 has slightly changed the peaks unlike Nd_2S_3 and Eu_2S_3 on equipartitioning the lattice of LSNRs. The XRD data for rhodium sulfide and its doping with Cu, Fe, Co, and Ni with some extra
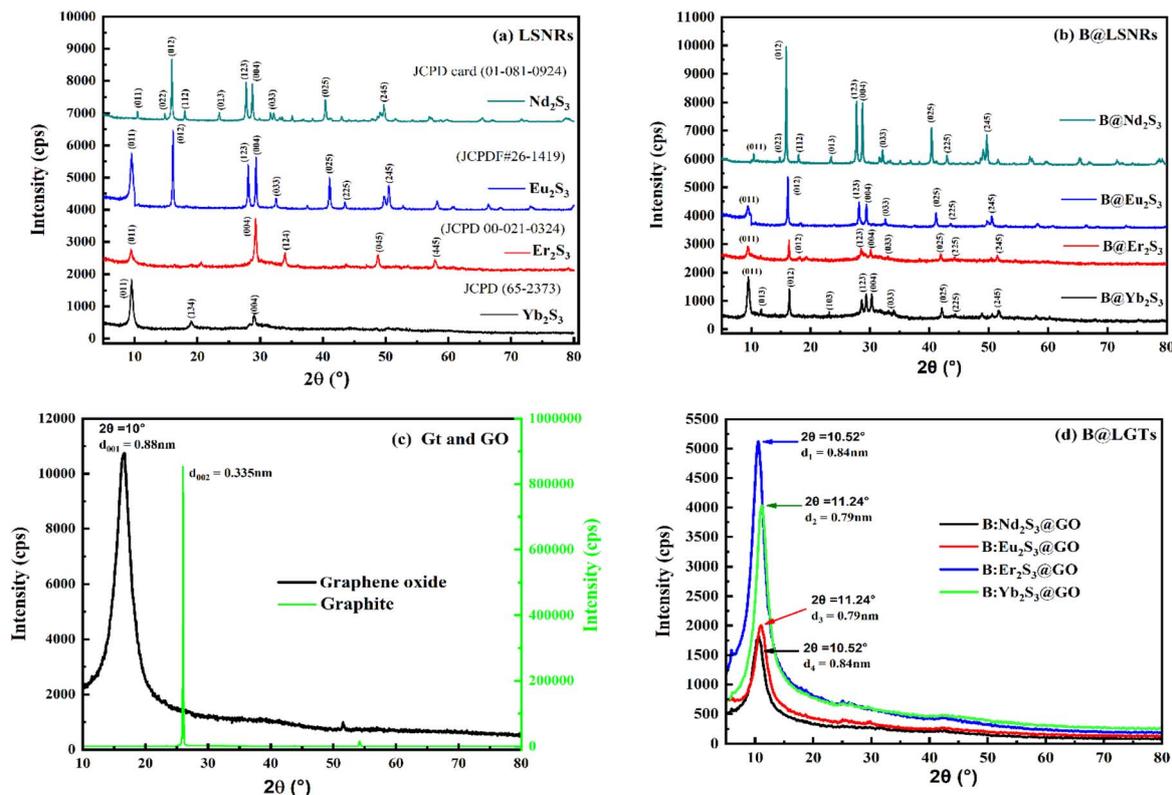
Fig. 10 XRD spectra elucidating the *d* spacing and diffraction planes at 2θ values for (a) LSNR, (b) B@LSNR, (c) GO and Gt and (d) B@LGTs.

peaks are reported.[93] Nearly fully filled 4f electrons have effective LSNR matrices with Gd^{3+} due to a $4f^7$ half-filled suborbital. The shift in peak position has occurred with a lower angle on strain in doped nanomaterials, as reported elsewhere.[94] Hence, Gd^{3+} doping with the LSNRs could not disrupt a native lattice of LSNRs except enhancing the intensity by ∼3000 cps (Fig. 10a and b). Thus, Gd^{3+} has been accommodated with lattices of respective LSNRs as the FGs become the constituents of the main lattice of GO. Though the Gd^{3+} did not destabilize the main lattice of LSNRs, the Ln^{3+} and S^{2-} have developed stronger covalent bonds, while Gd^{3+} has been the competent dopant to dent their PE with a new state of B@LSNRs. The increments in the intensities of lattices indicated that the repulsion between Gd^{3+} and Ln^{3+} is equal to the attraction between the $2Gd^{3+}$ and $3S^{2-}$ ions. This had maintained the consistency in the lattice planes without generating a new lattice with no effect in *d* spacing. Therefore, Gd^{3+} has effectively aligned the LSNRs by attracting the terminal S^{2-} (Fig. 9 and 12). The GO coating reoriented and aligned the lattice planes of B@LSNRs, the GO plane with their 0.88 nm d spacing was the main plane at 2θ = 10.52–11.24° (Fig. 10d). However, the intensities have been reduced to half values. The structuredness expressed as manifolds state was attained with the energy partitioning. Their intensities are as B:Er_2S_3@GO > B:Yb_2S_3@GO > B:Eu_2S_3@GO > B:Nd_2S_3@GO with $4f^{11e}$, $4f^{13e}$, $4f^{6e}$, and $4f^{3e}$. The variable factors with XRD intensities and *d*-spacing are the 4f electrons that have substantially synchronised the planes of the B@LSNRs, to the plane of GO (Fig. 10c and d). The said synchronisation of

their planes predicts that the FGs and FE both with −ve and +ve centres of B@LSNRs have substantially interacted to split their residual energies (Fig. 15).

3.8. Raman spectroscopy analysis

Raman laser elucidates the structural defects of B@LGTs that have variable intrinsic energies synchronized as intense D and G bands, unlike the pristine matrices.[61] Laser becomes relevant to analyse an equipartitioning of energies caused on aligning Gd^{3+} and GO in the matrices of LSNRs expressed as follows:

$$\text{laser} \rightsquigarrow \text{B@LGT} \rightarrow I_D + I_G + I_{2D} \qquad (2.9)$$
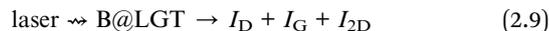
The intensities (*I*) of D, G, and 2D bands with GO at 1373, 1597, and 2750 cm^{-1} respectively have inferred a consolidation of the electronic activities of FG and π conjugation ($sp^2 \rightarrow sp^3$). That had rationalized as $I_D/I_G = 0.86 < 1$ along with a mild

Table 3 Raman shifts with D and G bands and ratios for GO and B@LGTs

LSNR@GO	D-shift (cm^{-1})	G-shift (cm^{-1})	I_D/I_G
GO	13 238	15 462	0.86
B:Nd_2S_3@GO	19 532	20 470	0.95
B:Eu_2S_3@GO	12 498	13 546	0.92
B:Er_2S_3@GO	12 614	13 448	0.94
B:Yb_2S_3@GO	34 406	37 386	0.92

modulation bump of 2D band against D and G bands[61] (Fig. 10). The integrated G band with E_{2g} induced the electronic activities from $sp^2 \rightarrow sp^3$ with an apex as disordered GO with a sharper D

band on localized synchronization among the tiers. The B@LGTs with higher $I_D/I_G = 0.93 < 1$ than GO has further inferred an induction of more energy domains integrated to sharper D bands than a pristine GO[8] (Fig. 11 and Table 3). B@Er$_2$S$_3$:GO with sharper D and G intrinsic intensities detected with Raman laser are correlated with IR stretching of S^{2-} and bonded with Ln^{3+} in matrices of LSNR via double and single bonds. Er^{3+} of B@Er$_2$S$_3$:GO has $4f^{11}$ electrons, $i.e.$ neither half nor a fully filed orbital causing the prominent individualistic energy domain within a structure responsible for effective photocatalysis and physicochemical interactions, While GO despite being a single 2D sheet has also developed the spontaneities due to localized FG and FE activation, which could be due to twisting or distortions but these are negligible compared to B@Er$_2$S$_3$:GO and others (Fig. 11b). Therefore, a GO coating has tremendously consolidated the electronic excitations in response to the Raman laser with robust phonon generation of the specific frequencies integrated to overall single energy value (Table 3). Such response of Raman laser could be aligned with the FT-IR spectra where the Fingerprint region is slightly intensified over stretching on coating due to the streamlining of the surface charges. The $4f^{13e}$ of B@Yb$_2$S$_3$:GO with lower intensities and large d-spacings strengthened synchronization with GO aligning the charges (Fig. 10d and 12b). The surface energies of B@Er$_2$S$_3$:GO are enhanced, causing inelastic incoherent neutron scattering depicted by symmetric IR with the moderate Raman activity. B@Nd$_2$S$_3$:GO and B@Eu$_2$S$_3$:GO upon integrating to synchronized interstities photocatalytically reduced BBR, TMIs, and QHIn in a shorter time (Fig. 11b). Raman spectra with incident laser have predicted a stronger communication of $4f^{@e}$ with GO oscillations. Thus, the incident laser indicates a stronger dipole moment for B@Er$_2$S$_3$:GO with maximum D and G intensities as surface plasmonic resonance (SPR).[95] The D and G bands with B@LGTs infer Rayleigh scattering due to the aligned GO sheet. However, B@LGTs with interstitial tiers on the aligned matrices of variable $4f^{@e}$ by minimizing the $h\nu$ bouncing photocatalytically reduced BBR, TMIs, and QHIn in 15–40 min. Considering the expeditious photocatalytic activities of B@Eu$_2$S$_3$:GO and B@Yb$_2$S$_3$:GO, the possibility could be explored to replace Gd^{3+} with Pd, Ag, Pt, and Au noble metals.[96] These metals could intensify the sharper D and G bands of B@Er$_2$S$_3$:GO and B@Nd$_2$S$_3$:GO enhancing $4f^{@e}$ interactions with FGs on stabilizing the dipoles (Fig. 11b). The $4f^{6e}$ and $4f^{13e}$ of B@Eu$_2$S$_3$:GO and B@Yb$_2$S$_3$:GO distract alignment on electronic collisions unlike $4f^{11e}$ and $4f^{3e}$ of B@Er$_2$S$_3$:GO and B@Nd$_2$S$_3$:GO respectively. The FGs with $4f^{@e}$ regulated on quenching the undesired stretching with higher polarizability (Fig. 11b). Nd$_2$S$_3$ at 200 and 300 cm^{-1} has attributed to E_{2g} and A_{1g} bands,[97] while Er$_2$S$_3$ and Yb$_2$S$_3$ have broader bands at 390 and 400 cm^{-1} respectively. The Raman laser has excited the 4f electrons to oscillating intensities within 200–1200 cm^{-1}, where the prominent intensities with Nd$_2$S$_3$ at 196, 392, 831, and 984 cm^{-1} and also at 196 and 392 cm^{-1} have attributed to E_{2g} and A_{1g} bands respectively.[97] Eu$_2$S$_3$ has shown maximum intensities at 217, 469, and 846 cm^{-1} while Er$_2$S$_3$ and Yb$_2$S$_3$ at 370, 1000, and 450, 1000 cm^{-1} respectively. The more oscillating intensities at variable Raman shifts are prominent
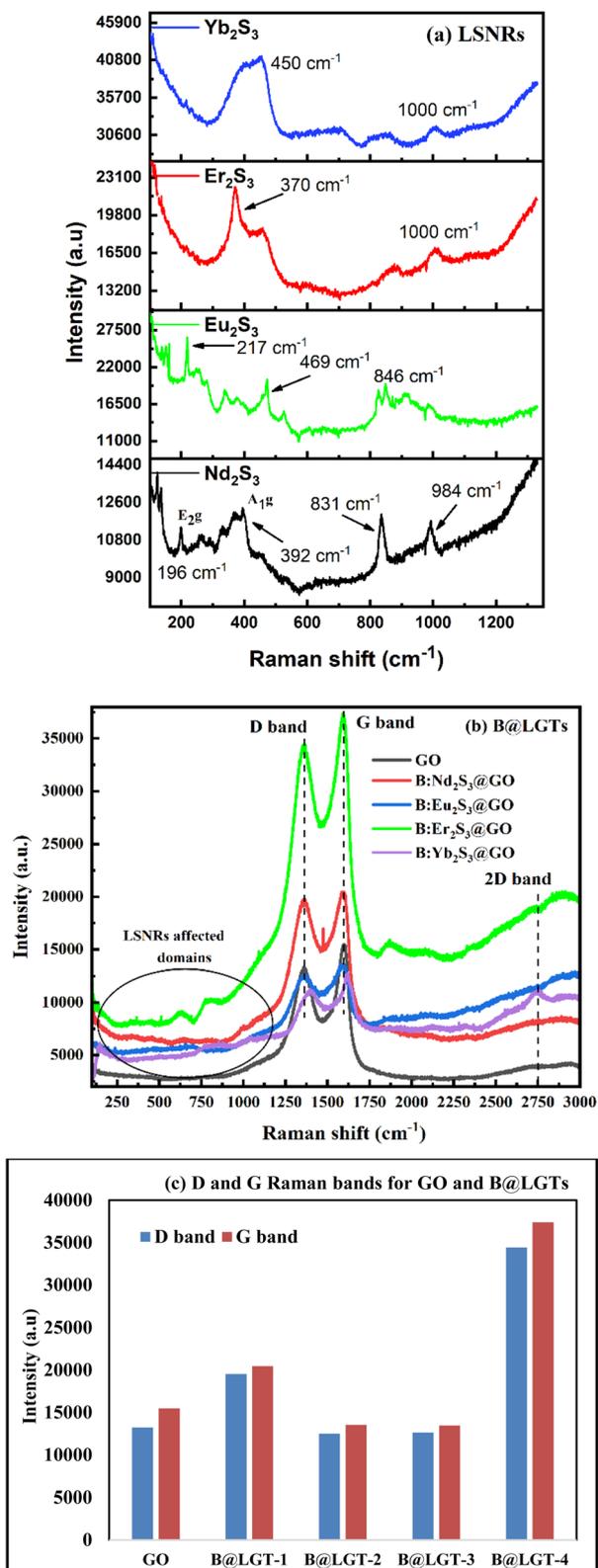
Fig. 11 Raman spectra for (a) LSNRs and (b) GO and B@LGTs elucidated the (c) D and G band intensities with $I_D/I_G < 1$.

with Nd_2S_3 and Eu_2S_3 having less than half-filled 4f electrons. Er_2S_3 and Yb_2S_3 have broader peaks at 370 and 450 cm^{-1}, where Yb_2S_3 from 316 to 510 cm^{-1} predict that the single 4f unpaired electron could not cause robust spins and collisions (Fig. 11a). A similar behaviour is predicted with B@Yb_2S_3:GO that had intensified a maximum PCR rate among the B@LGTs (Fig. 11). The LSNRs doped and coated have produced the well-defined D and G bands unlike LSNRs alone. The D and G bands predicted that the 4f electrons of Ln and dopant might have synchronized the oscillating activities of the GO sheet. The doping and coating of LSNRs have been fitted with surface-enhanced FRET to consolidate the electronic oscillations w.r.t. the structural constituents FGs and FE of the GO sheet.[30]

3.9. FT-IR analysis

FT-IR have tracked the 1071, 1400, 1250, 1750, and 1626 cm^{-1} bending and stretching frequencies for C–O–C, –CHO, >CO, –COOH, and –OH of GO and B@LGTs respectively.[61] This predicted that the said groups assist GO coating by aligning along B@LSNR. The broader peak for –OH at 3428 cm^{-1} infers free water molecules adhered with GO and B@LGTs (Fig. 12a). The peaks at 500–623 cm^{-1} and 697 cm^{-1} ascribed to Ln–S or Gd–S metal sulfide,[84] 1071–1400 cm^{-1} ascribed to C–O–C, –CHO, and >CO of the GO sheet and the bending at 3428 cm^{-1} for –OH, respectively[33] indicated the functionalisation of B@LGTs (Fig. 12b). B@LGT with aligned interstitial charges has absorbed maximum IR radiation for an energy storage with inelastic
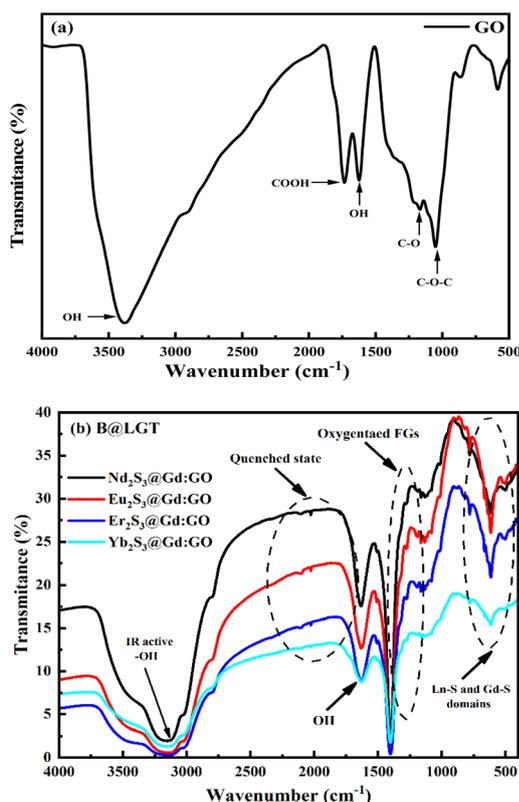

Fig. 12 FT-IR spectra Illustrating stretching and bending frequencies with (a) GO and (b) B@LGT with the increase in their 4f electrons.

ROCs.[23] The interfacing of the B@LGT with lithium or Ti metal could enhance the energy storage performance by further reducing the E_g with aligned electrostatic dipoles.[98] The B@LGTs by adsorbing H_2 could lower their ignition point for use as clean fuel. The B@LGT have intensified the bending and stretching in the fingerprint region[30] compared to GO with longer λ in the same φ (Fig. 12b). This also reoriented the H_2O dipoles with higher shear and surface tension (Fig. 18 and 19). The $O^{\delta-}$ of H_2O could have competitively realigned either with Gd^{3+} or Ln^{3+} sharpening the bending by lowering the stretching and stabilizing the electrostatic dipoles of interstitial tiers. The FGs of GO have been prominently stretching with negligible bending, as a fingerprint domain with GO is plain compared to B@LGTs (Fig. 12a). Thus, the 2D GO sheet could not be rotated, vibrated, and translated except stabilising the $h\nu$ receiving sites to oscillate with undesired activities and was chosen for coating. However, the stretching and bending patterns of LSNRs were harmonised compared to GO (Fig. S11a†). The GO stretching domains are active while the LSNRs normalised with bending unlike confined to a single value. However, the huge charge in bending on coating the B@LSNRs with GO seems to be the broader and undecided stretching despite that sharper with LSNRs (Fig. 11b). Hence, both the stretching and bending are largely modified on coating with GO, due to the spontaneities of both the GO and LSNRs for interfacing them (Fig. 12). Moreover, stretching and bending of B@LSNRs indicate a novel interface than LSNRs. The Gd^{3+} dopant has functionalised them where the stretching is broadened from 3600 to 3000 cm^{-1} (Fig. S11b†). Thus, the stretching of S^{2-} of LSNRs has become most active to stretch as well as to induce the exponential undistinguished bending credited to the response of S^{2-} to the Gd^{3+}, and at the same time, accommodating the covalent bond with Ln^{3+}. The dopant has substantially transformed the PE to eigenenergy elucidated with the HR-TEM and TGA (Fig. 9 and 15). The bending indicates the optimized B@LSNRs due to the energy distribution. However, the intrinsic stretching frequency of LSNRs from 1638 to 1405 cm^{-1} prove shifting via S^{2-} to accommodate Gd^{3+}.

The sharper bending pattern of manifolds from 500 to 1200 cm^{-1} appeared due to the metal sulfide bonding of LSNRs (Fig. S11a†). The LSNRs bending on doping with Gd^{3+} has also acted as the constituents for bending the B@LSNRs. The bending patterns of Gd^{3+} dopants with B@LSNRs have never been reported yet. Both S^{2-} and Ln^{3+} have shared their electron densities with Gd^{3+} unlike LSNRs alone. The 1700–2700 cm^{-1} indicate almost the normalised behaviour of B@LSNRs, which may be due to repulsion and attraction, where $[Gd^{3+}][S^{2-}]/4\pi r^2$ as $r_a = r_r$ (Fig. S11b†). These bending and stretching have introduced valuable ψ_{sv} to photocatalytically reduce the effluents. The frequencies with B@LSNRs broadened from 3600 to 2700 cm^{-1} than a straight line for LSNRs with 100% abs. It has predicted that the terminal $=S^{2-}$ and $-S^{2-}$ both are connected to the Gd^{3+} and have acquired almost similar KEs oscillating with similar frequencies. This is noted as $\psi_{B@LSNRs} = \int_{-\infty}^{\infty} \psi_{]S^{2-}} \times \psi_{eS^{2-}} dxdy = 1$ normalised than $\psi_{LSNRs} = \int_{-\infty}^{\infty} \psi_{]S^{2-}} \times \psi_{eS^{2-}} dxdy = 0$ orthogonal due to different intramolecular activities or oscillations synchronised with Gd^{3+}.

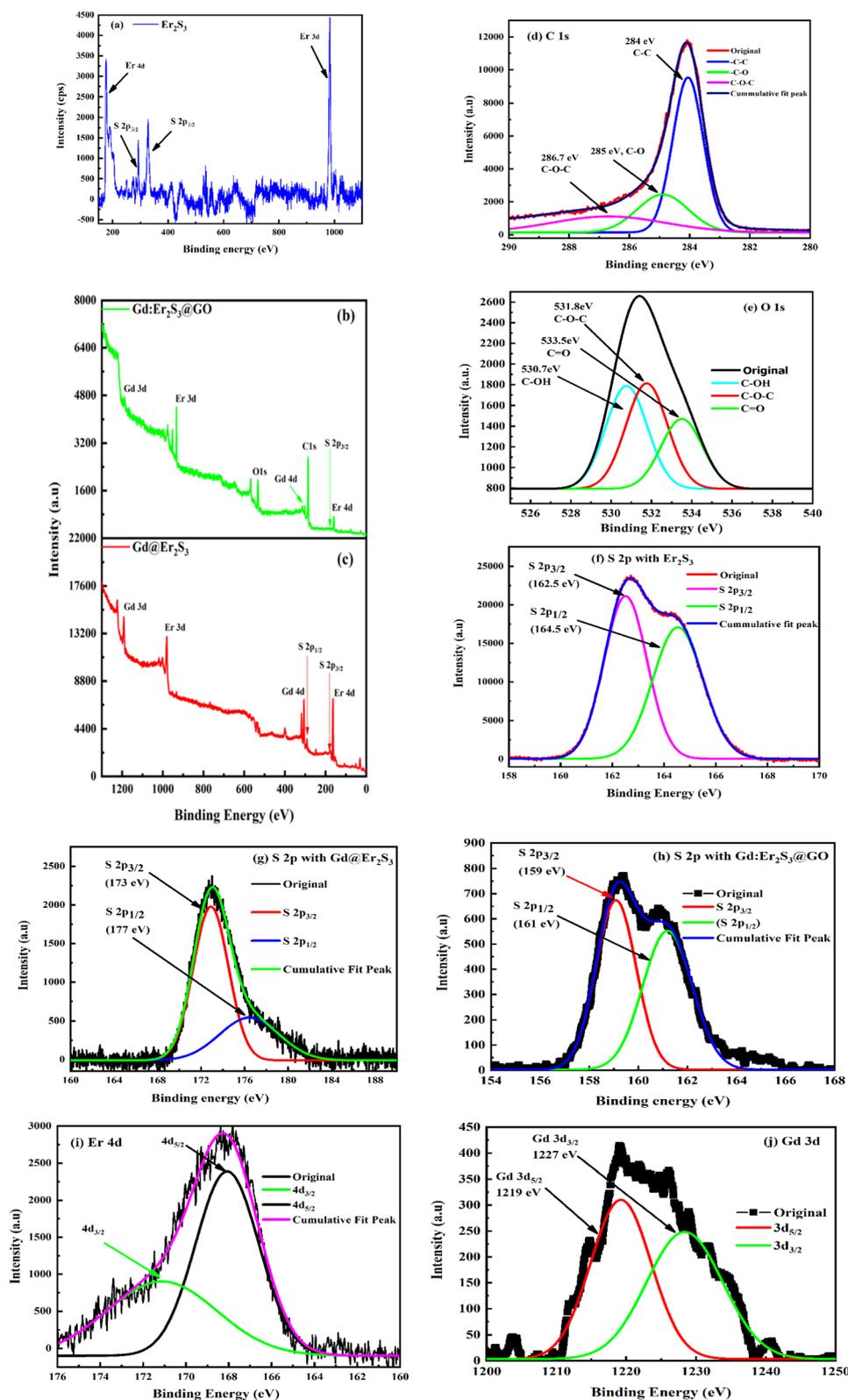**Fig. 13** XPS spectra: (a–c) survey scan for B@Er$_2$S$_3$ and B@Er$_2$S$_3$:GO; (d) C 1s and (e) O 1s of B@Er$_2$S$_3$:GO; (f–h) S 2p states; (i) Er 4d$_{3/2}$ and 4d$_{5/2}$ and (j) Gd 3d$_{3/2}$ and Gd 3d$_{5/2}$.

Gd^{3+} has functionalised the fingerprint region as well as the stretching domain of B@LSNRs (Fig. S11b†). The broader stretching frequency and fingerprint region have further been sharpened on coating because GO has established communication with Ln^{3+} and S^{2-} as well as Gd^{3+} on energy equipartition. Highly functionalised GO with stronger covalent bonds is not disrupted upon coating. Therefore, it has further sharpened the broader stretching domain of LSNRs as well as B@LSNRs (Fig. S11b†). The integrated GO sheets with FGs and FE equally resonate to transfer energy intimating the dopant and coating agents with intimated adherence with LSNRs. This has caused the stronger FRET generating ψ_{sv} on energy equipartitioning through the GO due to a sharper frequency at 1430 cm^{-1} and 1680 cm^{-1}. The GO has stabilised the molecules by normalising the bending frequencies due to a stronger link with the LSNR and Gd^{3+} to integrate the overall bending pattern as follows:

$$\int_{-\infty}^{\infty} B@LGTs = \int_{-\infty}^{\infty} \psi_{Gd^{3+}} \times \psi_{LSNRs} \times \psi_{GO} dxdydz = 1 \quad (3.0)$$

The bending energy pattern as B:Eu_2S_3@GO > B:Nd_2S_3@GO > B:Er_2S_3@GO > B:Yb_2S_3@GO indicates B:Yb_2S_3@GO as highly normalised due to $4f^{13e}$ than B:Eu_2S_3@GO with $4f^{6e}$. The sharpening at 1450 cm^{-1} indicates 100% equipartitioning as B:Nd_2S_3@GO, B:Eu_2S_3@GO, B:Er_2S_3@GO, and B:Yb_2S_3@GO have attained the undistinguishable energy states with instantaneous PCR without the energy ingredients (Fig. 12b). The stabilised bending has been supported by the Raman spectra, especially B:Er_2S_3@GO with a stronger D band at 35 000 cps. B@LGTs have gained normalised bending at 3100 cm^{-1} promoting the PCR and PCP activities with effluents than LSNRs and B@LSNRs (Fig. S11†).

3.10. XPS analysis

The XPS spectra of Er_2S_3, B@Er_2S_3, and B@Er_2S_3:GO analysed the oxidation state, elemental composition, and lattice energy. Their survey spectra indicate excitation of $4f^{11e}$ electrons shared with S^{2-} like Er^{3+} in Er_2S_3, while the 2p electrons resisted inner electronic activities as per the Compton effect.[99] Er_2S_3 with $2p_{1/2}$ and $2p_{3/2}$ states of the S at 162.58 and 164.58 eV respectively indicate optimized stability (Fig. 13f). The S 2p states (Table 4) have confirmed the structural stability of Er_2S_3 w.r.t. the core–shell electrons of lanthanides. The 4f electrons confined towards terminal sulfur atoms form double covalent bonds with specific binding energy.[30] Ln^{3+} is covalently bonded with S^{2-} while Gd^{3+} with a secondary bond on aligning the $4f^{@e}$ and 2p core electrons. Gd^{3+} with B@Er_2S_3 has broadened the $2p_{1/2}$ and $2p_{3/2}$ peaks at 177 and 173 eV respectively for the S atom than

Er_2S_3 alone (Fig. 13g). The broadening inferred that their spins noted as angular momentum could have been shared through repulsion and attractions charges in the LSNR matrices. Thus, the $2p_{1/2}$ and $2p_{3/2}$ energy states for S^{2-} increased with Gd^{3+} on realigning the matrices of Er_2S_3 and on increasing the unpaired $4f^{@e}$ with a higher binding energy of S^{2-} with 18–60% wt loss at 100–500 °C (Fig. 15).[100] The interstities of B@Er_2S_3 have broadened the peaks with a higher electron density than that of Er_2S_3 alone. The sharper peaks of lower intensity with B@Er_2S_3:GO are noticed. The FGs with $\psi_{Gd^{3+}}$, $\psi_{Ln^{3+}}$, and $\psi_{S^{2-}}$ interstities have equalized the lattices. B@Er_2S_3:GO with aligned charges enhanced the binding energy of S^{2-} from 164.58 to 177 and 162.58 to 173 eV of $2p_{1/2}$ and $2p_{3/2}$ respectively due to Gd^{3+} (Fig. 13h). Gd^{3+} has enhanced the peak intensity of B@Er_2S_3 with least E_g and a higher surface area than Er_2S_3 analysed with BET (Fig. 6 and 8). The higher electron density of B@Er_2S_3:GO decreased the binding energy from 177 to 161.12 and 173 to 159 eV of $2p_{1/2}$ and $2p_{3/2}$, respectively (Fig. 13 g and h). The C 1s spectra of B@Er_2S_3:GO at ~284, 285, and ~286.7 eV for C–C, C–O, and C–O–C respectively with stronger stability of respective bonds indicate intense hybridization[61] (Fig. 13d). The O K-edge with B@Er_2S_3:GO indicate C–OH, C–O–C, and C=O groups at ~530.7, ~531.8, and 533.5 eV respectively due to stronger O linkages than the GO alone[61] (Fig. 13d). The reduction of 532 eV of O 1s with GO to 530 eV with B@Er_2S_3:GO implied the O participation due to its electronegativity with the oxidation potential of dopant Gd^{3+} (Fig. 13e). The electron density of O with B@Er_2S_3:GO is higher with a broader peak for C–O–C at 531.8 than with GO.[30] Thus, the GO interactions have conjugated it with B@LGT than GO alone due to a higher PE. The higher binding energy for O of B@Er_2S_3:GO indicates the interfacing of FGs with LSNR matrices and dopants (Fig. 11). Thus, the C 1s and O 1s spectra have split at 530 eV due to FGs and $4f^{@e}$ vis-à-vis Gd^{3+} $4f^{7e}$ on strengthening a nuclear charge than GO alone[30] that agrees to literature values.[71,101] From 164.58 to 177 eV for Er_2S_3 of B@Er_2S_3 indicated the conjugation of Gd^{3+} with Er_2S_3 matrices via S^{2-} as the primary bond with

Table 4 Binding energies of the S atom for Er_2S_3, B@Er_2S_3, and B@Er_2S_3:GO

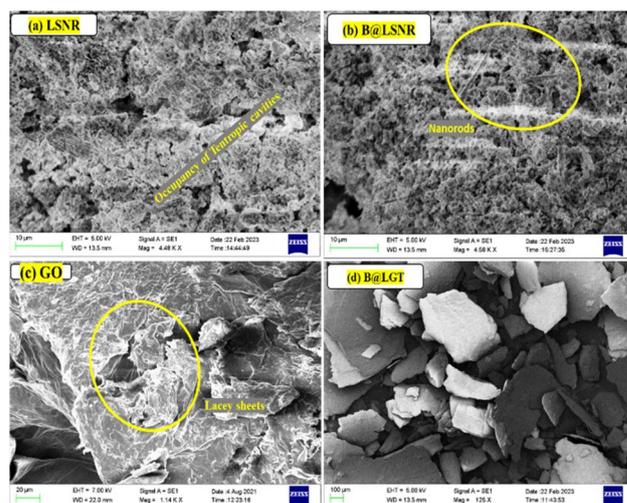| S (O.S)	LSNR	B@LSNR	ΔBE_{2-1}	B@LGT	ΔBE_{3-2}
S $2p_{1/2}$	164.58	177	12.42	161.12	−15.88
S $2p_{3/2}$	162.58	173	10.42	159	−14.00

Fig. 14 SEM images of (a) LSNR, (b) B@LSNR, (c) GO and (d) B@LGT morphologies.

Ln^{3+} and secondary with Gd^{3+} (Fig. 13f and g). The survey scans have elucidated the elemental compositions with various binding energies (Fig. 13a and c). The O 1 s with GO and $B@Er_2S_3$:GO at 530.86, 532.64, 533.88, and 530.7, 531.8, 533.5 eV for C–OH, C–O–C, and C=O respectively[30] indicate interstitial lattice with slightly less electron densities (Fig. 13d). Energies of 168.05 and 171 eV for $4d_{5/2}$ and $4d_{3/2}$ respectively for Er of $B@Er_2S_3$:GO than $\sim$1227 and $\sim$1219 eV for $3d_{3/2}$ and $3d_{5/2}$ respectively for Gd^{3+} have predicted the integrated interstities (Fig. 13j). Gd^{3+}, a dopant, has shared the PE in attraction for S^{2-} and repulsion for Ln^{3+} of matrices. The 3d and 4d electron spins attain stable interstities with dopants and GO responds to the $h\nu$ for hole generation.[30] The spectra for Er^{3+} and Gd^{3+} with 4d and 3d for $B@Er_2S_3$:GO with distinct binding energies of respective core electrons have exponentially enhanced their spins on sharpening the D and G bands supported by Raman intensities[78,102] (Fig. 11). The sharp peaks of Gd at $\sim$1227 and $\sim$1219 eV for $3d_{3/2}$ and $3d_{5/2}$ states, respectively, with $B@Er_2S_3$:GO indicate spin orbital coupling[71,101] (Fig. 13j). The spectra for Er^{3+} and Gd^{3+} with 4d and 3d with the $B@Er_2S_3$:GO resemble as dopant harmonized the electronic state of Er_2S_3.[78]

$$\Delta BE_{B@Er_2S_3-Er_2S_3} = \Delta BE_{2-1},\ \Delta BE_{B@Er_2S_3:GO-B@Er_2S_3} = \Delta BE_{3-2}$$

3.11. SEM analysis

SEM images have depicted the LSNRs and GO constituent integrated as B@LGT as a lace-like thin sheet of 10 and 100 μm morphology with a higher surface area with oscillating interlinks. The LSNR with uniform surface charges differ from B@LSNR of 2–10 μm *via* oxidation potential-driven linkages attained due to Gd^{3+} dopants (Fig. 14a and b). B@LGT on receiving the $h\nu$ with oscillating intensified interstities (I) profiled oscillating energies as follows:

$$I = [\psi_{Ln^{3+}} \times \psi_{S^{2-}}] + [\psi_{h^+} \times \psi_{e^-}]\ \text{and}\ |\psi_{LSNR}|^2\ \text{and}\ |\psi_{GO}|^2 \quad (3.1)$$

The monodisperse B@LTs were aligned similarly while the rough surfaces elucidated the uniform GO multilayers compared to GO alone (Fig. 14c and d). SEM elucidates the continuous networking of LSNR and GO sheets while the B@LGTs have been organized as a prominent integrated surface area in an intense smooth dimension. This established a close contact with the effluents for photocatalytic reduction, after PCR effluents get adsorbed onto B@LGTs. The B@LGT as an NR fibril network with activated surfaces has enhanced the photocatalytic reduction of BBR, TMIs, and QHIn. The integrated smooth sheet-like structure predicted that the interstities might have been staggered to intimate aligning despite the different energies but in the same φ. The square-like morphology of B@LGTs compared to the wire-type network distinguishes the role of the GO sheets, which have surrounded the B@LSNR. The morphological expression has been the function of the internal structural network in close contact on equipartitioning the energy through FRET (Fig. 14).

3.12. Elemental analysis

The C, H, and S elements with GO and B@LGTs both indicate that the coating is a chemical process on developing the

Table 5 Elemental analysis of GO and B@LGTs

Systems	C (%)	H (%)	S (%)	Wt (mg)
GO	60.558	3.306	—	1.0752
Nd_2S_3@Gd:GO	39.808	3.147	0.890	1.004
Eu_2S_3@Gd:GO	41.629	2.818	0.936	1.234
Er_2S_3@Gd:GO	40.978	3.098	0.797	1.365
Yb_2S_3@Gd:GO	41.698	2.381	1.045	1.380

uniform interstities with energy equipartitioning. Their values were detected using an elemental analyser and an XPS analyser (Fig. 13). Table 5 presents higher C% with GO alone than in the doped state in 1.5/1.0 ratio. Thus, almost 50% GO was doped when B@LSNR:GO = 1 : 6. Interestingly, B@LGTs from Nd_2S_3@Gd:GO to Yb_2S_3@Gd:GO have similar C% and H% with $\pm$0.5% and $\pm$0.2% variations respectively, though this variation with S is $\pm$0.1% (Table 5). Therefore, all the B@LSNRs have doped almost a similar GO amount due to similar interacting sites. It is also depicted with their similar N_2 adsorbing and desorbing rates with BET analysis (Fig. 6). Thus, their structural geometry is thermodynamically and quantum mechanically stable, and hence, they are used as photocatalysts with manifold reusability.

3.13. ICP-OES of LSNRs, B@LSNRs, and B@LGTs

First, 2 mg/100 mL of each LSNR, B@LSNR, and B@LGT was sonicated at 28 kHz in a conical flask for 2 h. It was washed twice with warm water and centrifuged, and later, a homogenized solution was prepared for ICP-OES analysis. Initially, 2, 4, 6, 8, and 10 ppm standard solutions were prepared by mixing 0.2, 0.4, 0.6, 0.8, and 1 mL of each of $NdCl_3$, $EuCl_3$, $ErCl_3$, $YbCl_3$, and $GdCl_3$ salts out of their 1000 ppm stock solutions for calibration.

The intensity *vs.* amount of respective metals with 1st order obtained on regression with residual coefficient (R^2) values between 0.973964 and 0.992382 (Fig. S15†) have inferred accuracy. The Gd^{3+} doping amounts were decreased on increasing the $4f^{@e}$ of lanthanide metals in B@LSNR. These were also estimated in the interpretation of PCPs as $4f^{7e}$ of Gd^{3+} had caused a repulsion with the respective chosen lanthanide metals. The intensities of Gd are increased from Nd_2S_3 to Er_2S_3 while decreased for Yb_2S_3 due to $4f^{13e}$ with milder electronic collisions. The intensities of Gd with B@LGTs are decreased due to the intimate communication of 2D GO sheets. The intensities and amounts of Nd_2S_3 to Eu_2S_3 are increased due to less than half-filled $4f^{@e}$, while from Er_2S_3 to Yb_2S_3, the intensities are decreased. The LSNRs in the range of 4.223–4.783 mg L^{-1} elemental compositions indicate their equivalent stoichiometric ratios. The elemental compositions of respective metals and Gd dopants in B@LSNRs are in the range of 3.066–4.150 and 1.162–1.763 mg L^{-1} respectively. While with B@LGTs, the elemental compositions of respective metals and Gd are in the range of 2.216–2.502 and 1.111–1.750 mg L^{-1} respectively (Table 6). The database obtained from ICP-OES analysis indicates that Gd^{3+}

Table 6 ICP-OES analysis of LSNRs, B@LSNRs, and B@LGTs

Analyte quantity	Elements	Corresponding intensity (g)	Prep. vol.: conc. (calib) (mg L^{-1})	Conc. (sample) (mg L^{-1})
Nd_2S_3 (406.109)	Nd	1334.4	4.513	4.513
Eu_2S_3 (381.967)	Eu	1 694 409.6	4.429	4.429
Er_2S_3 (337.27)	Er	74 385.78	4.223	4.223
Yb_2S_3 (328.937)	Yb	1543.1	4.783	4.783
Nd_2S_3@Gd (406.109)	Nd	3806	4.150	4.150
	Gd	9831.9	1.763	1.763
Eu_2S_3@Gd (381.967)	Eu	1 623 457.4	3.974	3.974
	Gd	21 394.0	1.341	1.341
Er_2S_3@Gd (337.27)	Er	17 697.5	3.822	3.822
	Gd	36 522.8	1.212	1.212
Yb_2S_3@Gd (328.937)	Yb	44 130.3	3.066	3.066
	Gd	1527.9	1.162	1.162
Nd_2S_3@Gd:GO (406.109)	Nd	101 043.6	2.326	2.326
	Gd	212 602	1.639	1.639
Eu_2S_3@Gd:GO (381.967)	Eu	644 080.9	2.502	2.502
	Gd	10 172	1.750	1.750
Er_2S_3@Gd:GO (337.27)	Er	73 521.4	2.451	2.451
	Gd	8703.4	1.439	1.439
Yb_2S_3@Gd:GO (328.937)	Yb	2027.4	2.216	2.216
	Gd	290.3	1.111	1.111

and GO were adequately doped and coated with LSNRs. While their nuclear sizes, the number of 4f$^{@e}$, and FGs of exfoliated GO sheet have proven the B@LGTs as the robust photocatalysts.

The B@LGTs have enhanced the PCR of BBR, TMIs, and QHIn compared to GO, LSNRs, and B@LSNRs. The elemental compositions confirmed the substantial chemical binding of dopants and coating agents with the angular momentum of LSNRs. The detail of the ICP-OES analysis is given in Table S29.†

3.14. Thermal stability *via* TGA, DTA, and DTG

TGA indicated the structural stability and heat holding ability of samples in terms of wt loss. Thus, B@LGTs have gained uniform thermal energy and Gt of the C–C skeleton also lost wt in the 1st order due to strong VWFs (Fig. 15a). The stronger heat holding capacities with the Gt → GO → LGT→ and LSNR → B@LSNR → B@LGT indicate the structural stability.[30] The Gt with no wt loss for moisture accounts for the stronger VWFs than GO with 15.24% wt loss at 106 °C. The LSNRs and Gt due to compact structures with stronger VWFs could not hold much water, while GO with manifold FGs and FEs having several energy ensembles almost in the same phase showed sharper 88.76% wt loss at 194 °C. Thus, the structural activities of GO could be expressed as $\text{VWF} = \int_m^n \psi_n \times \psi_m d\tau = 1$ shifting to $\int_m^n \psi_n \times \psi_m d\tau \neq 1$ from Gt to GO respectively with $\psi_m \neq \psi_n$, as their initial m and final n coefficients differ at two temperatures due to alignment (Fig. 15a and b). The LGTs were split at ~250 °C with hedgy oscillations, while Nd_2S_3, Er_2S_3 and Yb_2S_3 have quenched the oscillations by synchronization and Eu_2S_3 was stabilized. Eu_2S_3 with hedgy oscillations is shifted to an empty 4f suborbital than other LSNRs. The resonating B@LSNRs get detached[103] from the lattice, as Gd^{3+} from 0 to

250 °C accelerated the $\psi_{LSNR} \approx \psi_{S^{2-}} \oiint \psi_{LSNR}$ and $\psi_{Gd^{3+}} \approx \psi_{S^{2-}}$ and $\psi_{Gd^{3+}} \approx \psi_{Ln^{3+}}$ to shorten the PCR time. The spins of the 4f$^{@e}$ could boost the efficiencies of sensors, acoustivity,[61] TFT, and contrasting activities[16] in the CT scan.[32] Nd_2S_3@Gd has lost 28.03% wt at 287.49 °C on oscillation as $\psi_{2Ln^{3+}} \approx \psi_{3S^{2-}} \oiint \psi_{LSNR}$ to $\psi_{Gd^{3+}} \approx \psi_{S^{2-}}$ (Fig. S4†). B@LSNR with specific frequencies could exchange a coded message[104] similar to receiving the $h\nu$ transforming into the holes compared with the standard known quantum materials. Gd^{3+} equipartitioned Nd_2S_3 at 750 °C, while DTA for Eu_2S_3 indicated uniform charge distribution compared to other LSNRs. The B@LSNR lost wt at 254 and 436 °C along endothermic and exothermic peaks at 750 °C. The Gd$^{3+} \cdots$S^{2-} and Ln^{3+}–S$^{2-} \cdots$Gd^{3+} strings could have aligned Eu_2S_3 with Gd^{3+}. The Gd^{3+} 4f^{7e} could not induce major oscillations with Eu_2S_3 except mass transitions at 254.82, 436.6, and 800 °C with 37.04, 27.54, and 35.42% wt losses respectively (Fig. S3 and S4†). Gd^{3+} with 2Eu^{3+} and 3S^{2-} of Eu_2S_3 enhanced the holes *via* $\psi_{Ln^{3+}} \approx \psi_{S^{2-}} \oiiint \psi_{Gd^{3+}} \approx \psi_{S^{2-}}$) with tetrahedron tentropic cavities (eqn (3.2)). B@LGT supersedes the Schottky and Frankel defects to regulate a current flow[105] *via* $\psi_{Ln^{3+}}$ and $\psi_{Gd^{3+}}$ in a photocatalysing medium to calculate the energies as follows:

$$E_E = \frac{\left| \psi_{Gd^{3+}} \times \psi_{Ln^{3+}} \right| \times \left| \psi_{S^{2-}-Gd^{3+}} \times \psi_{S^{2-}-Ln^{3+}} \right|}{4\pi\varepsilon r^2} \quad (3.2)$$

$\psi_{S^{2-}-Gd^{3+}}$ mutually attracts while $\psi_{Gd^{3+}} \times \psi_{Ln^{3+}}$ repels with exothermic and endothermic energy cycles respectively to store energy. B@LGT with $\psi_{S^{2-}-Gd^{3+}}$ contraction and $\psi_{Gd^{3+}} \times \psi_{Ln^{3+}}$ expansion cycles are aimed to advance piezoelectric sensors, bionics, and, spintronics with $\frac{1}{2}$ filled 4f$^{@e}$.[98] Er_2S_3@Gd^{3+} at 220 °C and 310 °C has been reoriented with a sharper mass transition than Eu_2S_3@Gd^{3+}. Yb_2S_3@Gd^{3+} with hedgy oscillations credited to equidistribution with a similar value of electron defined probability $|\psi_{Yb_2S_3@Gd^{3+}}|^2$ as Yb^{3+} has 4f^{13e} (Fig. S3 and
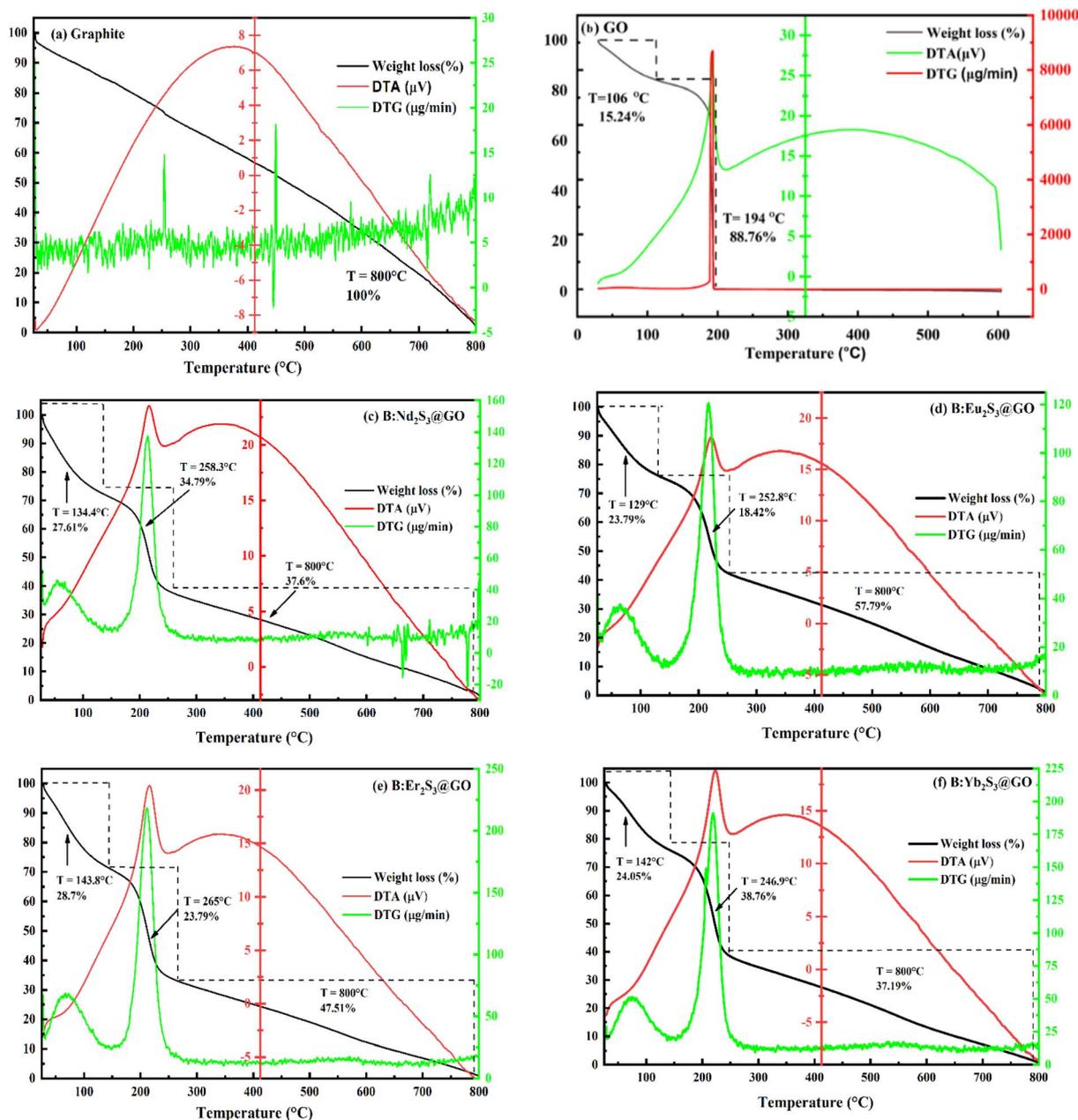
Fig. 15 TGA, DTA and DTG of (a) Gt, (b) GO and (c–f) B@LGTs.

S4†). The B@LGTs with $\psi_{Ln^{3+}-S}$ and $\psi_{Gd^{3+}-S}$ have induced 1st mass transition at 50 °C than at 210 °C with LGT[98] (Fig. 15c–f and S3†). B:Er$_2$S$_3$@GO has lost 23.7% at 129 °C compared to 28% wt loss from Eu$_2$S$_3$@Gd^{3+} at 143.8 °C, indicating higher stability for B:Er$_2$S$_3$@GO. The wt loss with B:Yb$_2$S$_3$@GO is 38.76% at 246.9 °C than 34.79, 18.42, and 23.79% at 258.3, 252.8, and 265 °C for B:Nd$_2$S$_3$@GO, B:Eu$_2$S$_3$@GO, and B:Er$_2$S$_3$@GO respectively, indicating the higher stability of B:Yb$_2$S$_3$@GO. The Peaks with B:Eu$_2$S$_3$@GO are sharpened at 210 °C upon aligning with Gd^{3+} (Table S13†). $\psi_{Yb^{3+}}$ and $\psi_{Gd^{3+}}$ of B:Yb$_2$S$_3$@GO might have induced a drift velocity of holes/charges *via* tentropic cavities (Fig. 15c–f). The DTG peaks with

Gt are resonating with the same frequencies except with 15 μg min^{-1}, 17 μg min^{-1}, and −2.5 g min^{-1} at 250 °C, 450 °C and 730 °C respectively due to intimate sheet alignment with the stronger VWFs. Each sheet with a stronger FRET could not localize heat, while with GO a single DTG signal appeared as all the FGs and FEs of GO had equally oscillated with the same heat contents (Fig. 15b). It has predicted an equal FG distribution throughout a GO sheet without energy gradient and was chosen for coating. The DTG for B:Nd$_2$S$_3$@GO, Eu$_2$S$_3$@Gd^{3+}, B:Er$_2$S$_3$@GO, and B:Yb$_2$S$_3$@GO with sharper structural changes at 258.3 °C, 252.8 °C, 265.0 °C, and 246.79 °C with 34.79, 18.42,
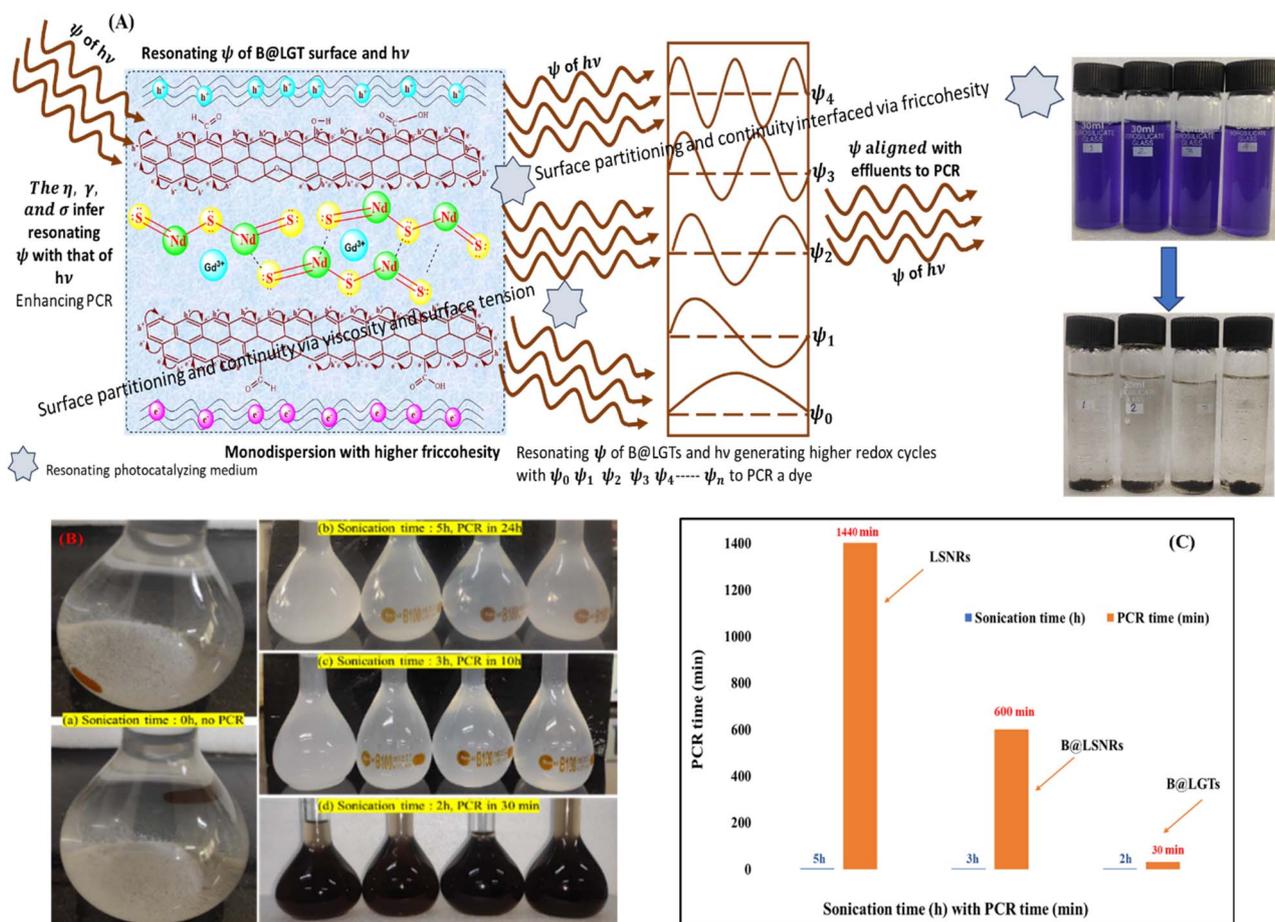
Fig. 16 (A) Wavefunctions of the surface in the same phase to receive maximum $h\nu$ emitting phonons of robust ψ to photocatalytically reduce (B) Aq-LSNR, B@LSNR, and B@LGT. (C) PCR *vs.* sonication time.

23.79%, and 38.79% wt loss have predicted a common lattice equally integrated with GO sheets (Fig. 15c–f).

4. PCPs interfacing photocatalysis at different T/K values

The monodisperse B@LGT surfaces oscillating with ψ in the same phase as of $h\nu$ from visible light have allowed negligible rebouncing. Therefore, the PCPs have predicted stabilized surfaces generating resonating wavefunctions in the same phase as of $h\nu$. Thus, the interstitial surfaces have been proven asset to resonating the wavefunctions of photocatalyzing surfaces with that of the light sources. Fig. 16A illustrates the overall intimate density of energy states to manifold the emitted ψ accessing a cathodic dye. The viscosity with adequate adherence has predicted a surface partitioning with intimate continuity without causing the energy gradients that hurdle $h\nu$ receptance. Basically, a medium of highest friccohesity economically allows each B@LGT molecule to participate for the PCR of a dye. Therefore, the concentrations of B@LGT were cautiously chosen to avoid nanoclustering that could have damaged an operative string depicted in Fig. 16. B@LGTs with the lowest sonication time have developed an intense

photoluminescence on generating the resonating wavefunction w.r.t. visible light, which have photocatalytically reduced a dye in 30 min. The monolayer solvent adherence with a higher viscosity and the strongest surface continuity with adequate surface tension have been the asset to receive the $h\nu$.

For initiating interactions with the dipoles of water, 0.01 g% LSNR, B@LSNR, and B@LGT were sonicated at 28 kHz for 5, 3, and 2 h. The dipoles get aligned at the electrostatic sites of LSNRs for developing monolayer adherence with adequate coherence *via* an anticoagulating friccohesity mechanism (Fig. 16a). The order of B@LGT > B@LSNR > LSNR inferred monodispersion stability for 2 h, 3 h, and 10 months respectively. The order and time of stability have predicted the sharing of PE of LSNRs with dopants *via* repulsion with Ln^{3+} but attraction with S^{2-}. Such infinite charge matrices could have been generated in a most symmetric pattern aligning the charges in electrostatic dipoles to flow the electron in response to the $h\nu$. Therefore, the coating with a 2D GO sheet with uniform distribution of FGs and FEs made the surfaces receptive for $h\nu$. At the same time, GO has equipartitioned the surface energies. Therefore, water monomers have entered the interstitial tiers of B@LGTs on adhering around the charged sites regaining the PE of same strengths. Such arrangement of

charges has also attracted the dipoles of H_2O to enhance the surface continuity in the flow of e^- and h^+ holes. The water monomers gained on disrupting the hydrogen bonded (HB) water have been depicted with the viscosity, surface tension, friccohesity and thermodynamic parameters like activation energy (E_a) (Fig. 21). The monodispersion and E_a have predicted the intimate adherence of B@LGT photocatalysts with BBR, TMIs, and QHIn for PCR (Fig. 16). Thermograms of the B@LGTs after the PCR of a dye developed a hedgy DTG pattern due to the adsorption of reduced dye with an intimate interfacial layer that exchanges energies through the FRET. Shifts in HR-TEM and FT-IR stretching of B@LGTs with reduced BBR predicted their adsorptions (Fig. 30 and 31). This is also proven with the BET analysis of B@LGTs that have adsorbed inert N_2 gas upon increasing the relative pressure. The adhered water dipoles with B@LGTs are replaced with the reduced dye to separate. The unreduced dye and water interactions are stronger, while the reduced dye did not interact with the water dipoles. There is a novel interfacial science work with the reduced dyes, as these did not coagulate and did not get settle. Under this condition, a reduced dye opts to enter the interstitial cavities of the B@LGTs where water has stronger affinity to interact with the water molecules. Therefore, η, γ, σ, and thermodynamic properties explained the adherence of adequate H_2O molecules without mixing the effluents. It had replaced the adhered H_2O molecule with the reduced effluents having the affinities to be adhered with the interstities of B@LGTs, while their adhered water due to stronger dipolar interaction go together as the water phase pushes out the reduced effluents to the interstities. The reduced dye increased the density of B@LGTs and got settled. The PCPs such as η, γ, and σ affect this replacement (Fig. 16). The aq-B@LGT with dynamic property η elucidated the normalization of surfaces to cohere H_2O dipoles with moderate adherence (Fig. 16f). The B@LGTs with monolayer water adherence to each site of interstities aligned similarly with slightly higher γ values. The interstitial strings LSNR–NHS–NHS–LSNR and B@LGT–NHS–NHS–B@LGT developed stronger interfacial continuity (Fig. 16f). The PCPs for 0.01 g% at 288.15, 298.15, and 310.15 K were measured, while at 283.15 and 313.15 K, they are calculated from the regression constants obtained from the above-mentioned temperature range (Tables 8–13). The monolayer water adhesion to aq-B@LGTs balanced by frictional and cohesive forces noted as friccohesity predicted energy equipartitioning.[33] B@LGTs photocatalytically reduced BBR, TMIs, and QHIn in 15–40 min as NHS aligned around the charged sites that acted as molecular switches and linkers for reorienting to receive the $h\nu$ to generate the holes. The E_g values of aq-B@LGT from 298.15 to 310.15 K decrease attaining a suitable reorienting state with uniform H_2O adherence with a distinguished PL. Nd_2S_3 with $4f^{3e}$ mildly realigned the H_2O dipoles compared to Eu_2S_3, Er_2S_3, and Yb_2S_3 while B@LGTs sharpened PL to harness solar energy (Fig. 16B).

4.1. Recycling of wastewater effluents and recovery

A new pedagogy of B@LGTs as a novel research methodology for recycling wastewater effluents has been highly economic
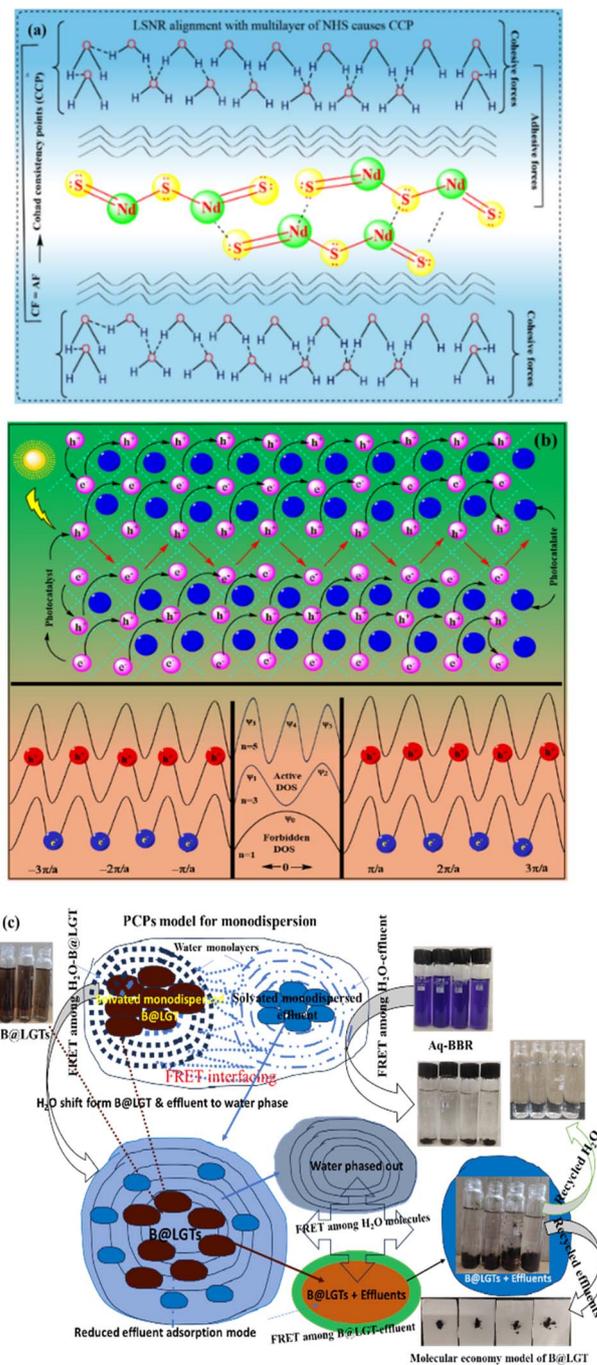

Fig. 17 (a and b) CCPs for LSNRs with NHS monodispersing photocatalysts for symmetric Brillion zones avoiding $h\nu$ annihilation. (c) PCPs elucidating monodispersion with an intimate FRET for recycling effluents and clean water through photocatalysis.

for getting rid of nuisance of polluting effluents. Initially, their PCPs have predicted an entry of H_2O dipolar molecules at NTP, generating certain internal pressure due to interactions with BBR on PCR. Thus, the PCPs have been substitution of BET to analyse structural stability and adsorption abilities at variable T/K. Since, the H_2O dipoles adhered to each interstities have softened the functional surface area. As before PCR, no

solvated effluents could have entered the adhered H_2O. While with time, the reduced effluents have been aside by the cohesive force of H_2O moving in two ways notably the post-PCR dynamics for a recovery of the reduced effluents. The mutual communication of B@LGTs and effluents *via* FRET predicts spontaneity and sustainable PCR mechanism. Fig. 17c depicts the wastewater recycling potential of interstitial B@LGT initiated by monodispersing BBR in a common solvent, which elucidated the gradients in interacting activities of unreduced and reduced effluents represented with PCPs as a key prerequisite database for extensive recycling studies. The energy gradients signify the higher friccohesity values on unreduced effluents which with time decrease on phasing out a water from B@LGT and effluents both, it forms a pure water phase with lower friccohesity values. At the end, the effluents have replaced the water dipoles, which upon gaining density get settled with shorter size.

Thus, their monodispersion has occupied a higher surface area with higher adhesion by remaining suspended in a thermodynamically stable solution with their stronger FRET. The $h\nu$ has reduced the effluents that had acted as the cathode by causing a gradient in energy, separating them (Fig. 17).

4.2. Viscosity (η, mPa s) for molecular alignments

Rovitronic motions with specific rheological resistance with adequate relaxation time to mimic ψ_{sv} to photocatalytically reduce BBR, TMIs, and QHIn. The twisting or deforming of solvated B@LGTs during PCR disrupts the interfacial continuity that hampers receiving of $h\nu$. Therefore, monolayer adhesion with moderate cohesion has predicted continuity and is measured with friccohesity. η is a prerequisite of friccohesity interfacing a photocatalyst to capture $h\nu$, which is calculated as follows:[33]

$$\eta = \left(\frac{t}{t^\circ}\right)\left(\frac{\rho}{\rho^\circ}\right)\eta_0, \quad \eta_r = \left(\frac{\eta}{\eta_0}\right)_T \text{ and } \eta_r = 1 + 2.5\phi \quad (3.3)$$

where ρ is the density of the solution, ρ° the density of water, η° the viscosity of water, η_r the relative viscosity, and vft the relaxation time (τ). The shear rate with certain heat capacity has stabilized the charge centres tuned by T/K (Tables 8 and 9). The consistent shear stress and rate are both inversely proportional to the uniform lattice of wavevector 'k' ($-\pi/a$, 0, π/a), and are analysed by DTG and fitted with the Schrödinger equation transforming PE to KE as follows:[33]

$$\frac{\partial^2\psi}{\partial x^2} + \frac{8\pi^2 m}{h^2}(E-V)\psi = 0, \ (V=0),$$

$$\frac{\partial^2\psi}{\partial x^2} + \frac{8\pi^2 m}{h^2}E_\psi = 0, \ E_\psi = -\frac{h^2}{8\pi^2 m}\frac{\partial^2\psi}{\partial x^2} \quad (3.4)$$

$V(x, t) = 0$ energy at position x at time 't' aligns the B@LGTs to receive the $h\nu$ with higher η and lower surface tension[106] (Fig. 18). The $4f^{@e}$ have behaved like an upper critical (UC) solution to increase the PCR rate shortening the PCR at 298.15 K. The $4f^{@e}$ spins of B@LGTs have enhanced the consistent interacting activities[107] noted as cohad consistency points (CCPs) aligning the adhesive and cohesive energies as follows:
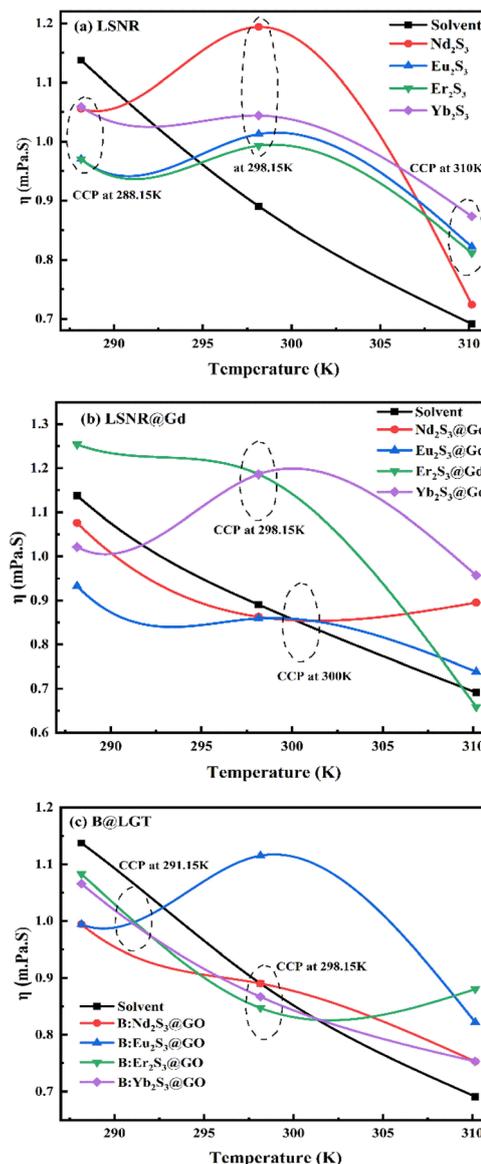

Fig. 18 Viscosities for (a) aq-LSNR, (b) aq-B@LSNR and (c) aq-B@LGT plotted *vs.* temperatures with higher resolution for B@LSNRs, while the values of B@LGTs are in a narrow range.

$$\text{Cohad consistency points(CCPs)} = \frac{\text{Cohesive forces}}{\text{Adhesive forces}} = \text{constant} \quad (3.5)$$

NHS–NHS, NHS–LSNR, and NHS–LSNR–NHS with B@LGTs have been aligned by the cohesive, adhesive, and cohad forces respectively (Fig. 17 and 18). The η values for aq-Nd_2S_3 and Yb_2S_3 have coincided at CCPs with equilibrated cohad forces at 288.15 K. The dopant has shifted the CCPs values to 298.15 and 300 K while a coating agent GO to the 291.15 and 298.15 K, respectively (Fig. 18a and b). The B@LGTs of Nd_2S_3 and Eu_2S_3 with partially while the Er_2S_3 and Yb_2S_3 fully filled 4f orbitals have coincided with CCPs respectively (Fig. 18c). Gd^{3+} and Ln^{3+} both have attracted the $O^{\delta-}$ of H_2O interfacing the S^{2-} with adhesion =

cohesion of solvent competitively. The CCPs, the novel interfacing with PCPs in the lanthanide chemistry, have advanced the PCR.[108] The NHS with dopant and matrices have generated the CCPs around the B@LGTs.[61] The B@LGTs of Nd_2S_3, Eu_2S_3, Er_2S_3, and Yb_2S_3 at 291.15 and 298.15 K respectively have produced the CCPs while the LGTs of La_2S_3, Ce_2S_3, Tb_2S_3, and Ho_2S_3 at 283.15, 298.15, and 315.15 K, as reported previously [33] (Fig. 18c). The origin of the CCPs infers energy with ψ_{sv} of a longer wavelength. The CCPs for a series agree at comparable T/K on a common alignment. LSNR and B@LGTs both might have generated the vibrational (E_v) and rotational (E_{rot}) energies as $E_v = E_{rot}$ *via* NHS at 315.15 T/K (Fig. S9†). The H_2O alone on monolayer adhesion has fastened the fluid flow with η as $Nd_2S_3 > Yb_2S_3 > Eu_2S_3 > Er_2S_3 > H_2O$ at 298.15 than $Yb_2S_3 > Eu_2S_3 > Er_2S_3 > Nd_2S_3 > H_2O$ at 310 K. The η values at 300 K infer constant cohad forces with similar CCPs due to the LSNR–NHS linkages (Fig. S12†). The NHS around S^{2-} and Ln^{3+} have synchronized the spins for the similar activities predicted from the CCPs (Fig. 17). The η values for H_2O differ from that of the aq-LSNR as the NHS remained the same with CCPs at 315.15 K (Fig. S12†). The NHS adhesion to Eu_2S_3, Er_2S_3, and Yb_2S_3 has interfaced with that of the Gd^{3+} by avoiding their deposition including of cholesterol.[109] The competitive alignment of electronegative O^{2-} of H_2O with either the Ln^{3+} or the Gd^{3+} has truly created an energy distributing ingredients. As Ln^{3+} is bonded with S^{2-} through the primary bond, Gd^{3+} is bonded through the secondary bond. These have been functional interstities to align the 2D GO sheet for generating a higher surface area and the frictional forces depicted with the η. That were obtained on aligning the water dipoles for PCR with robust FRET. Because the said charge intricacies are ultrasensitive to thermal energy and hence PCPs were studied at 283.15, 288.15, 298.15, 310.15 K and 313.15 K. The B@LGTs could be an alternate quantum material for the CT scan for body X-rays[22] with more contrast[110] than Gd^{3+} alone generating ψ_{sv} of longer λ. The η value of B@LSNRs as $B@Er_2S_3 > B@Yb_2S_3 > H_2O > B@Nd_2S_3 > B@Eu_2S_3$ has predicted the effective adherence of water around B@LSNRs than others with least E_a for the PCR. The higher η values for Er_2S_3 and Yb_2S_3 than Nd_2S_3 and Eu_2S_3 have inferred the monolayer adhesion of water dipoles. The Nd_2S_3 and Eu_2S_3 with the CCPs at 300 K than Er_2S_3 and Yb_2S_3 at 298.15 K with higher η values have normalized the spins unlike Nd_2S_3 and Eu_2S_3 with less $\frac{1}{2}$ filled 4f electrons (Fig. 18b). Nd_2S_3 with stronger adhesion at 288.15 K has responded with robust FRET than composition (Fig. 18 and S12a†). Nd_2S_3, Eu_2S_3, Er_2S_3, and Yb_2S_3 have reoriented the solvated state with a common shear but are narrowed down to 315.15 K (Fig. S12a†). Gd^{3+} has streamlined a shear stress with extra CCP at 300 K, while a common CCP for Er_2S_3, and Yb_2S_3 at 298.15 K has higher η values. The dopant has partially equilibrated $\psi_{S^{2-}}$ and $\psi_{Ln^{3+}}$ of B@LGT on aligning the NHS dipoles with different CCPs at 291.15 and 298.15 K.

4.3. Surface tension (γ, mN m^{-1})

Since, the $Ln^{3+}\cdots H_2O$ and $Gd^{3+}\cdots H_2O$ interactions have equipartitioned their energies where the Ln^{3+} is covalently bonded with S^{2-} while the Gd^{3+} with the secondary. These charge wavevectors along GO have developed the electrostatic dipolar
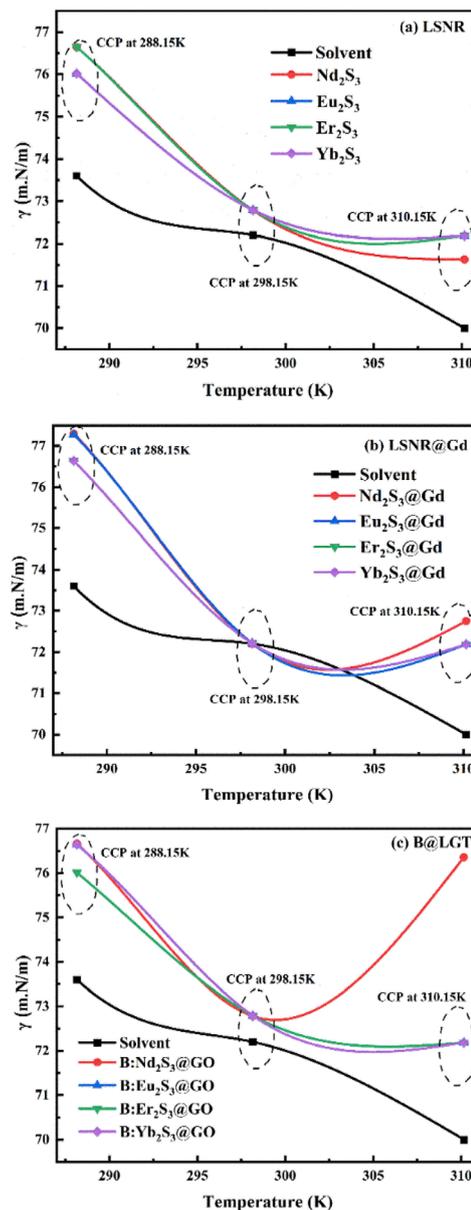

Fig. 19 Surface tension of (a) aq-LSNR, (b) aq-B@LSNR and (c) aq-B@LGT plotted against temperatures with a higher resolution.

alignments of H_2O at the air-aq-B@LGTs interfaces. This directly influenced the receptance of $h\nu$ from solar energy. The surface energy noted as surface tension (γ) directly affects the $h\nu$ interactions. Lower γ values with small sized pendent drop number (pdn) were formed on NHS adherence. The pdn were used to calculate γ values with eqn (3.6), the lower γ values have enhanced a PCR.[61]

$$\gamma = \left(\frac{n^\circ}{n}\right)\left(\frac{\rho}{\rho^\circ}\right)\gamma^\circ \qquad (3.6)$$

where γ°, n°, ρ° and γ, n, ρ are the surface tension, pdn, and density of water and solution respectively. The $\gamma \sim 78$ mN m^{-1} for LSNR and B@LSNR infer realigned H_2O with Ln^{3+} and with S^{2-} with stronger cohesive forces at 288.15 and 298.15 K

(Fig. 19). The B@LSNRs have decreased multilayer adhesion upon shortening the PCR time (Fig. 18a and Tables 10, 11). aq-LSNR with 65–77.28 and B@LSNR with 51.98–76.64 mN m^{-1} photocatalytically reduced BBR, TMIs, and QHIn in a longer time than that of B@LGTs (Fig. 19b). The B@LGTs have weakened the dipolar attraction than LSNR and B@LSNR by partitioning the NHS. The higher γ values at 288.15 than at 298.15 K infer the manifold NHS with a lower surface energy, while after 310 K, a decrease in the γ value on monolayer water adherence is observed (Fig. S13†). The NHS and Gd^{3+} have aligned $\psi_{S^{2-}}$ and $\psi_{Ln^{3+}}$ decreasing γ from 78 to 77.6 mN m^{-1} at 298.15 K (Fig. 19). The $\gamma_{Gd^{3+}} = \gamma_{LSNR} - \gamma_{B@LSNR}$ infers a reorientation of $\psi_{S^{2-}}$ and $\psi_{Ln^{3+}}$ with a slightly higher relaxation time on equipartitioning the NHS. The $\eta_{Gd}^{3+} = \eta_{B@LSNR} - \eta_{LSNR}$ is linearly decreased (Fig. 11 and 18) upon lowering γ shifting from LSNR to B@LGTs by reducing BBR in a shorter time, in agreement with Fermi energy (eqn (3.7)):

$$E = E_F + k_B T \left(\frac{1}{4f^{@e}} - 1 \right) \qquad (3.7)$$

Gd^{3+} with E–E_F synchronized both γ and η as B@LSNRs have slightly scattered the γ values at higher T/K than at 298.15 K due to the competitive Gd^{3+}–NHS and Ln^{3+}–NHS interactions without $\psi_{Gd^{3+}} = \psi_{S^{2-}} = \psi_{Ln^{3+}}$ at 298.15 K. The $\psi_{Gd^{3+}}$ value has enhanced the surface energy for B@LSNR as $\gamma_{LSNR} > \gamma_{B@LSNR}$ at 298.15 K (Fig. 19a and b). The spins of Ln^{3+} are sensitive to T/K compared to composition while S^{2-} with shared orbitals is not so sensitive to oscillate.

The aq-B@LSNR with higher friccohesity than aq-LSNR have enhanced $\psi_{S^{2-}}$, $\psi_{Ln^{3+}}$ and $|\psi_{LSNR}|^2$ to $|\psi_{Gd-LSNR}|^2$ on attraction and repulsion respectively enhancing the PCR rate. The B@LGTs have synchronized the deficient sites of BBR, TMIs, and QHIn with higher UV-vis absorption[111] (Fig. 12 and 26). The B@LGTs with $E_g = 1.88$ eV with intense wave and charge sensors may tune the confirmatory state of protein or intercalation of DNA.[112] Higher γ values for LSNR and B@LGT are coincided at 298.15 and 310 K than lower with B@LSNR at 298.15 K equipartitioning an energy (eqn (3.8)):

$$E = E_{e^-} + E_{Nu^+} + E_{EER} + E_{e^-Nu} + E_{Nu-Nu} \qquad (3.8)$$

E is the vital line oscillation on increasing T/K via moderate shear and uniform surface energy to track $h\nu$. The B@LGTs have quantized the laminar flow and surface energies expressed as friccohesity (Fig. 20).

4.4. Friccohesity (σ, S cm^{-1})

The friccohesity basically aligns the photocatalysts avoiding deformation and wrinkling of surfaces, which cause surface twisting that inhibit the receiving of $h\nu$. The solvent has monodispersed the B@LGTs developing the thin hydration spheres attained via interstices. Thereby, the adequate adherence of H$_2$O dipoles from monolayer to multilayer generates a protective mechanism noted as cohesive force with sufficient PE to avoid twisting or coagulating, coalescence, of B@LGTs, where $h\nu$ is received by generating the favourable rovitronic activities.
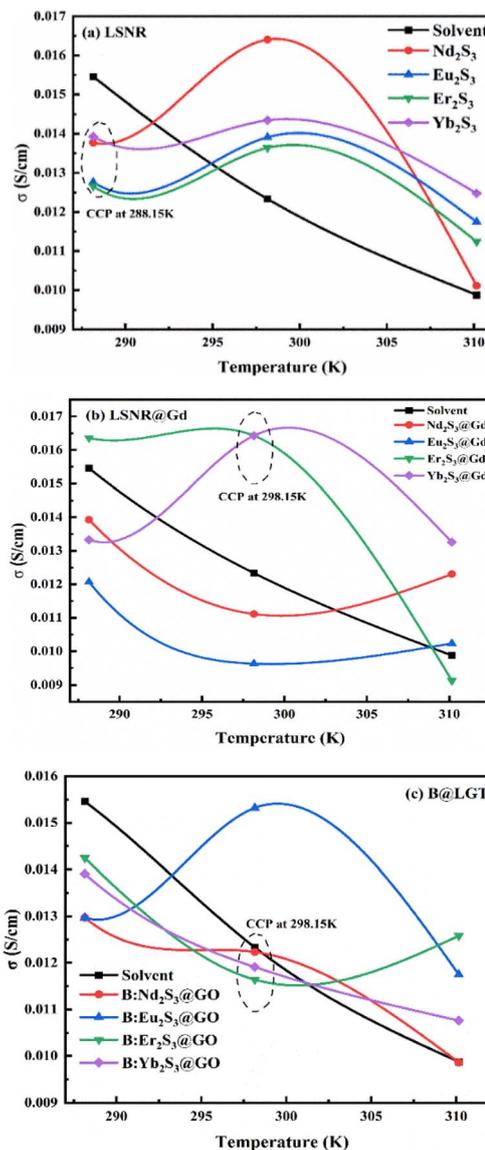

Fig. 20 Friccohesity of (a) aq-LSNR, (b) aq-B@LSNR and (c) aq-B@LGT plotted against temperatures with higher resolution for LSNR and B@LSNRs, while the values of B@LGTs are in a narrow range.

The monodispersion have been tracked with the vft and pdn values calculated with eqn (3.9):

$$\sigma = \sigma^\circ \left(\frac{t}{t_0} \pm \frac{B}{t} \right) \left(\frac{n}{n_0} \pm 0.0012(1-\rho) \right), \ \sigma = \sigma^\circ \left(\frac{t}{t_0} \right) \left(\frac{n}{n_0} \right),$$

$$\sigma = \frac{\sigma^\circ}{t_0 n_0}(t \times n), \ M_c = \frac{\sigma^\circ}{t_0 n_0} \qquad (3.9)$$

where σ and σ_0 are the friccohesity of solution and solvent, respectively, $\pm B/t$ is the kinetic correction and $0.0012(1-\rho)$ is the buoyancy correction, and other symbols are depicted as usual.[113] The corrections of 1×10^{-7} order are omitted and the Man Singh constant (M_c) depicts the shear stress and surface energy coefficient of aq-B@LGTs (eqn (3.7)). The σ values have predicted the surface forces (Tables 11 and 12) and laminar layer on getting the rovitronic motions of monolayered

adhesion of water around B@LGTs (Fig. 17). Because the energies and minimum entropies of B@LGTs on getting reoriented are highly interfacial and mutual tuned with electronic oscillation to receive $h\nu$. Therefore, the values of γ and η individually could elucidate the intimate intricacies of the ultrasensitive interfacial hairline marked with the friccohesity. The σ realigns the NHS dipoles in compliance with Gd^{3+} for PCR in a longer time. The γ values have distinguished the surface energies confined to more than two CCPs than the σ at variable T/K (Fig. 20). The CCPs have predicted a monolayered NHS–B@LGT validated with stretching and bending frequencies with the FT-IR spectra (Fig. 12). $\psi_{S^{2-}}$ and $\psi_{Ln^{3+}}$ with $|\psi_{LSNR}|^2 \neq 0$ seem to align the NHS dipoles with $\psi_{S^{2-}}$ separating the CCPs as T/K sensitive. The η values infer ψ_{LSNR}, $\psi_{B@LSNR}$, and $\psi_{B@LGT}$ interfacing the surface charges of the effluents[33] to intensify the CCPs with different γ and friccohesity values at 288.15 and 298.15 K with an integrating fluid dynamics[104] (Fig. 20). The friccohesity for aq-B@LGT photocatalytically reduced BBR, Cr^{3+}, Ni^{2+}, and Cu^{2+}, and QHIn in 30, 20, 40, 35, and 15 min respectively.

4.5. Thermodynamic parameters derived from PCPs for PCR

Thermodynamic parameters (E_a, ΔH, ΔG, and ΔS) derived from the viscosity database predicted the spontaneity of a photocatalysing medium.[61] The ΔH value ranging from -0.6 to -6.7 kJ mol^{-1} with $\Delta G < 0$ on decreasing linearly on raising T/K indicates monodispersion fastening the PCR of BBR, Cr^{3+}, Ni^{2+}, and Cu^{2+}, and QHIn with B@LGT in 30, 20, 40, 35, and 15 min respectively. ΔH, ΔG, and ΔS with aq-B@LGTs at lower T/K predict a spontaneity for the PCR than at higher T/K (Fig. 21). The photocatalysing medium with $\Delta H < 0 < T\Delta S$ at lower T/K than higher shortened the PCR time, calculated as follows:[33]

$$\Delta G = \Delta H - T\Delta S, \ \Delta G \propto \frac{1}{\Delta S} \text{and} \ \Delta G \times \Delta S = k \quad (4.0)$$

The $\Delta G \ll 0 \gg \Delta S$ has lowered the PCR rate and plot of ΔG vs. ΔS is nonlinear due to unaligned functional sites at higher T/K. $Gd^{3+}@Eu_2S_3$ has shifted a common T/K point to 310 than 308 K with Eu_2S_3 as the E_a of dopant and LSNR matrices get aligned at the cost of restricted collisions (Fig. S7 and S8†). The common T/K point is supplemented with ΔS and B@LSNRs have lowered a common point to 298.15 K on equal energy distribution. The $Gd^{3+}@Er_2S_3$ and $Gd^{3+}@Nd_2S_3$ have been aligned with nearly half and fully filled 4f orbitals with $\Delta G \geq \Delta S$ in the same ratio[25] at lower T/K (Fig. 21). The $Gd^{3+}@Yb_2S_3$ and $Gd^{3+}@Eu_2S_3$ with similar ΔG, ΔS, and ΔH trends are credited to the number of electrons in the 4f orbital. The ΔG, ΔH, and least ΔS with B@LGTs have photocatalytically reduced BBR, TMIs, and QHIn in 15–40 min, and E_a was calculated with $\log(\eta)$ vs. $(1/T)$ with eqn (4.1):[33]

$$\log(\eta) = \log A - \frac{E_a}{R} \times \left(\frac{1}{T}\right) \text{or slope} = -\frac{E_a}{2.303 \times R}, \ E_a$$
$$= -\text{slope} \times 2.303 \times R \quad (4.1)$$

The ΔH, ΔS, and ΔG values were calculated using E_a as follows:[33]

$$\Delta H = E_a - 2.303RT, \ \Delta G = 2.303 \times R \times T \times \log(\eta) \ \Delta S$$
$$= \frac{(\Delta H - \Delta G)}{T}, \ \Delta G = \Delta H + T\Delta S \quad (4.2)$$

B@LGT with $\Delta H < 0$ and E_a from -670.14 to -925.57 J mol^{-1} with B:Nd_2S_3@GO to B:Yb_2S_3@GO indicates a spontaneous photochemical reaction (Fig. 21 and Tables S22–25†). The $\Delta S < 0 < \Delta S$ up to 312 K is noted as the effluent saturation point[33] on being weakly adsorbed by B@LGT by releasing the ΔH. The B@LGTs with least ΔS with $\Delta G < 0 > \Delta H$ have PCR a BBR in 30 min (Fig. 21). The $\Delta G < 0$ values were obtained on receiving the $h\nu$ that had enhanced the $\pi \to \pi^*$ favouring the PCR.

4.5.1. E_a from fluid dynamics ($E_{a,\eta}$) and UV/vis ($E_{a,UV}$). The higher negative E_a values for undoped LSNR than the B@LSNR are decreased on enhancing the interacting activities as KE $\gg$ PE (Tables S14–S21†). The B@LSNR with strongly aligned water dipoles closely interfaces to photocatalytically reduce the effluents in a shorter time than LSNR. Thus, no charges were originated out of the $Ln^{3+}\cdots H_2O$ and $Gd^{3+}\cdots H_2O$ matrices due to energy equipartitioning that were missing with the LSNRs.

$Ln^{3+}\cdots H_2O$ and $Gd^{3+}\cdots H_2O$ are missing with LSNRs. The lower E_a values with aq-B@LGTs than B@LSNR and LSNR determined from their respective UV/vis abs and fluid dynamics have enhanced the PCR activities. $E_{a,UV}$ in the range of -3.95 to -30.12 J mol^{-1} for Nd_2S_3@GO, Eu_2S_3@GO, Er_2S_3@GO, and Yb_2S_3@GO than $E_{a,\eta}$ from -210.62 to -700.25 J mol^{-1} for Nd_2S_3, Ee_2S_3, Er_2S_3, and Yb_2S_3 consumed more energy in thermodynamic reorientations than UV transition (Tables S7–S10 and S14–S17†). $E_{a,\eta}$ for B@Nd_2S_3, B@Eu_2S_3, B@Er_2S_3, and B@Yb_2S_3 decreased from -361.47 to -765.88 J mole^{-1} upon entering water dipoles to their interstities causing the reorientational motions with continuity in capillary flow (Tables S18–S21†). The $h\nu$ of UV light excited electrons from VB to CB of unreduced BBR by overcoming a fermi energy resistance to interact with BBR. The B@LGTs with monolayer NHS in the excited state expeditiously got reoriented for transferring the holes to BBR by avoiding a mismatch in spatial occupancies. $E_{a,\eta}$ acquired from a system is more negative while an increasing T/K has compensated $E_{a,\eta}$ at a constant concentration by avoiding the interactions with self for receiving the maximum $h\nu$. $E_{a,UV}$ of aq-B@LGTs and BBR with time was compensated with $E_{a,\eta}$ on increasing T/K. The T/K increments have controlled the rovitronic motions in fluid dynamics for optimizing the state. The molecular reorientations have gained much energy, while UV absorption has overcome the resulting motions, $E_{a,\eta} > E_{a,UV}$. The $E_{a,UV}$ and $E_{a,\eta}$ interfacing has predicted the monodisperse photocatalysts for receiving more $h\nu$ for PCR buffered with water dipoles (Tables S7–S25†). The B@LGTs acquire less $E_{a,UV}$ and $E_{a,\eta}$ with least E_g to PCR the effluents in a shorter time than others, which is given as follows (Fig. 21e):

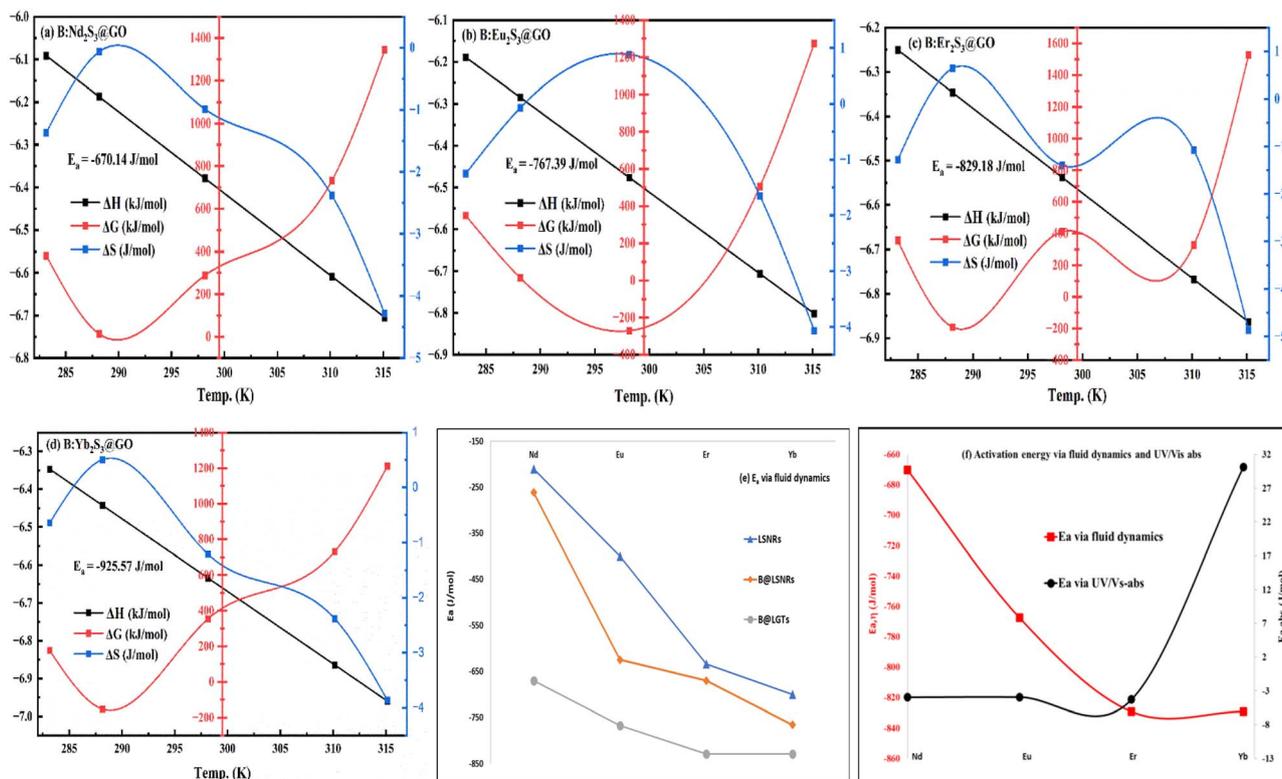$$\text{PCR} = K_{PCP}\left[\frac{1}{E_g} \times \frac{1}{E_a}\right] \quad (4.3)$$

Fig. 21 (a–d) For B@LGTs, dH linearly decreased while dG and dS oppositely vary upon release of heat content on increasing temperature with reorientations and (e) E_a for photocatalysis. (f) E_a calculated from fluid dynamics and UV/vis-abs.

K_{PCP} predicts the spontaneity of B@LGTs that photocatalytically reduced BBR in 30 min in 1st order with the residual coefficient (R^2) from 0.87 to 0.98. The B@LGTs could not adsorb an unreduced dye on stronger water adhesion while a reduced dye has replaced H_2O to get adsorbed onto B@LGTs.

$$B@LGTs + h\nu \rightarrow B@LGTs* \rightarrow B@LGTs + holes \rightarrow$$
$$holes + BBR \rightarrow reduced\ BBR \quad (4.4)$$
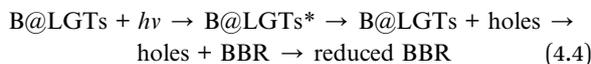
Low $E_{a,UV}$ and $E_{a,\eta}$ allowed aq-B@LGTs to adsorb reduced BBR as B@LGTs-BBR acquire energy to come out of NHS sheath. The B@LGT molecules on getting reoriented have aligned a BBR for PCR while the reduced BBR was adsorbed by B@LGTs predicted with PCPs.

$$h\nu + B@LGTs = holes = BBR \cong B@LGTs - BBR$$
$$+ \Delta H = -ve \quad (4.5)$$
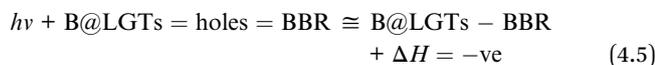
Hence, the exchange of adhered H_2O to B@LGTs before the PCR of effluents has different energetics than a condition when adhered H_2O is replaced with reduced effluents.

5. PCR for BBR, heavy metal ions, and QHIn on subsequent adsorption

To begin with, the B@LGTs photocatalytically reduced the pollutants by neutralizing their electronic-rich and -deficient sites to disconnect them from wastewater molecules. The B@LGTs

have received the $h\nu$ to generate the e^- and h^+ holes approaching their respective sites along the splitting of H_2O. The pollutants had developed stronger linkages with the H_2O dipoles through their respective $=N^+-$, SO_3^-, active methyl groups, delocalized π conjugation sites, and Cr^{3+}, Ni^{2+}, and Cu^{2+} did not allow adsorption (Fig. 22a and 28h). The QHIn with phenolic groups developed the linkages with stronger ionic interactions without adsorbing with B@LGTs. Thus, the B@LGTs could not adsorb them without PCR due to their stronger linkages with H_2O dipoles than the B@LGTs. The B@LGTs supplemented with the $h\nu$ had generated the e^- and h^+ holes to attack their linkages with the H_2O dipoles by reducing their electronic sites responsible for linkages. Thus, B@LGTs did not directly adsorb the pollutants, and no direct adsorption isotherm/equilibrium is possible as the PCR and adsorption had worked simultaneously. Thus, the aim of the study was not to establish an adsorption but to photocatalytically reduce those, which were adsorbed at the same rate from a homogeneous solution to recycle wastewater. Before PCR, the BBR dye and other pollutants had emitted colour on receiving the $h\nu$ where their electronically rich and deficient sites oscillated. The PCR had neutralized them, making them unable to respond to the light, and resulting in colourless solutions. No fragmentations of their structures were aimed except PCR and separation from wastewater, focusing on recycling wastewater. Thus, the physicochemical and PCR studies of B@LGTs are directly connected to excite the VB to CB electrons. The sole moto to study PCPs at different $T/$ K with the same composition was to investigate the kinetic behaviour of 4f electrons. Thus, the PCR experiments designed

with B@LGTs of Nd, Eu, Er, and Yb metals upon increasing their 4f electrons were correlated with the PCPs. The density of energy states of Gd and GO both had caused to receive the maximum $h\nu$ as the Fermi energy gap between their VB and CB was less. This had favoured to excite the VB electrons to the CB without collisions and recombination. The adsorbed pollutants were analysed by FT-IR spectroscopy, and their sites did not respond to IR except resembling to B@LGTs[114] (Fig. 23f). The λ_{max} value of effluents did not change in the darkness, while on receiving $h\nu$ they have generated hole pairs avoiding their recombination (Fig. 22). The UV-vis band spectra were reduced at specific λ_{max} due to single electronic response of unfragmented effluents (Fig. 23 and 27). The FT-IR spectra of BBR has a vibrant fingerprint region on robust bending but after PCR, its quaternary nitrogen ($=N^+-$) was reduced, which neither responded to IR nor the H_2O dipoles. The electron was shifted towards N^+- with stronger electron finding probability enhancing its interaction with H_2O dipoles. On PCR, BBR has reduced the vibrancy of bending and adsorbed without structural fragmentation (Fig. 23f). The conductivities of 0.01%g aq-B@Nd$_2$S$_3$:GO, B@Eu$_2$S$_3$:GO, B@Er$_2$S$_3$:GO, and B@Yb$_2$S$_3$:GO as 30.24, 25.50, 27.23, and 24.50 μs cm^{-1} are produced with 2.23, 2.28, 2.38, and 1.88 eV E_g, respectively (Fig. 8 and 32c). For aq-B@Nd$_2$S$_3$:GO, the lower the E_g, the higher the conductivity. The B@Yb$_2$S$_3$:GO have generated $E_g = 1.88$ eV with 24.50 μs cm^{-1} conductivity credited to 4f^{13} electrons of Yb^{3+}. The one unpaired electron out of the 4f^{13} electrons has reached to CB without causing much collisions. The B@Yb$_2$S$_3$:GO being large in size has low conductivity (Fig. 32c). This research work established a relation among the conductivities and E_g and the number of 4f electrons of LSNRs coated with photosensitive materials such as GO (Fig. 24). The PCR performance was correlated with conductivity, bandgap energy, and BBR quantum yield, as the electronic configuration of the respective B@LGTs has exhibited variable electronic spins due to nuclear charge applied on increasing the 4f electrons in the same period of periodic table. The variable spins of Nd^{3+}, Eu^{3+}, Er^{3+}, and Yb^{3+} of Nd$_2$S$_3$, Eu$_2$S$_3$, Er$_2$S$_3$, and Yb$_2$S$_3$ respectively align the 4f^{7e} of Gd^{3+} on equipartitioning the overall energies, which are subsequently consolidated with FGs and FE of GO. Thus, in the 1st step, a dopant reduced the Fermi energy gap that was further integrated with GO to respond to the external electronic potential with certain mobility noted as conductivities. The least permittivity between the VB and CB has enhanced the mobility of respective ions in the conductometer. A similar mechanism seems to follow during PCR in transforming the hole pairs supported with PCPs and thermodynamic parameters (Fig. 17). The exponential redox cycles without dissociating Ln^{3+} and S^{2-} from LSNRs, nor Gd^{3+} dopant, leached out except narrowing down the Fermi energy gap. These mechanisms have safeguarded optically active GO and equally adhered with B@LSNRs upon generating a high frequency of FRET confining energy to a shorter E_g rather than dissipating. Thus, the magnitudes of PCPs such as conductivity, viscosity, and surface tension promote the PCR of effluents. Therefore, the conductivity and other PCPs of B@LGTs have analysed a mobility of holes for PCR as well as their interacting activities with dipolar water as a protective mechanism. Moreover, a decrease in their conductivities upon increasing the PCR time indicated the adsorption of

reduced BBR, TMIs, and QHIn species (Fig. 32c). The respective charge centres of these species had stronger interactions with water dipoles with higher mobility,[115] but the reduced species could not interact with water and got adsorbed with B@LGTs. Thus, their charge centres, which were individually interacting with water with higher mobility, were now occupied mutually, and the water was phased out with stronger cohesive forces with lower mobility or conductivity. The sizes as Yb$_2$S$_3$ > Er$_2$S$_3$ > Eu$_2$S$_3$ > Nd$_2$S$_3$ with the 4.67, 4.75, 4.71, and 4.86 eV E_g values than the Gd^{3+}@Yb$_2$S$_3$ > Gd^{3+}@Er$_2$S$_3$ > Gd^{3+}@Eu$_2$S$_3$ > Gd^{3+}@Nd$_2$S$_3$ B@LSNR have generated the two E_g values 4.64–1.90, 4.62–2.41, 4.59–2.43, and 4.50–2.50 eV respectively (Fig. 8). The E_g values of LSNR are
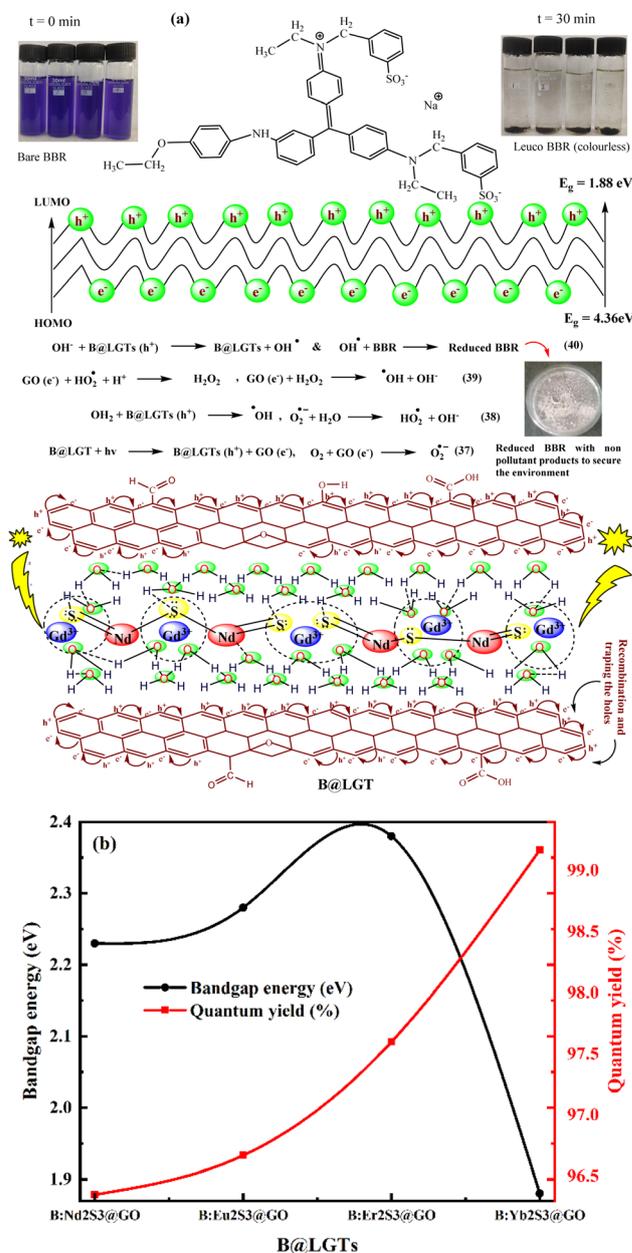

Fig. 22 (a) Aligned lattice interstities for hole generation without recombination. (b) Relationship between the bandgap energy and the quantum yield (%) of BBR dye.
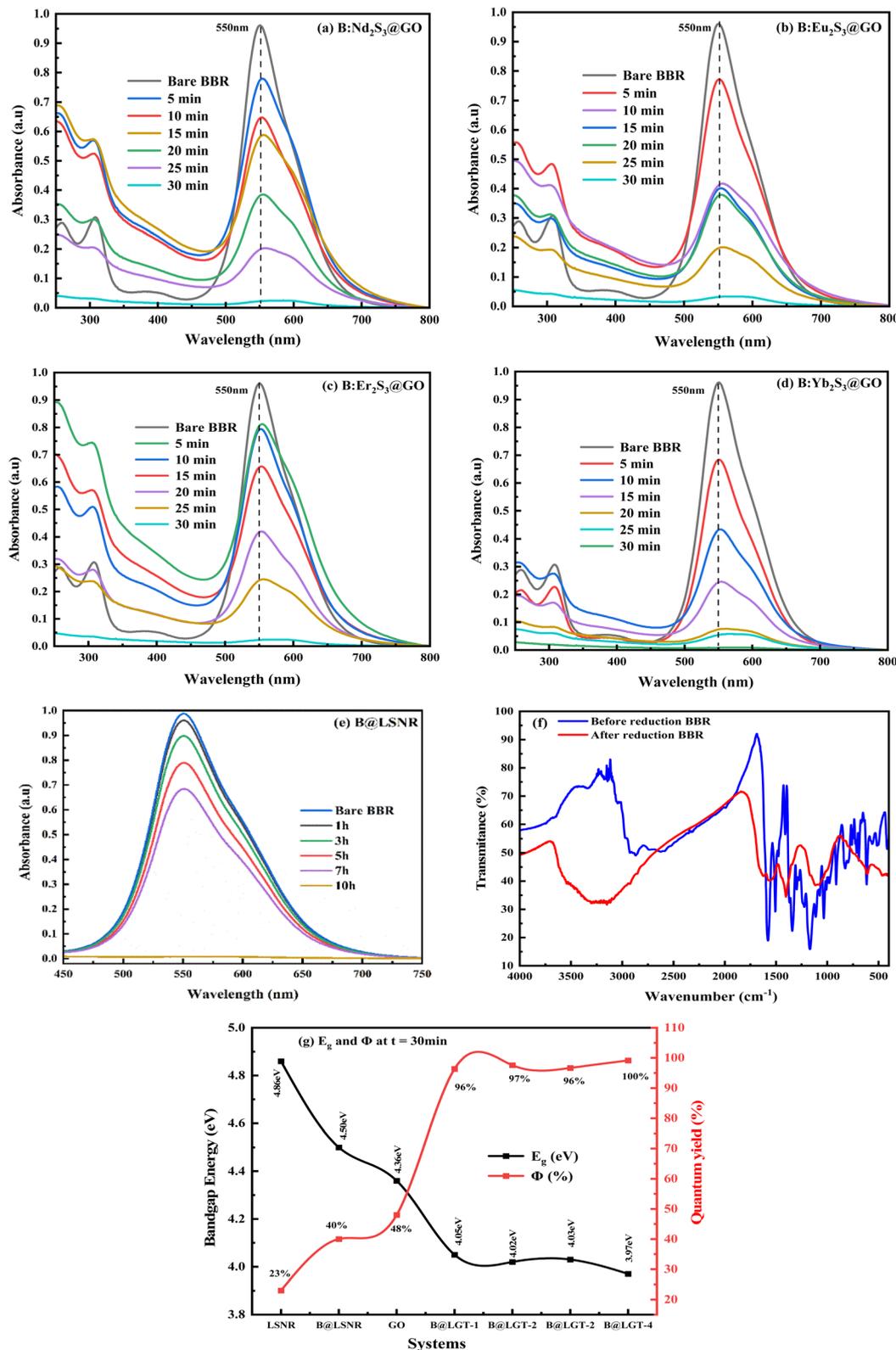
Paper

Fig. 23 (a−d) PCR of BBR with B@LGTs and (e) B@LSNRs. (f) FT-IR spectra before and after PCR. (g) Relation between E_g and Φ.

increased with the increase in 4f electrons from 13, 11, 7, and 3 for Yb^{3+}, Er^{3+}, Eu^{3+}, and Nd^{3+} as their collisions on occupying 4f orbitals are minimized. Gd^{3+} has partitioned E_g from VB_{LSNR} to CB_{LSNR} and $VB_{Gd^{3+}@LSNR}$ to $CB_{Gd^{3+}@LSNR}$ for Gd^{3+} and Ln^{3+} respectively, where S^{2-} has a similar electronic state except orienting effects. The B @Nd_2S_3:GO, B@Eu_2S_3:GO, B@Er_2S_3:GO, and
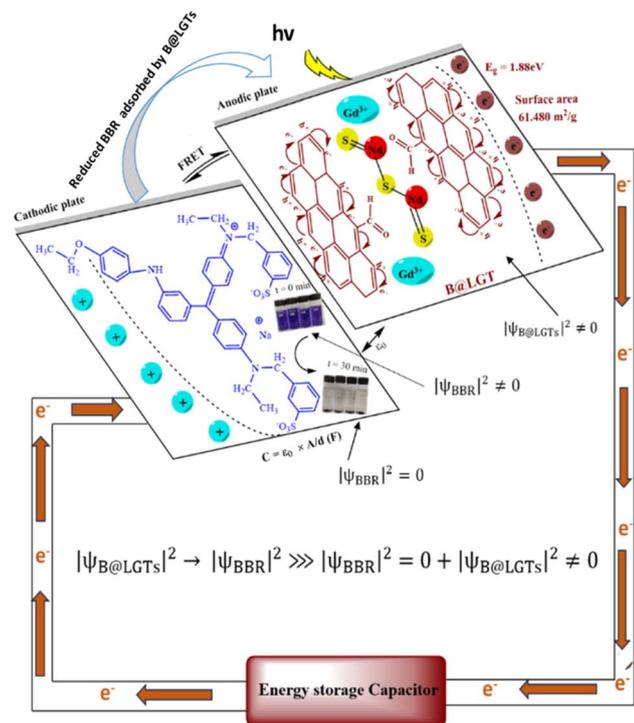
Fig. 24 Negative holes of B@LGT (anodic) approaches towards the quaternary nitrogen of BBR (cathodic) under sunlight and resemble the energy storage of supercapacitors.

B@Yb$_2$S$_3$:GO have two E_g, such as 3.97–1.88, 4.03–2.38, 4.02–2.28, and 4.05–2.23 eV, respectively, for completing PCR in 15–40 min. Gd^{3+} has shared the PE of LSNR enhancing a KE on reducing the E_g values. Thereby, with more KE, the Gd^{3+} has reduced the size of B@LSNR to B@LGT from 100 to 20 nm. From B@LSNR to B@LGTs, the ~62 to 78 mN m^{-1} within the 100 to 20 nm size respectively have PCR the BBR, TMIs, and QHIn in shorter time. The decrease in the size of B@LGTs with the increase in γ values directly predicts the alignment of Ln$^{3+}\cdots$H$_2$O and Gd$^{3+}\cdots$H$_2$O, though S^{2-} bonded with the Ln^{3+} through the covalent bond seems to work similarly. Both Ln$^{3+}\cdots$H$_2$O and Gd$^{3+}\cdots$H$_2$O have addition effects on aligning H$_2$O mutually interconnecting together, similar to the HB away from the bare H$_2$O. The B@LGTs have catalysed an alignment of water dipoles on increasing the dipolar forces at an air–liquid interface. The B@LGTs w.r.t. water dipoles with stabilized charges might have generated the synchronized holes that had shortened a PCR time along monodisperse the effluents. The B@LGTs having 1.88–2.38 eV E_g with lower permittivity on intimate continuity[116] indicate the stabilized dielectric dipoles for PCR activity fitted using Schrödinger eqn (4.6) as follows:

$$E_\psi = \frac{p^2}{2m}\psi + V(x,\,t), \ \ V(x,\,t) = \frac{q^+q^-}{4\pi\varepsilon r^2}, \ \ E_\psi = \frac{p^2}{2m} \gg V(x,\,t)\psi$$
(4.6)

where p is the momentum, m is the mass, $V(x,\,t)$ is PE at x position and t time, and r, nm is the distance between B@LGTs and effluents. At $t = 0$ ($V(x,\,t)\psi = 100\%$, $\frac{p^2}{2m}\psi = 0$ while changing t

from 5 to 30 min, the $\frac{p^2}{2m}\psi$ is >90% and $V(x,\,t)\psi$ is <10%, as predicted *via* PCPs database with B@LGTs (Fig. 22). H$_2$O dipoles adhered with the B@LGTs were replaced by reduced BBR, TMIs, and QHIn and have restricted the stretching and bending causing hedgy oscillations despite a lower surface tension than the aq-B@LSNR (Fig. 17 and 19). The uniform intense oscillating patterns produced with TGA after PCR than a sharper before PCR due to equidistribution of BBR with interstitities of B@LGTs (Fig. 31). Their interfacing with effluents is accountable for stronger physisorption with localized FRET exchanging their mutual energies. The PCPs have revealed their unique response on lowering γ and relaxation time on specific adherence and coherence. The Gd^{3+} dopant and GO due to the spins of 4f electrons and stretching of FGs respectively have accommodated the water dipoles (Fig. 22). Thus, an unreduced effluent did not enter the interstities of BL@LGTs except H$_2$O dipoles to lower the γ. The DTA analysis of B@LGT before and after PCR predicted a uniform energy distribution (Fig. 31). The BBR has been uniformly aligned with synchronized interstities of B@LGT depicted with PCPs like surface properties (Fig. 18–20). The B@LGTs could form the oxygen-based superoxide radicals (O$_2^{\bullet-}$) on splitting the wastewater effluents.[115] O$_2^{\bullet-}$ on protonation seems to produce hydroperoxyl radicals (HO$_2^{\bullet-}$) and free hydroxyl radicals (OH$^\bullet$).[43] The BBR after PCR adsorbed by B@LGT with higher density and negligible VWFs with water get settled at bottom (Fig. 22 and 23). The aq-B@LGTs with slightly higher coherence on aligned H$_2$O dipoles have enhanced the mobility of holes and photocatalytically reduced BBR, Cr^{3+}, Ni^{2+}, and Cu^{2+}, and QHIn in 30, 20, 40, 35, and 15 min respectively. The B@LGTs have absorbed the $h\nu$ at 228 and 312 nm similar to LGTs *via* FRET.[33] Their spins at 302 nm resonated with the BBR dye at 550 nm λ to overcome QEB[117] (Fig. 7a and b). The PCR activities with B@LGTs of Nd (4f^4), Eu (4f^7), Er (4f^{12}), Yb (4f^{14}) have shortened the PCR time by 50% compared to the TMI-GO of Ni (3d^8), Zn (3d^{10}), Cd (4d^{10}) Cr (3d^5), Mn (3d^5), and Fe (3d^6).[61,118] The B@LGT with E_g (1.88–2.30 eV) harnessed solar energy two times than TMI-GO (2.12–4.47 eV) and 4 times than GO[33,61] as 4f$^{@e}$ have generated holes expeditiously than 3d electrons. The B@LGTs have reduced BBR, TMIs, and QHIn in 15–40 min as B:Yb$_2$S$_3$@GO > B:Er$_2$S$_3$@GO > B:Eu$_2$S$_3$@GO > B:Nd$_2$S$_3$@GO with 1.88 < 2.38 < 2.28 < 2.23 eV E_g respectively. Their resonating constituents have higher KE with longer λ with least permittivity.

The amount of dye photocatalyzed with time t noted as C_t was calculated from initial amount (C_0) expressed as (C_0-C_t). The plot (C_t/C_0) *vs.* time gave 2nd order, while the ln(C_0/C_t) *vs.* time, indicated 1st order kinetics to PCR with a residual coefficient R^2 = ~95–99 with 96.35–99.17% Φ (Fig. S5† and Table 7). 40 ppm of BBR was mixed with 0.01 g% of B@LGT for PCR and decreasing UV/vis absorption with time has indicated the PCR of the dye. The absorption *vs.* time plot was used for calculating E_a when electronic transitions occurred, while the viscosity *vs.* T/K plot was used for determining when the B@LGTs underwent rovitronic motions. Thus, the electronic and molecular motions have connected the E_g and E_a values mutually plotted with time (eqn (S1)†). The 96.35, 96.67, 97.60, and 99.17% with B@Nd$_2$S$_3$:GO, B@Eu$_2$S$_3$:GO, B@Er$_2$S$_3$:GO, and B@Yb$_2$S$_3$:GO in

Table 7 Kinetics at pH 7, 0.01 g% B@LGTs, 40 ppm BBR with 1st order

B@LGT	E_g (eV)	E_a (J mol^{-1})	PCR (%)	K (min^{-1})	R^2
B@Nd$_2$S$_3$:GO	2.23	−670.14	96.35	0.0325	0.9975
B@Eu$_2$S$_3$:GO	2.28	−767.39	96.67	0.0318	0.9561
B@Er$_2$S$_3$:GO	2.38	−829.18	97.60	0.0321	0.9818
B@Yb$_2$S$_3$:GO	1.88	−925.57	99.17	0.0315	0.9736

Table 9 Viscosity (mPa S) of B@LGTs at different temperatures

Temp. (K)	B:Nd$_2$S$_3$@GO	B:Eu$_2$S$_3$@GO	B:Er$_2$S$_3$@GO	B:Yb$_2$S$_3$@GO
283.15	0.8506	0.8625	0.8596	0.9281
288.15	0.9943	0.9940	1.0828	1.0658
298.15	0.8904	1.1151	0.8472	0.8669
310.15	0.7531	0.8222	0.8805	0.7531
315.15	0.5990	0.6148	0.5586	0.6301

30 min while the 42.11, 42.22, 42.33, 43.51% Φ with B@Nd$_2$S$_3$, B@Eu$_2$S$_3$, B@Er$_2$S$_3$, and B@Yb$_2$S$_3$ respectively have predicted the significance of doping and coating both (Table 7, S7–S10 and 32b†). The decrease in E_g has increased Φ (%), and Gd^{3+} has equipartitioned the PE to KE as per Schrödinger eqn (4.6). Gd^{3+} with half-filled stability oscillating with longer λ with QTE avoided the electronic collisions and recombination. The holes got strengthened to reach CB channelized to effluents. The lower E_g value with expeditious excitation of 4f electrons has photocatalytically reduced in a shorter time producing maximum Φ (%) without recombining the holes (Fig. 22b and Table 7). The BBR was reduced with B@LGTs from 5 to 30 min at 550 nm with almost similar slope values in the 1st order. The 1st order has predicted that BBR had received the holes at the same rate with each B@LGT being also adsorbed in the first order without any reaction (Fig. S5a†). Thus, the B@LGTs have been reused 10 times to photocatalytically reduce the 10 fresh samples each of 40 ppm BBR than B@LSNR. The constant slope with B@LGTs inferred that the doping and coating have uniformly engaged the LSNR matrices with almost similar charges. The novelty of B@LGTs was to photocatalytically reduce a dye under visible light at 660 nm λ. The fingerprint region of FT IR for BBR before and after PCR remains almost the same except the variation in transmittance. The overall trends of stretching and bending remain the same as no functional sites are occupied permanently during chemisorption with BBR, but the physisorption works well (Fig. 23f). The physisorption of reduced BBR by B@LGTs attained as the water dipoles adhered with unreduced BBR were phased out. Thus, the PCR of charged sites phased out the water dipoles from the dye as the reduced dye phased out water dipoles from B@LGTs, which is noted as a greentech to recycle water (Fig. 22). These changes accompanied infinitesimally small changes in thermodynamic parameters, which predicted phasing of water dipoles from dye to water phase while to dye from water, in case of B@LGTs.

5.1. pH effect on photocatalysis

The wastewater discharged from textile,[50] ink, coating, pulp and paper, and other industries contains various dyes, ions, and even acidic and alkaline contents.[49] The ionic pollutants remain intimately suspended with the water dipoles with stronger dipolar interactions,[119] and hence, a chemical method fails to recycle the water. Initially, the B@LGTs have photocatalytically reduced them to phase out water for adsorbing the reduced pollutants. In this process, the H$^+$ and OH$^-$ ions engage the holes affecting the PCR rate. The B@LGTs also split wastewater to H$^+$ and OH$^-$ ions to balance the charge density needed to photocatalytically reduce the pollutants.[120] The 0.01 g% B@LGTs photocatalytically reduced 40 ppm BBR and 20 ppm TMIs and QHIn at pH 2–12. pH values of 2 and 7 are favourable for the reduction of BBR and 20 ppm TMIs by 35.5 and 99.8% Φ respectively in 15–40 min (Fig. 25a). The pH 2 has formed the H$_3$O$^+$ by engaging the water dipoles that had affected the $h\nu$ capaturing of B@LGTs. The B@LGTs at pH < 7 have generated the positive charges on surfaces either by adsorbing H$^+$ or H$_2$O + H$^+$ = H$_3$O$^+$ with electrostatic repulsion between the B@LGTs and BBR with a lower PCR activity (Fig. 25a). At pH > 7, the surfaces of B@LGTs with OH$^-$ have attracted the h$^+$ holes[121] on lowering Φ by 35–50% and B@LGTs could have aggregated (Fig. 16). The B@LGTs from 2 to 12 pH have absorbed the UV/vis up to 35% while at pH 7, a 99.8% on counterbalancing the H$^+$ and HO$^-$ mutually without engaging the holes (Fig. 25a). While the e$^-$ hole seems to interact with 2H$^+$ + e$^-$ = H$_2$ in acidic media, the h$^+$ hole interacts with 4HO$^-$ + h$^+$ = 2H$_2$O + O$_2$ in alkaline media.

5.2. Monodispersibility for photocatalysis

The 0.01 g% B@LGTs have PCR the 10 to 80 ppm BBR and 20 ppm of each TMIs and QHIn. The @PCR for 80 ppm is lower than that for 40 ppm and 20 ppm BBR and TMIs respectively due to aggregation[122] (Fig. 25c). The 0.008 to 0.012 g% B@LGTs (@0.01 g%) did PCR the BBR and TMIs in 30–45 min. The 0.01 g% B@LGTs have PCR the 99.8% while for >0.01 g%, the

Table 8 Viscosities (mPa S) of aq-LSNR and aq-B@LSNR solutions at different temperatures

Temp. (K)	Nd$_2$S$_3$	Eu$_2$S$_3$	Er$_2$S$_3$	Yb$_2$S$_3$	Nd$_2$S$_3$@Gd	Eu$_2$S$_3$@Gd	Er$_2$S$_3$@Gd	Yb$_2$S$_3$@Gd
283.15	1.0152	1.0000	0.8726	1.0000	0.9050	0.8539	0.8705	0.8514
288.15	1.0555	0.9701	0.9702	1.0590	1.0763	0.9325	1.2536	1.0213
298.15	1.1939	1.0126	0.9930	1.0442	0.8628	0.8590	1.1860	1.1860
310.15	0.7240	0.8223	0.8114	0.8732	0.8950	0.7386	0.6585	0.9569
315.15	0.6379	0.5990	0.5833	0.5650	0.7679	0.5930	0.5833	0.5650

Table 10 Surface tension values (mN m^{-1}) of aq-LSNRs and aq-B@LSNRs at different temperatures

Temp. (K)	Nd$_2$S$_3$	Eu$_2$S$_3$	Er$_2$S$_3$	Yb$_2$S$_3$	Nd$_2$S$_3$@Gd	Eu$_2$S$_3$@Gd	Er$_2$S$_3$@Gd	Yb$_2$S$_3$@Gd
283.15	65.97	63.82	66.01	65.56	73.58	70.91	70.90	68.367
288.15	76.64	76.01	76.64	76.02	77.30	77.28	76.64	76.64
298.15	72.79	72.79	72.79	72.79	72.20	72.21	72.21	72.21
310.15	71.63	72.18	72.19	72.19	72.75	72.18	72.19	72.18
315.15	51.98	66.52	60.56	62.15	70.47	72.09	67.92	65.58

@PCR was slightly lowered. The higher B@LGT concentration got aggregated (Fig. 25b). The >0.01 g% B@LGTs have weakened the H$_2$O–B@LGT interstitial linkages on strengthening the B@LGT–B@LGT interactions. A monolayer NHS aligned around B@LGT favoured PCR (Fig. 16). The water dipoles adhere along the Gd^{3+} and Ln^{3+} sites *in situ* with two separate alignments with stronger cohesive forces by weakening surface continuity predicted with PCPs and thermodynamic parameters (Fig. 18–20).

5.3. PCR of CrCl$_3$, NiCl$_2$, and CuCl$_2$ under visible light on subsequent adsorption

At pH = 7, 0.01 g% aq-B@LGTs photocatalytically reduced and subsequently adsorbed 20 ppm of CrCl$_3$, NiCl$_2$, and CuCl$_2$ individually in 20, 40, and 35 min respectively. The e$^-$ holes produced by the B@LGTs have reduced the 3d^3 (Cr^{3+}), 3d^8 (Ni^{2+}), and 3d^9 (Cu^{2+}) ions to 3d^4 (Cr^0), 3d^8 (Ni^0), and 3d^9 (Cu^0) state. The longer PCR time with NiCl$_2$ having 3d^8 electrons than 3d^9 of Cu^{2+} and 3d^3 of Cr^{3+} predicted the unpaired electrons enhancing the PCR rate. The coloured aq-solutions of Cr^{3+}, Ni^{2+}, and Cu^{2+} turned colourless in 10 min, while in the next 10 min, the spongy nanoclusters appeared (Fig. 27). Initially, B@LGTs with specific surface energies reduced Cr^{3+}, Ni^{2+}, and Cu^{2+} on subsequent adsorption by weakening the ionic interactions with water to zero.[123] The water dipoles aligned with the respective cation tended towards Gd^{3+} and Ln^{3+} integrating the charge spontaneities.[124] The ions with respective charges receive the e$^-$ and h$^+$ holes. The B@LGTs with LSNR–Gd^{3+}–GO have

Table 13 Friccohesity values (cm S^{-1}) of aq-B@LGTs at different temperatures

Temp. (K)	B:Nd$_2$S$_3$@GO	B:Eu$_2$S$_3$@GO	B:Er$_2$S$_3$@GO	B:Yb$_2$S$_3$@GO
283.15	0.0120	0.0119	0.0121	0.0149
288.15	0.0130	0.0130	0.0142	0.0139
298.15	0.0122	0.0153	0.0116	0.0119
310.15	0.0099	0.0117	0.0126	0.0108
315.15	0.0088	0.0090	0.0084	0.0047

trapped the hv for PCR and physisorbed the Cr, Ni, and Cu metals and got settled (Fig. 26). The B@LGTs have oxidized Cl$^-$ to Cl$_2$ in a two-step PCR[122] process (eqn (4.7)–(4.9)). The PCR of TMIs differ from BBR as B@LGTs initially seem to align them with a brownish colour[125] from their respective colours in 1–2 min (Fig. 26B). The B@LGTs competitively disrupted the ionic NHS for physisorption. The ions may get associated with water dipoles adhered[126] to B@LGTs to receive the holes and get reduced (eqn (4.7)–(4.9)). The water dipoles did not interact with Cr, Ni, and Cu metals and so are adsorbed by B@LGs forming a spongy state (Fig. 26). The overall system right from receiving hv and generate the e$^-$ and h$^+$ holes for PCR on subsequent adsorption is dynamic within a liquid phase.[127] Thus, their PCPs have predicted the valuable input about avoiding the air bubbles that hurdle the mobility and continuity. Therefore, the moderate shear and surface tension both have predicted a continuity (Fig. 18 and 19).

$$\text{Aq-B@LGTs} + 2\text{CrCl}_3 \xrightarrow{hv} \text{B@LGTs*}(h^+ + e^-) + 2\text{Cr}^{3+} + 4\text{Cl}^-$$

$$2\text{Aq-Cr}^{3+}(4e^-) + 4\text{Cl}^-(4h^+) \rightarrow 2\text{Cr}^0 + 2\text{Cl}_2 \qquad (4.7)$$

$$\text{Aq-B@LGTs} + 2\text{NiCl}_2 \xrightarrow{hv} \text{B@LGTs*}(h^+ + e^-) + 2\text{Ni}^{2+} + 4\text{Cl}^-$$

$$2\text{Aq-Ni}^{2+}(4e^-) + 4\text{Cl}^-(4h^+) \rightarrow 2\text{Ni}^0 + 2\text{Cl}_2 \qquad (4.8)$$

$$\text{Aq-B@LGTs} + 2\text{CuCl}_2 \xrightarrow{hv} \text{B@LGTs*}(h^+ + e^-) + 2\text{Cu}^{2+} + 4\text{Cl}^-$$

$$2\text{Aq-Cu}^{2+}(4e^-) + 4\text{Cl}^-(4h^+) \rightarrow 2\text{Cu}^0 + 2\text{Cl}_2 \qquad (4.9)$$

Table 11 Surface tension values (mN m^{-1}) of aq-B@LGTs at different temperatures

Temp. (K)	B:Nd$_2$S$_3$@GO	B:Eu$_2$S$_3$@GO	B:Er$_2$S$_3$@GO	B:Yb$_2$S$_3$@GO
283.15	70.90	72.53	70.90	68.38
288.15	76.66	76.64	76.01	76.64
298.15	72.78	72.79	72.79	72.79
310.15	76.36	72.18	72.18	72.18
315.15	67.95	68.00	66.01	70.51

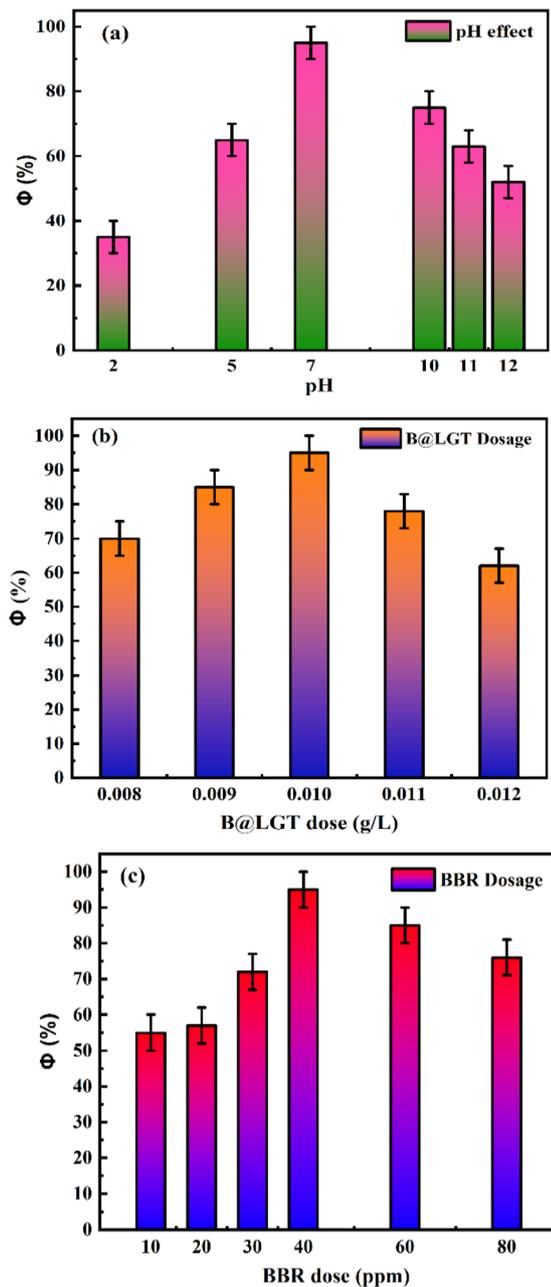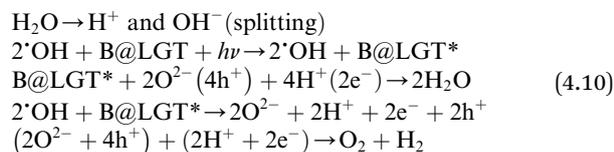**Table 12** Friccohesity values (cm S^{-1}) of aq-LSNRs and aq-B@LSNRs at different temperatures

Temp. (K)	Nd$_2$S$_3$	Eu$_2$S$_3$	Er$_2$S$_3$	Yb$_2$S$_3$	Nd$_2$S$_3$@Gd	Eu$_2$S$_3$@Gd	Er$_2$S$_3$@Gd	Yb$_2$S$_3$@Gd
283.15	0.0154	0.0141	0.0132	0.0130	0.0123	0.0120	0.0123	0.0129
288.15	0.0138	0.0128	0.0127	0.0139	0.0139	0.0121	0.0164	0.0133
298.15	0.0164	0.0139	0.0136	0.0143	0.0111	0.0096	0.0164	0.0164
310.15	0.0101	0.0117	0.0112	0.0125	0.0123	0.0102	0.0091	0.0133
315.15	0.0122	0.0090	0.0096	0.0091	0.0109	0.0082	0.0086	0.0086

Fig. 25 Effect of (a) pH, (b) B@LGT photocatalyst dosage and (c) BBR dosage.

5.4. PCR of QHIn to HIn

First, 2 mg HIn and 1 mg NaOH dissolved in 100 mL water formed pink-coloured QHIn at pH > 9. Keeping 2 mL of 0.01 g% aq-B@LGTs with 30 mL aq-QHIn under visible light showed discolouration in 15 min upon reducing QHIn to HIn (Fig. 27d). The B@LGTs have split H_2O into H^+ and OH^- as follows:

$$H_2O \rightarrow H^+ \text{ and } OH^- \text{ (splitting)}$$
$$2^\bullet OH + B@LGT + h\nu \rightarrow 2^\bullet OH + B@LGT^*$$
$$B@LGT^* + 2O^{2-}(4h^+) + 4H^+(2e^-) \rightarrow 2H_2O \quad (4.10)$$
$$2^\bullet OH + B@LGT^* \rightarrow 2O^{2-} + 2H^+ + 2e^- + 2h^+$$
$$(2O^{2-} + 4h^+) + (2H^+ + 2e^-) \rightarrow O_2 + H_2$$

Excess e^- holes reoriented the quinonoid benzene ring of QHIn, while Na^+ oxidised an anion of HIn as a sodium benzoate salt of HIn as intermediate.[128] The B@LGT solution has faded a QHIn pink stint at $t = 15$ min on sharing the electronic charges due to charged sites. The B@LGT with spontaneities has intimately adhered QHIn to initiate a reduction. The colour could not disappear with LSNR and B@LSNR while the B@LGTs have aligned OH^-, Na^+, and quinonoid ring to interact with holes in infinite populations. The B@LGTs with respective charges/holes have turned the native pink stint of QHIn on reducing OH^- to O_2 and H_2 (eqn (4.10) and (Fig. 28b)). OH^- and Na^+ could have generated stronger affinities for water dipoles.[129] The partial positive charge could have interacted with OH^-, Na^+, and quinonoid ring for PCR in certain area (Fig. 28). The quinonoid benzene ring could have reacted with Na^+ while OH^- entered B@LGT interstities gaining higher density to get settled at bottom with time. Initially, the salts and QHIn were monodispersed with B@LGT on moderate electrostatic interactions with robust oscillating activities.

5.5. PCR of methyl orange (MO) dye

The 0.01 g% aq-B@LGTs with 20 ppm MO turned into a dark red colour solution after 2 h. The residual charges of 4-(dimethylamino)phenyl, diazenyl, and sodium benzenesulfonate could not resonate the energies. The wavefunction ψ_{-CH_3} of ERG $-CH_3$ could not interface $\psi_{-phenyl}$ and $\psi_{dizenyl}$ of 4-(dimethylamino)phenyl and diazenyl that have disintegrated benzenesulfonate (Fig. 29a). Thus, their mismatched ψ counterbalance mutually on occupying their own functional sites deflecting the holes unlike the BBR, TMIs, and QHIn (Fig. 29d). The B@LGTs could not photocatalytically reduce a conjugated aligned dye due to a stronger azo ($-N=N-$) group. The e^- and h^+ holes have responded SO_3^- and partially got settled after 5 h as delocalization of MO could have been tracked by the FGs of GO in coated B@LGT (Fig. 29f). The $(-N(CH_3)_3)$ and $(-N=N-)$ constituents of MO have mutually mismatched their respective angular momentums with least electron finding probability expressed as orthogonal $\int\int\int_{-\infty}^{\infty} \psi_{eN(CH_3)_3}\psi_{-N|N-} = 0$ that could not receive the holes except minor adsorption (Fig. 29). Its transition dipole moment ($\mu = 0$) within the VB to CB space ($d\tau = dxdydz$) along the x, y, and z dimensions is almost nil as follows:

$$\text{Transition dipole moment} = \int(\psi_{-N(CH_3)_3})\mu \times (\psi_{-N=N-})d\tau \quad (4.11)$$

Thus, the MO needs stronger photocatalysts than B@LGTs to photocatalytically reduce the quinonoid, quaternary nitrogen ($=N^+-$), and TMIs to receive the holes. The B@LGTs have acted as photosensors for the effluents containing quinonoid, $=N^+-$, and TMIs to photocatalytically reduce except azo groups such as MO (Fig. 29).

5.6. Photocatalyst reusability

It was found that 0.01 g% B@LGTs have reduced 40 ppm BBR and 20 ppm TMIs in the 1st cycle. For the 2nd cycle, the used B@LGTs were washed with H_2O to photocatalytically reduce fresh 40 ppm BBR. It continues to reuse the B@LGTs after

washing for reducing the 3rd fresh sample of 40 ppm BBR. Thus, 0.01 g% B@LGTs after washing were reused to photocatalytically reduce 10 fresh BBR samples in 30, 35, 40, 45, 50, 60, 75, 90, 105, and 120 min respectively with 68–98.9% Φ (Fig. 32a). The B@LGTs have physisorbed BBR, TMIs, and QHIn within the interstitial tiers with weaker VWFs. The B@LGT with adsorbed dye seem to have the two energy ensembles within

tiers with milder VWFs up to 10 reuse cycles. After 5 subsequent PCR cycles, the B@LGTs were analysed with the FT-IR spectra, TEM images and TGA curves (Fig. 30 and 31). Their hedgy thermograms predicted physisorption that resulted in an acoustic structure on exchanging energies mutually. Reduced BBR, TMIs, and QHIn with stronger interaction have differed in bending and stretching frequencies. Thus, the reduced
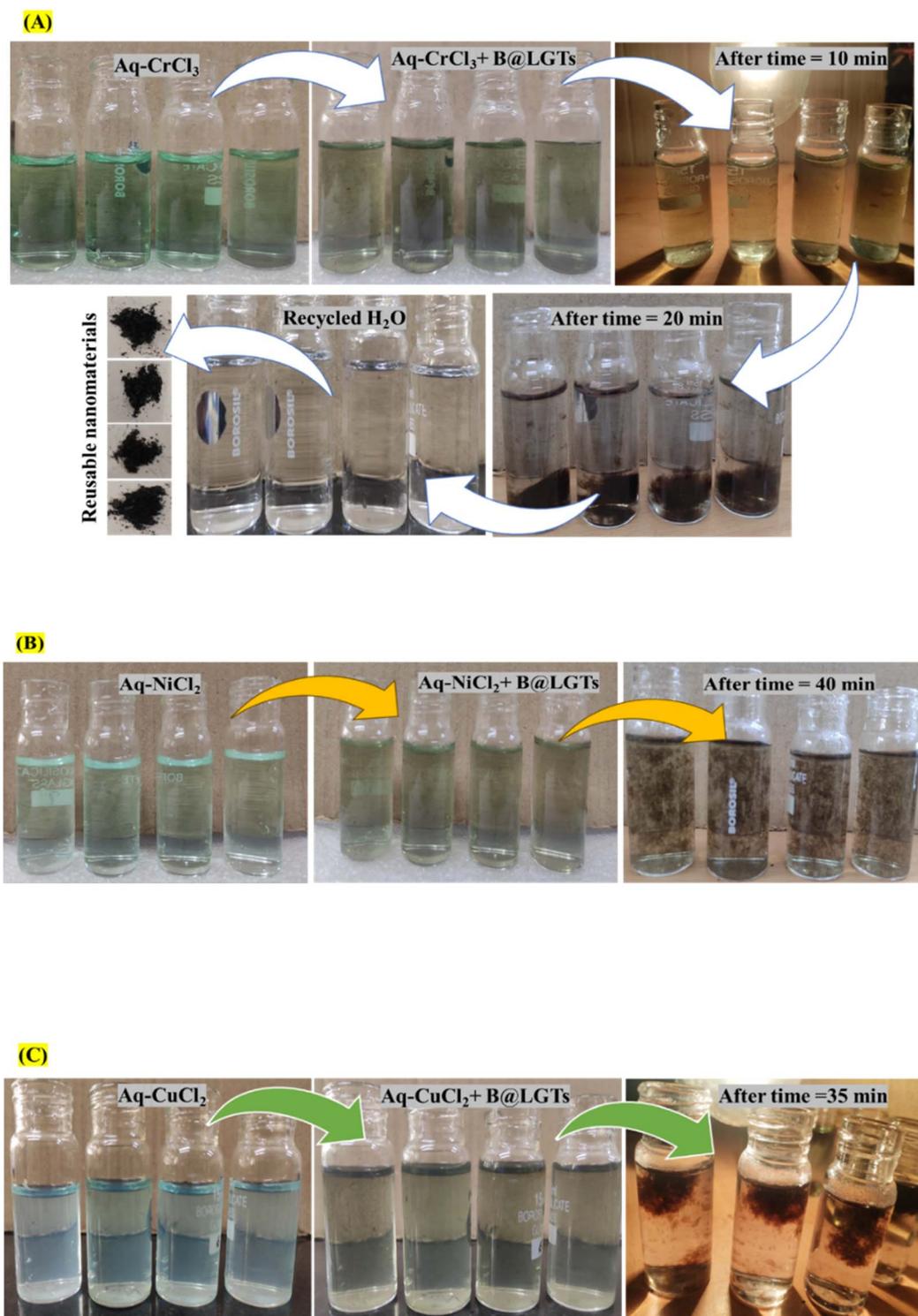
Fig. 26 PCR of 20 ppm $CrCl_3$ (A), $NiCl_2$ (B), and $CuCl_2$ (C) on subsequent adsorption using 0.01 g% of B@LGTs under visible light.
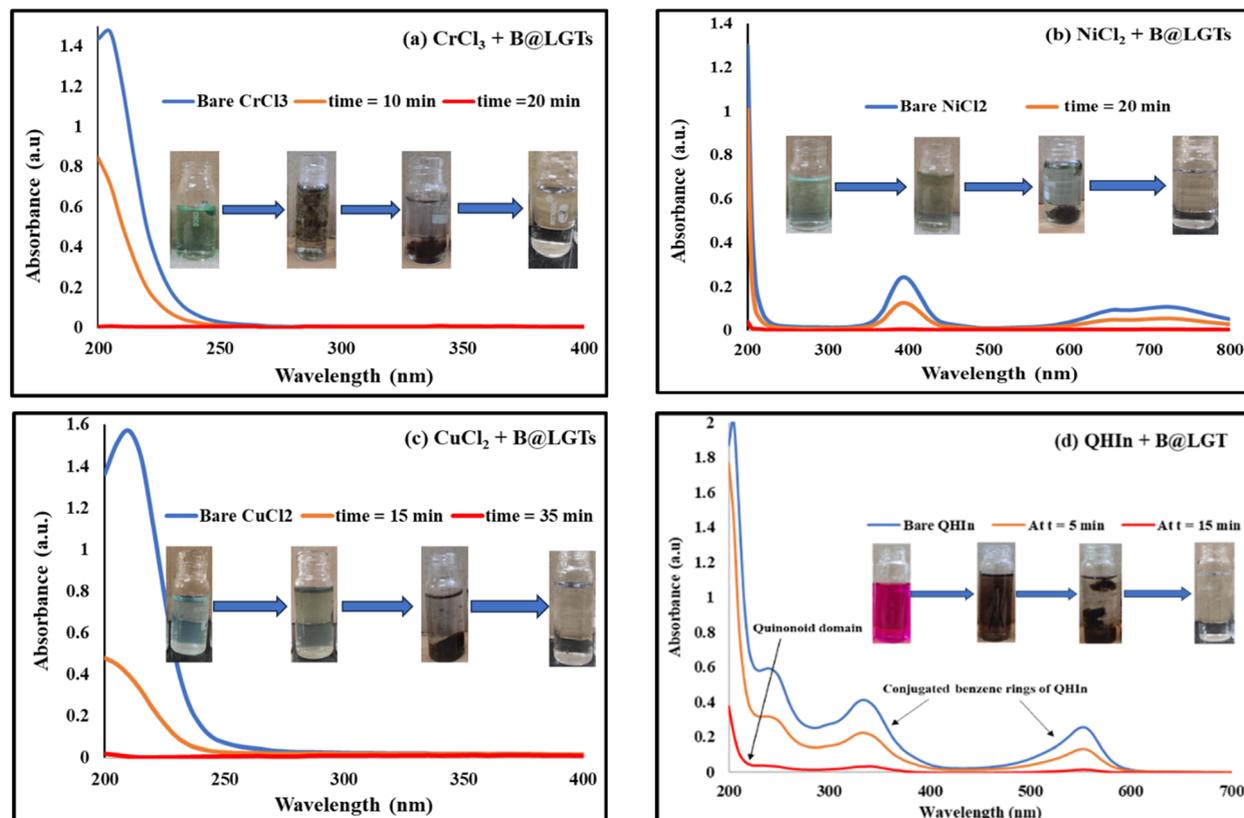
Fig. 27 (a–c) UV-vis spectra for the PCR of $CrCl_3$, $NiCl_2$, and $CuCl_2$ and (d) QHIn using 0.01 g% B@LGTs.
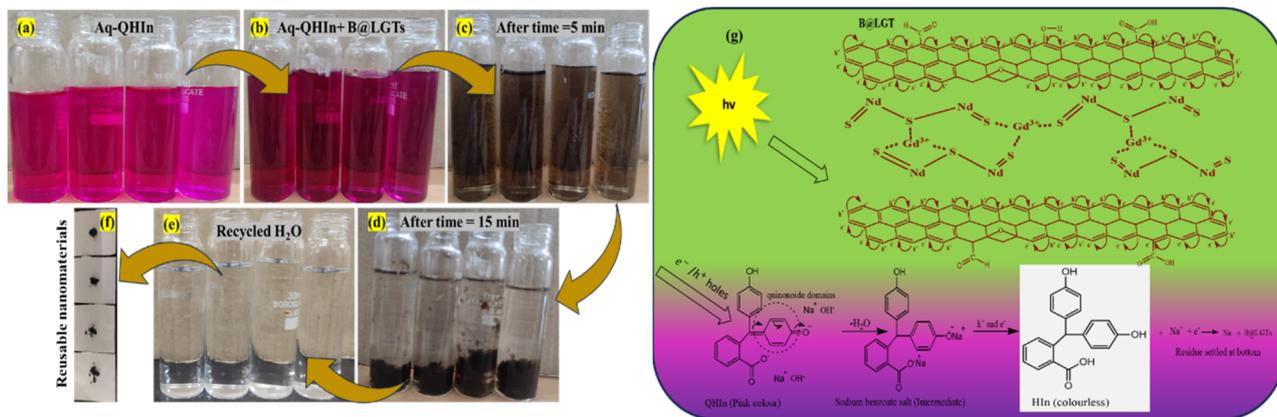

Fig. 28 (a–f) Disappearance of the colour followed by the reduced QHIn settling at the bottom. (f) Recycled clean water. (g) Proposed mechanism under visible light.

effluents with their residual charges due to different electronic configurations of their constituents have interacted with the B@LGTs apart from the PCR of quaternary nitrogen. Thermally stable B@LGT could advance the science in areas of nano thin films, piezoelectric devices, and photoluminescent sensors.[98] The B@LGTs on reuse for 10 cycles seem to have been reinforced with enhanced durability and networking[55] similar to smart resin with GO and metallic nanoparticles.[130] The FT-IR spectra, TGA curves, and HR-TEM images predicted dye-reinforced B@LGT (DRB) rather than bare ones by detaining the

same frameworks (Fig. 30 and 31). The HR-TEM images predicted a slightly flattened morphology compared to the bare ones due to residual forces[98] generated on exposing to hv. The dopant and coating agents have developed a quasistatic structure of B@LGTs with symmetric interstities oscillating in the same phase. That had excellently worked as the reversible state on receiving the photons and developing the holes without undergoing structural transitions. Thus, the B@LGTs could act as photoluminescent to sharpen the nano thin films on window glass, vehicle glass, and solar panels.[39,131]
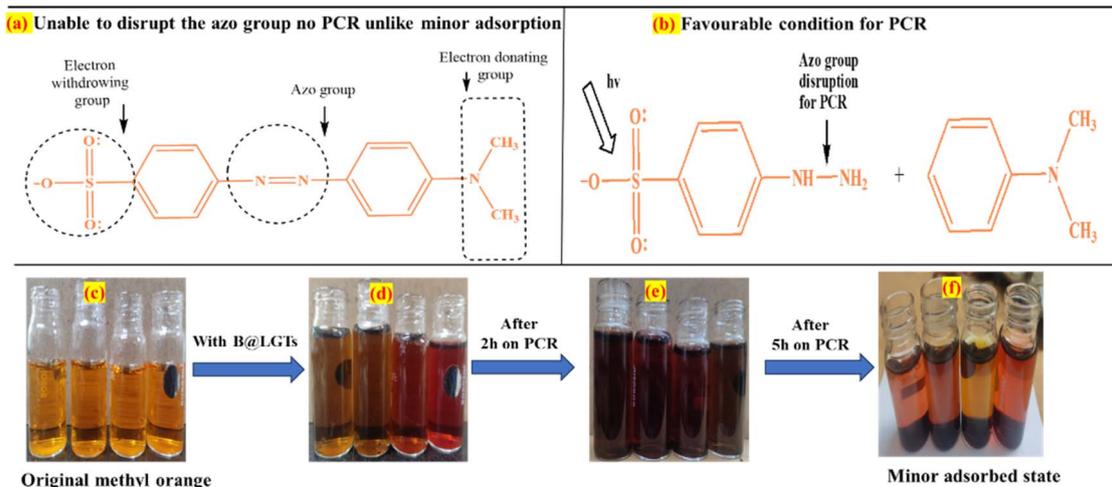
Fig. 29 (a and b) Plausible mechanism for MO dye to favour PCR (c) original MO (d) dye with B@LGTs (e) solution after 2 hours and (f) solution after 5 hours, indicated the B@LGTs did not PCR but partially adsorbed the MO dye under visible light owing to the presence of highly stable azo group with a high potential energy.
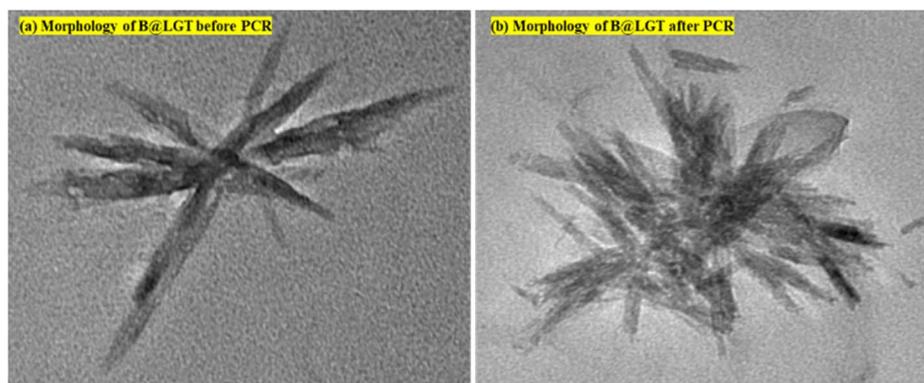

Fig. 30 (a and b) HR-TEM images of B@LGT elucidating the stable morphology before and after the PCR of the pollutants.
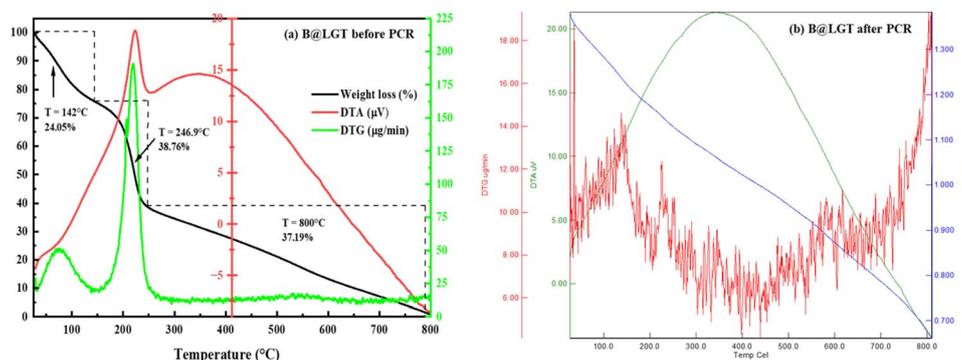

Fig. 31 (a and b) Varying TGA, DTG and DTA patterns differentiating the spinning of increasing 4f electrons for B@LGT before and after the PCR of pollutants.

5.7. MO + B@LGTs treated in acidic and basic media separately

The B@LGTs had photocatalytically reduced BBR, TMIs, and QHIn as their native colours got disappeared while MO in an acidic solution (with HCl) showed colour fading negligibly with

negligible PCR. The holes from B@LGTs have oxidized Cl$^-$ to Cl$_2$ and split water, while the holes could not interact with (–N(CH$_3$)$_3$) and (–N==N–) eqn (4.12). The holes from B@LGTs 300–400 nm could not access highly stable groups of MO and no colour faded (Fig. 32d). The B@LGTs to photocatalytically
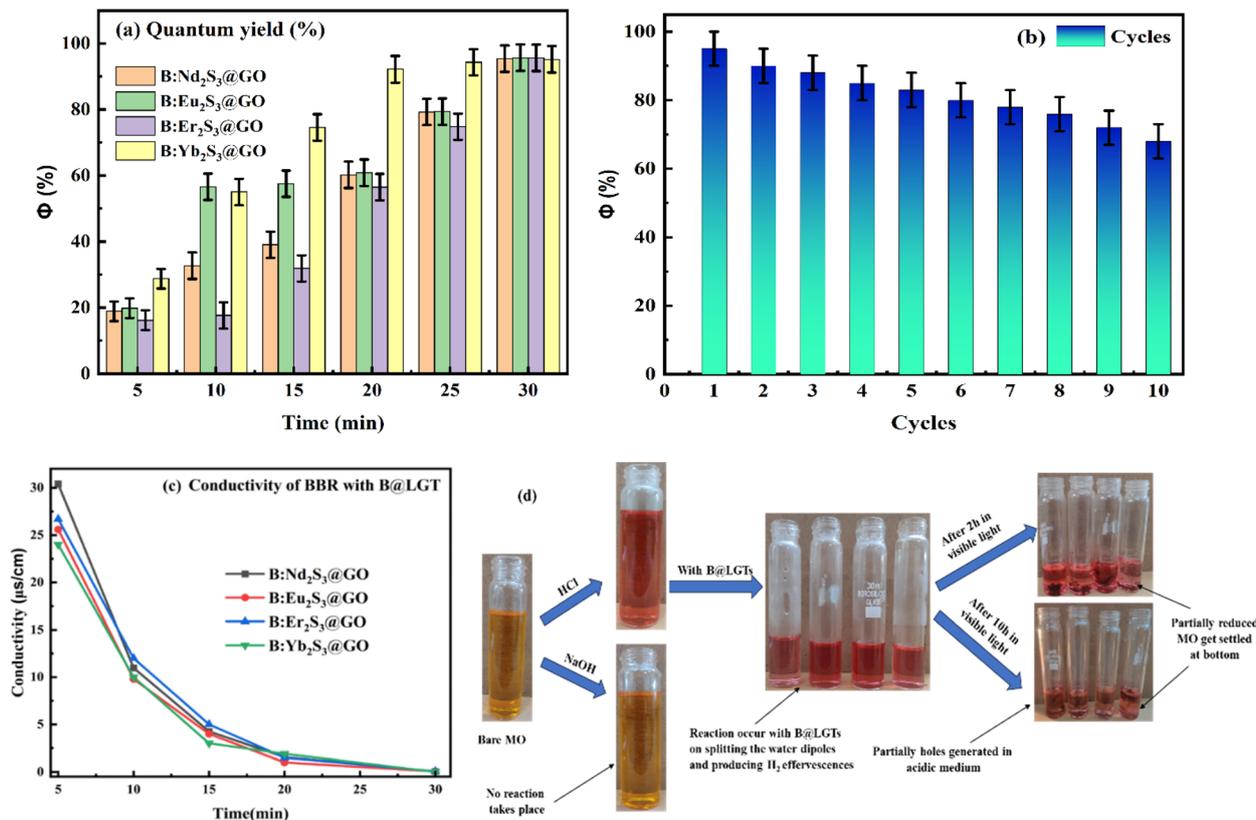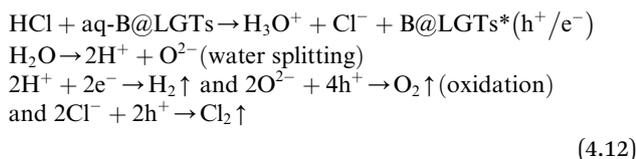
Fig. 32 Spectra elucidating (a) Φ of BBR, (b) 10 times reusability of B@LGTs, (c) conductivity during the PCR and (d) B@LGTs negligibly undergoing PCR rather than partially adsorbing the MO dye in an acidic medium due to higher potential energy.

reduce MO are functionalized further with highly π conjugated molecules such as flavonoids. The B@LGTs in an acidic medium form H_3O^+ and have split water to O_2 and H_2 with robust effervescences, generating holes under visible light that acted as an indicator to control the pH (Fig. 32d). The B@LGTs have oxidized Cl^- into Cl_2 with $2h^+$ holes to scavenge Cl^- that could equally scavenge in biomedical, biophysical, dyeing, and water treatment.

$$HCl + aq\text{-}B@LGTs \rightarrow H_3O^+ + Cl^- + B@LGTs^*(h^+/e^-)$$
$$H_2O \rightarrow 2H^+ + O^{2-} (\text{water splitting})$$
$$2H^+ + 2e^- \rightarrow H_2\uparrow \text{ and } 2O^{2-} + 4h^+ \rightarrow O_2\uparrow (\text{oxidation})$$
$$\text{and } 2Cl^- + 2h^+ \rightarrow Cl_2\uparrow$$

$$(4.12)$$

The B@LGTs have scavenged OH^- in alkaline solutions and H^+ in acidic solutions, respectively, as pH scavenger and anti-dots for controlling the acidity and alkalinity of the solutions.[23]

6. Conclusion

Lanthanide sulphide nanorods of Nd, Eu, Er, and Yb have been synthesized by reducing 0.001 M $LnCl_3 \cdot 6H_2O$ with 0.006 M Na metal at NTP for generating ~73.71 mL H_2 gas by CRM. On passing the H_2S gas to aq-$Ln(OH)_3$, LSNRs have been produced. LSNRs were doped and coated with Gd^{3+} and GO for B@LSNRs and B@LGTs respectively. Then 0.01 g% of B@Nd_2S_3:GO,

B@Eu_2S_3:GO, B@Er_2S_3:GO, and B@Yb_2S_3:GO have separately photocatalytically reduced 40 ppm of BBR and 20 ppm of $CrCl_3$, $NiCl_2$, and $CuCl_2$, and QHIn individually with 96.35–99.17% quantum yield in 30, 20, 40, 35, and 15 min respectively under visible light. B@Yb_2S_3:GO and B@Er_2S_3:GO have proven to be robust photocatalysts by performing PCR in 30 min with thermodynamic stability predicted with PCPs. The PCPs such as density, viscosity, sound velocity, surface tension, and friccohesity have predicted their thermodynamically stable mono-dispersions at 288.15, 298.15, and 310.15 K. Their PCPs have elucidated the functional surfaces to receive the $h\nu$ and to interface with BBR, TMIs, and QHIn without aggregation. The GO and Gd^{3+} tiers have enhanced PCR with 10 times reusability. The intimate interfacing of BBR dye, TMIs, and QHIn with B@LGTs *via* quantum tunnelling effects for photosensitization was examined with PCPs and thermodynamic parameters. The higher friccohesity of 0.01 g% B@LGTs have confirmed eige-nenergies to align water dipoles with a higher surface area on strengthening adhesive forces. B@Nd_2S_3:GO, B@Eu_2S_3:GO, B@Er_2S_3:GO, B@Yb_2S_3:GO, with 2.23, 2.28, 2.38, and 1.88 eV E_g respectively and with higher surface energies could be used as the heat sensor, functional group detector, chemical sensor, and energy storage. The B@LGTs could substitute the piezo-electric sensors, acoustics, and routine adsorbents due to aligned interstities. The reusable trifunctional B@LGT photo-catalysts could remediate other wastewater effluents than BBR, metal salts, and QHIn.

Abbreviation

GO	Graphene oxide
LSNRs	Lanthanide sulfide nanorods
B@LSNRs	Bimetallic lanthanide sulfide nanorods
NRs	Nanorods
B@LGT	Bimetallic lanthanide GO template
$4f^{@e}$	Number of 4f electrons
BBR	Brilliant blue red
TMIs	Transition metal ions
QHIn	Quinonoid phenolphthalein
PCPs	Physicochemical properties
FRET	Friccohesity resonance energy transfer
CRM	Crash reaction methodology
FT-IR	Fourier transform infrared
Rovitronic motions	Rotational, vibrational, and translational motions
Gt	Graphite
GtO	Graphite oxide
IFTs	Interfacial templates
UPE	Unpaired electron
MFP	Mean free path
RBF	Round-bottom flask
RPM	Revolution per minute
aq	Aqueous
PDN	Pendant drop number
VFT	Viscous flow time
Cohad	Cohesive and adhesive forces
CCP	Consistency cohad point
TC	Tentropic cavity
wt	Weight
FE	Functional edges
RE	Resonating energy
SL	Sunlight
PCR	Photocatalytic reduction
TGA	Thermogravimetric analysis
DTG	Differential thermal gravimetry
ΔH	Enthalpy
ΔE_a	Activation energy
ΔS_t	Tentropy
ψ_{sv}	Single-valued wavefunction

Data availability

The data supporting this article have been included as part of the ESI file.†

Author contributions

Krishan Kumar conducted the bench work, calculations, some discussions, and figure plotting, and wrote up the experimental observations and conclusions. Prof. Man Singh supervised the research work and participated in discussions, explored new models to explain experimental observations and derived new scientific insights out of the research.

Conflicts of interest

The authors confirm that there is no conflict of interest.

Acknowledgements

References

1 M. E. Borges, M. Sierra, E. Cuevas, R. D. García and P. Esparza, *Sol. Energy*, 2016, **135**, 527–535.

2 X. Chen, P. Zhang, D. H. Kuo, Q. Wu, A. B. Abdeta, B. Wu, Z. Su, L. Chen, O. A. Zelekew and J. Lin, *J. Mater. Chem. A*, 2023, **11**, 19091–19106.

3 Z. Wu, X. Yuan, G. Zeng, L. Jiang, H. Zhong, Y. Xie, H. Wang, X. Chen and H. Wang, *Appl. Catal. B Environ.*, 2018, **225**, 8–21.

4 T. A. Aragaw, F. M. Bogale and B. A. Aragaw, *J. Saudi Chem. Soc.*, 2021, **25**(8), 101280.

5 P. Zhang, H. Wang, Y. Lai, Y. Xu, L. Chen, Q. Wu, D.-H. Kuo, D. Lu, M. T. Mosisa, J. Li, J. Lin and X. Chen, *J. Water Process Eng.*, 2024, **58**, 104820.

6 T. A. Saleh, *Environ. Technol. Innov.*, 2021, **24**, 101821.

7 R. Koutavarapu, M. R. Tamtam, M. C. Rao, S. G. Peera and J. Shim, *Chemosphere*, 2021, **272**, 129849.

8 H. Wu, L. Li, K. Chang, K. Du, C. Shen, S. Zhou, G. Sheng, W. Linghu, T. Hayat and X. Guo, *J. Environ. Chem. Eng.*, 2020, **8**(4), 103882.

9 Y. Li, M. Fu, R. Wang, S. Wu and X. Tan, *Chem. Eng. J.*, 2022, **444**, 136567.

10 M. Sun, J. Ma, M. Zhang, Y. Xiao, Y. Zhu and S. Zhang, *Mater. Chem. Phys.*, 2020, **241**, 122450.

11 P. Zhang, Y. Lai, X. Dai, Y. Xu, X. Wu, B. Yang, D.-H. Kuo, D. Lu, Q. Wu, M. T. Mosisa, J. Lin and X. Chen, *J. Environ. Chem. Eng.*, 2024, **12**, 111831.

12 D. Saini, R. Aggarwal, S. R. Anand and S. K. Sonkar, *Sol. Energy*, 2019, **193**, 65–73.

13 P. Zhang, Q. Wu, H. Wang, Y. Xu, Y. Lai, P. Li, D.-H. Kuo, T. Huang, H. Zhang, M. T. Mosisa, J. Li, J. Lin, X. Chen and D. Lu, *Mater. Today Chem.*, 2024, **37**, 102028.

14 X. Chen, H. Sun, O. A. Zelekew, J. Zhang, Y. Guo, A. Zeng, D.-H. Kuo and J. Lin, *Appl. Surf. Sci.*, 2020, **525**, 146531.

15 M. T. Mosisa, P. Zhang, B. Wu, L. Chen, Z. Su, P. Li, H. Zhang, A. Farooq, T. Huang, A. B. Abdeta, O. A. Zelekew, D.-H. Kuo, J. Lin, X. Chen and D. Lu, *J. Environ. Chem. Eng.*, 2024, **12**, 113383.

16 V. V. Klepov, K. A. Pace, L. S. Breton, V. Kocevski, T. M. Besmann and H. C. Zur Loye, *Inorg. Chem.*, 2020, **59**, 1905–1916.

17 Z. Liu, X. Sun, S. Xu, J. Lian, X. Li, Z. Xiu, Q. Li, D. Huo and J. G. Li, *J. Phys. Chem. C*, 2008, **112**, 2353–2358.

18 X. Luo, M. Zhang, L. Ma and Y. Peng, *J. Rare Earths*, 2011, **29**, 313–316.

19 A. V Ruseikina, O. V Andreev, E. O. Galenko and S. I. Koltsov, *J. Therm. Anal. Calorim.*, 2017, **128**, 993–999.

20 I. Valsamakis and M. Flytzani-Stephanopoulos, *Appl. Catal. B Environ.*, 2011, **106**, 255–263.

21 R. Mauricot, P. Gressier, M. Evain and R. Brec, *J. Alloys Compd.*, 1995, **223**, 130–138.

22 S. A. Osseni, S. Lechevallier, M. Verelst, P. Perriat, J. Dexpert-Ghys, D. Neumeyer, R. Garcia, F. Mayer, K. Djanashvili, J. A. Peters, E. Magdeleine, H. Gros-Dagnac, P. Celsis and R. Mauricot, *Nanoscale*, 2014, **6**, 555–564.

23 S. R. Sanivarapu, J. B. Lawrence and G. Sreedhar, *ACS Omega*, 2018, **3**, 6267–6278.

24 N. Vashistha, A. Chandra and M. Singh, *New J. Chem.*, 2020, **44**, 14211–14227.

25 C. M. Marin, L. Wang, J. R. Brewer, W. N. Mei and C. L. Cheung, *J. Alloys Compd.*, 2013, **563**, 293–299.

26 I. L. Ikhioya and A. C. Nkele, *Arabian J. Sci. Eng.*, 2023, **49**, 1217–1225.

27 S. Roméro, A. Mosset, J. C. Trombe and P. Macaudière, *J. Mater. Chem.*, 1997, **7**, 1541–1547.

28 H. Tang, L. N. Sacco, S. Vollebregt, H. Ye, X. Fan and G. Zhang, *J. Mater. Chem. A*, 2020, **8**, 24943–24976.

29 A. Roca-Sabio, M. Regueiro-Figueroa, D. Esteban-Gómez, A. de Blas, T. Rodríguez-Blas and C. Platas-Iglesias, *Comput. Theor. Chem.*, 2012, **999**, 93–104.

30 S. Dev and M. Singh, *Solid State Sci.*, 2022, **134**, 107045.

31 N. Shukla, D. K. Verma, A. K. Singh, B. Kumar, Kavita and R. B. Rastogi, *ACS Appl. Nano Mater.*, 2020, **3**, 8012–8026.

32 M. L. Redígolo, D. S. Koktysh, K. van Benthem, S. J. Rosenthal and J. H. Dickerson, *Mater. Chem. Phys.*, 2009, **115**, 526–529.

33 K. Kumar, B. Sahoo, T. C. Meghwal and M. Singh, *Energy Adv.*, 2023, **3**, 198–225.

34 P. Glaser, O. Stewart, R. Atif, D. R. C. Asuigui, J. Swanson, A. J. Biacchi, A. R. Hight Walker, G. Morrison, H. C. zur Loye and S. L. Stoll, *Angew. Chem., Int. Ed.*, 2021, **60**, 23134–23141.

35 A. Kumar, S. Kumar, A. Bahuguna, A. Kumar, V. Sharma and V. Krishnan, *Mater. Chem. Front.*, 2017, **1**, 2391–2404.

36 M. T. Mosisa, P. Zhang, Z. Su, B. Wu, L. Chen, Y. Liao, A. Farooq, D. Lu, A. B. Abdeta, D.-H. Kuo, J. Lin and X. Chen, *J. Environ. Chem. Eng.*, 2024, **12**, 112111.

37 X. Chen, D.-H. Kuo and D. Lu, *Chem. Eng. J.*, 2016, **295**, 192–200.

38 X. Chen, D.-H. Kuo, D. Lu, Y. Hou and Y.-R. Kuo, *Microporous Mesoporous Mater.*, 2016, **223**, 145–151.

39 J. M. Coronado, F. Fresno, M. D. Hernández-Alonso and R. Portela, *Design of Advanced Photocatalytic Materials for Energy and Environmental Applications*, 2013, vol. 71.

40 L. Hu, Y. Li, X. Peng, W. Zheng, W. Xu, J. Zhu, L. Y. S. Lee, P. K. Chu and K. Y. Wong, *Chem. Eng. J.*, 2021, **417**, 127900.

41 T. P. Gompa, A. Ramanathan, N. T. Rice and H. S. La Pierre, *Dalton Trans.*, 2020, **49**, 15945–15987.

42 H. Wu, J. Peng, H. Sun, Q. Ruan, H. Dong, Y. Jin, Z. Sun and Y. Hu, *Chem. Eng. J.*, 2022, **432**, 134339.

43 P. Borthakur and M. R. Das, *J. Colloid Interface Sci.*, 2018, **516**, 342–354.

44 X. Chen, H. Sun, J. Zhang, Y. Guo and D.-H. Kuo, *J. Mol. Liq.*, 2019, **273**, 50–57.

45 F. Uddin, *Cellulose*, 2021, **28**, 10715–10739.

46 P. Bai, U. J. Etim, Z. Yan, S. Mintova, Z. Zhang, Z. Zhong and X. Gao, *Catal. Rev.*, 2018, **61**(3), 333–405.

47 L. Alcaraz, O. R. Largo, F. J. Alguacil, M. Á. Montes, C. Baudín and F. A. López, *Metals*, 2021, 13.

48 C. Wang, M. Chen, J. Wu, F. Mo and Y. Fu, *Anal. Chim. Acta*, 2019, **1086**, 66–74.

49 B. N. Joshi, H. Yoon, S. H. Na, J. Y. Choi and S. S. Yoon, *Ceram. Int.*, 2014, **40**, 3647–3654.

50 M. Ubaidullah, A. M. Al-Enizi, T. Ahamad, S. F. Shaikh, M. A. Al-Abdrabalnabi, M. S. Samdani, D. Kumar, M. A. Alam and M. Khan, *J. Energy Storage*, 2021, **33**, 102125.

51 S. Fahrendorf, N. Atodiresei, C. Besson, V. Caciuc, F. Matthes, S. Blügel, P. Kögerler, D. E. Bürgler and C. M. Schneider, *Nat. Commun.*, 2013, **4**, 1–6.

52 X. Zeng, Y. Liu, T. Zhang, J. C. Jin, J. L. Li, Q. Sun, Y. J. Ai, M. L. Feng and X. Y. Huang, *Chem. Eng. J.*, 2021, **420**, 127613.

53 O. P. Kumar, M. N. Ashiq, M. Ahmad, S. Anjum and A. ur Rehman, *J. Mater. Sci. Mater. Electron.*, 2020, **31**, 21082–21096.

54 I. Valsamakis, R. Si and M. Flytzani-Stephanopoulos, *J. Power Sources*, 2010, **195**, 2815–2822.

55 J. Chang, S. Zang, W. Liang, D. Wu, Z. Lian, F. Xu, K. Jiang and Z. Gao, *J. Colloid Interface Sci.*, 2021, **590**, 114–124.

56 A. Khaligh and Z. Li, *IEEE Trans. Veh. Technol.*, 2010, **59**, 2806–2814.

57 A. G. Stern, *Int. J. Hydrogen Energy*, 2018, **43**, 4244–4255.

58 V. J. Reddy, N. P. Hariram, R. Maity, M. F. Ghazali and S. Kumarasamy, *World Electr. Veh. J.*, 2023, **14**(12), 349.

59 X. Chen, H. Sun, D.-H. Kuo, A. B. Abdeta, O. A. Zelekew, Y. Guo, J. Zhang, Z. Yuan and J. Lin, *Appl. Catal. B Environ.*, 2021, **287**, 119992.

60 R. Kumari and M. Singh, *ACS Omega*, 2020, **5**, 23201–23218.

61 K. Kumar, R. P. Dave, S. Dev and M. Singh, *RSC Adv.*, 2022, **12**, 29734–29756.

62 G. Avashthi and M. Singh, *New J. Chem.*, 2021, **45**, 5463–5483.

63 R. Jain, M. Mathur, S. Sikarwar and A. Mittal, *J. Environ. Manage.*, 2007, **85**, 956–964.

64 Q. Liang, J. Jin, M. Zhang, C. Liu, S. Xu, C. Yao and Z. Li, *Appl. Catal. B Environ.*, 2017, **218**, 545–554.

65 A. B. Abdeta, Q. Wu, D.-H. Kuo, P. Li, H. Zhang, T. Huang, J. Zhang, J. Lin and X. Chen, *J. Catal.*, 2022, **413**, 1056–1069.

66 X. Chen, T. Huang, D.-H. Kuo, H. Sun, P. Li, O. A. Zelekew, A. B. Abdeta, Q. Wu, J. Zhang, Z. Yuan and J. Lin, *Appl. Catal. B Environ.*, 2021, **298**, 120542.

67 J. P. Guggenbichler, M. Böswald, S. Lugauer and T. Krall, *Infection*, 1999, **27**, S16–S23.

68 M. Salavati-Niasari, M. R. Loghman-Estarki and F. Davar, *Inorg. Chim. Acta*, 2009, **362**, 3677–3683.

69 T. Charinpanitkul, A. Soottitantawat, N. Tonanon and W. Tanthapanichakoon, *Mater. Chem. Phys.*, 2009, **116**, 125–128.

70 P. Malik, S. S. Maktedar, G. Avashthi, T. K. Mukherjee and M. Singh, *Robust Curcumin-Mustard Oil Emulsions for Pro to Anti-oxidant Modulation of Graphene Oxide*, King Saud University, 2020, vol. 13.

71 W. C. Yang, C. W. Wang, J. C. Wang, Y. C. Chang, H. C. Hsu, T. E. Nee, L. J. Chen and J. H. He, *J. Nanosci. Nanotechnol.*, 2008, **8**, 3363–3368.

72 G. Viola, J. Chang, T. Maltby, F. Steckler, M. Jomaa, J. Sun, J. Edusei, D. Zhang, A. Vilches, S. Gao, X. Liu, S. Saeed, H. Zabalawi, J. Gale and W. Song, *ACS Appl. Mater. Interfaces*, 2020, **12**, 34643–34657.

73 M. S. Longair, *Philos. Trans. R. Soc., A*, 2008, **366**, 1685–1696.

74 S. Saxena, T. A. Tyson, S. Shukla, E. Negusse, H. Chen and J. Bai, *Appl. Phys. Lett.*, 2011, **99**, 67–70.

75 N. Sakai and T. Saito, *Polyhedron*, 2004, **23**, 2611–2614.

76 A. R. Altaf, H. Teng, M. Zheng, I. Ashraf, M. Arsalan, A. U. Rehman, L. Gang, W. Pengjie, R. Yongqiang and L. Xiaoyu, *J. Environ. Chem. Eng.*, 2021, **9**, 105313.

77 Y. P. Varshni, *Physica*, 1967, **34**, 149–154.

78 E. Asikuzun, O. Ozturk, L. Arda, A. T. Tasci, F. Kartal and C. Terzioglu, *Ceram. Int.*, 2016, **42**, 8085–8091.

79 X. Chen, Q. Wu, D. H. Kuo, A. B. Abdeta, H. Zhang, P. Li, T. Huang, O. A. Zelekew and J. Lin, *J. Mater. Chem. A*, 2023, **11**, 4126–4141.

80 S. Faisal, F. A. Jan, S. Saleem, R. Ullah, R. Wajidullah, N. Ullah and N. Salman, *Nanotechnol. Environ. Eng.*, 2022, **7**, 675–689.

81 P. Mountapmbeme, A. El, L. Wu, M. Waqas and Z. Tian, *J. Taiwan Inst. Chem. Eng.*, 2018, 1–9.

82 Q. Wu, A. B. Abdeta, D. H. Kuo, H. Zhang, Q. Lu, J. Zhang, O. A. Zelekew, M. T. Mosisa, J. Lin and X. Chen, *J. Mater. Chem. A*, 2022, **10**, 5328–5349.

83 Z. Quan, Z. Wang, P. Yang, J. Lin and J. Fang, *Inorg. Chem. ACS*, 2007, **46**, 1354–1360.

84 M. Mahar, G. Khuram, S. Ahmad, L. Almanqur, A. Guy and T. Suliman, *J. Appl. Electrochem.*, 2024, **54**, 257–273.

85 M. A. Harrison, S. Somarajan, S. V Mahajan, D. S. Koktysh, K. Van Benthem and J. H. Dickerson, *Mater. Lett.*, 2011, **65**, 420–423.

86 M. M. Gul, K. S. Ahmad, S. A. Alderhami, A. G. Thomas, Y. T. Alharbi and L. Almanqur, *Mater. Sci. Eng. B*, 2023, **297**, 116776.

87 G. Physics, A. Abdullayeva and I. Bakhtiyarly, *Glass Phys. Chem.*, 2020, **60**, 7.

88 S. B. Ubale, S. B. Kale, V. J. Mane, P. P. Bagwade and C. D. Lokhande, *J. Solid State Electrochem.*, 2021, **25**, 1753–1764.

89 S. B. Ubale, S. B. Kale, V. J. Mane, U. M. Patil and C. D. Lokhande, *J. Electroanal. Chem.*, 2021, **897**, 115589.

90 N. Sato, M. Odori, M. Skrobian, M. Saito, T. Fujino and N. Masuko, *Shigen Sozai*, 1994, **110**, 869–874.

91 S. Anjana, *Dalton Trans.*, 2019, **48**, 2926–2938.

92 S. H. Han, K. A. Gschneidner and B. J. Beaudry, *J. Alloys Compd.*, 1992, **181**, 463–468.

93 N. Singh, M. Gordon, H. Metiu and E. Mcfarland, *J. Appl. Electrochem.*, 2016, **46**, 497–503.

94 M. Kumar, P. Rajput, P. K. Singh, A. C. Yadav, S. A. Khan, S. N. Jha, F. Singh and A. C. Pandey, *RSC Adv.*, 2016, **6**, 108523–108529.

95 H. Taz, R. Ruther, A. Malasi, S. Yadavali, C. Carr, J. Nanda and R. Kalyanaraman, *J. Phys. Chem. C*, 2015, **119**, 5033–5039.

96 S. Wang, L. Xu, L. Wang, A. Liang and Z. Jiang, *Luminescence*, 2013, **28**, 842–846.

97 M. Abdullah, M. M. Alanazi, S. A. M. Abdelmohsen, S. D. Alahmari, S. Aman, A. Sadaf, A. G. Al-Sehemi, A. M. A. Henaish, Z. Ahmad and H. M. T. Farid, *Mater. Sci. Eng. B*, 2024, **301**, 117207.

98 C. H. Lai, M. Y. Lu and L. J. Chen, *J. Mater. Chem.*, 2012, **22**, 19–30.

99 M. J. Neves, J. B. De Oliveira, L. P. R. Ospedal and J. A. Helayël-Neto, *Phys. Rev. D*, 2021, **104**, 15006.

100 G. Tai, T. Zeng, J. Yu, J. Zhou, Y. You, X. Wang, H. Wu, X. Sun, T. Hu and W. Guo, *Nanoscale*, 2016, **8**, 2234–2241.

101 G. Vijayaprasath, I. Habibulla, V. Dharuman, S. Balasubramanian and R. Ganesan, *ACS Omega*, 2020, **5**, 17892–17899.

102 A. A. Dakhel and M. El-Hilo, *J. Appl. Phys.*, 2010, **107**, 123905.

103 P. Macaudie, *J. Mater. Chem.*, 1997, **7**, 1541–1547.

104 Z. Yang, H. Peng, W. Wang and T. Liu, *J. Appl. Polym. Sci.*, 2010, **116**, 2658–2667.

105 J. J. Carey and M. Nolan, *Solid State Ionics*, 2017, **307**, 51–64.

106 M. I. Marković and A. D. Rakić, *Opt. Laser Technol.*, 1990, **22**, 394–398.

107 M. Singh, *J. Chem. Thermodyn.*, 2007, **39**, 240–246.

108 H. J. Zhao, L. H. Li, L. M. Wu and L. Chen, *Inorg. Chem.*, 2010, **49**, 5811–5817.

109 J. H. Qiao, V. Mishra, M. C. Fishbein, S. K. Sinha and T. B. Rajavashisth, *Exp. Mol. Pathol.*, 2015, **99**, 654–662.

110 J. Kurawa, M. A. Jaafar and J. Bayero, *Pure Appl. Sci.*, 2021, **14**, 64–70.

111 R. V. Blasques, M. A. A. Pereira, A. M. R. V. Mendes, N. E. M. Filho, W. C. Gomes, L. T. Arenas, J. L. Marty, M. I. P. Gurgo, G. S. Nunes and P. C. M. Villis, *Mater. Chem. Phys.*, 2020, **243**, 122255.

112 R. P. Dave and M. Singh, *Int. J. Biol. Macromol.*, 2023, **231**, 123243.

113 A. Chandra, P. Malik, S. Singh, A. Roy, N. Sahoo and M. Singh, *Chem. Eng. Process.*, 2022, **174**, 108870.

114 M. P. Rayaroth, U. K. Aravind and C. T. Aravindakumar, *Chemosphere*, 2015, **119**, 848–855.

115 Z. Su, X. Wu, D. H. Kuo, B. Yang, B. Wu, L. Chen, P. Zhang, J. Lin, D. Lu and X. Chen, *J. Mater. Chem. A*, 2024, **12**, 10494–10506.

116 T. S. Sreeprasad and V. Berry, *Small*, 2013, **9**, 341–350.

117 P. Roy and S. K. Srivastava, *CrystEngComm*, 2015, **17**, 7801–7815.

118 S. Dev and M. Singh, *J. Phys. Chem. Solids*, 2020, **139**, 109335.

119 P. Zhang, L. Chen, D. H. Kuo, B. Wu, Z. Su, D. Lu, Q. Wu, J. Li, J. Lin and X. Chen, *J. Mater. Chem. A*, 2024, **12**, 7163–7177.

120 H. Karimi, H. R. Rajabi and L. Kavoshi, *J. Photochem. Photobiol., A*, 2020, **397**, 112534.

121 B. Li, T. Liu, Y. Wang and Z. Wang, *J. Colloid Interface Sci.*, 2012, **377**, 114–121.

122 A. Reghioua, D. Barkat, A. H. Jawad, A. S. Abdulhameed, S. Rangabhashiyam, M. R. Khan and Z. A. ALOthman, *J. Polym. Environ.*, 2021, **29**, 3932–3947.

123 A. B. Abdeta, H. Sun, Y. Guo, Q. Wu, J. Zhang, Z. Yuan, J. Lin and X. Chen, *Adv. Powder Technol.*, 2021, **32**, 2856–2872.

124 Z. Su, B. Wu, L. Chen, M. T. Mosisa, P. Zhang, Q. Wu, D.-H. Kuo, D. Lu, O. A. Zelekew, J. Lin and X. Chen, *J. Sci.:Adv. Mater. Devices*, 2023, **8**, 100645.

125 A. Barde, U. V. Agbogo and A. I. Lawal, *Int. J. Multidiscip. Res. Growth Eval.*, 2022, 1–8.

126 Y. Guo, O. A. Zelekew, H. Sun, D.-H. Kuo, J. Lin and X. Chen, *Sep. Purif. Technol.*, 2020, **242**, 116769.

127 Q. Wu, X. Wang, J. Fu, O. A. Zelekew, A. B. Abdeta, D.-H. Kuo, J. Zhang, Z. Yuan, J. Lin and X. Chen, *J. Sci.:Adv. Mater. Devices*, 2021, **6**, 578–586.

128 P. Yin, Y. Chen, Y. Wang, Y. Chi, B. Li, M. Xu, H. Song and C. Chen, *J. Environ. Chem. Eng.*, 2023, **11**, 110374.

129 X. Li, L. Chen, P. Zhang, A. B. Abdeta, Q. Wu, B. Wu, J. Lin, D.-H. Kuo, Y. Zhang and X. Chen, *J. Sci.:Adv. Mater. Devices*, 2023, **8**, 100598.

130 T. Zhang, T. Ma and W. Li, *J. Macromol. Sci., Part B:Phys.*, 2015, **54**, 992–1000.

131 V. G. Rajeshmon, C. S. Kartha, K. P. Vijayakumar, C. Sanjeeviraja, T. Abe and Y. Kashiwaba, *Sol. Energy*, 2011, **85**, 249–255.